

# POLITECNICO DI TORINO

Master Degree in  
Electronic Engineering



Master Degree Thesis

## Development of a laser beam modeling tool for high power applications

### **Supervisors**

Prof. Guido Perrone  
Prof. Renato Orta

### **Candidates**

Alice Franco  
Irene Velotti

Academic Year 2019-2020

*To those who I love so much and I am so lucky to be loved in return - Alice*  
*To those who have always believed in me - Irene*

# Abstract

Amazing technological progresses have been made in the high-power laser field in the last few decades, thus allowing laser systems to be used in several applications, ranging from materials processing (cutting, marking, welding etc.) to biomedical and military sectors.

Before the last decade, laser material processing was dominated by CO<sub>2</sub> lasers. However, due to their very low wall plug efficiency (amount of electrical power converted into optical power) and mechanical reliability issues, CO<sub>2</sub> lasers have been replaced by fiber lasers, which are pumped by high power laser diodes (HPLDs). HPLDs are characterized by compactness, high efficiency, high reliability and low ownership costs. Since 2017, the HPLDs became the leading market sector for lasers. The state of the art of the single emitting chips is around 10 W; in order to obtain kilowatt range sources, different beam combining techniques are employed.

The thesis purpose is the development of a versatile tool to design devices based on the beam stacking of single emitters with applications to high-power laser modules and beam shaping components. The model is based on *Ray Tracing Technique* and Gaussian beams and has been assessed by comparing the results with measurements obtained from ad hoc experimental benches.

The developed software is able to realize a laser module with a variable number of chips and to assemble them in the desired structure (array, rectangle, circle, etc.) by selecting the positions where to locate the diodes. It is also possible to modify the parameters of the chips, as the dimensions and the emission wavelength.

Concerning the beam shaping applications, the effect of different optical elements aimed at material processing was studied. A ring-shaped beam, useful to obtain circular cutting profiles, was simulated by means of the tool; the action of a set of cylindrical lenses producing a laser line incident on the target material was instead verified in laboratory.

# Introduction

Technological progresses in high-power laser diode environment have revolutionised some fields that were not accessible before, such as scientific, military, medical and commercial sectors. Particularly, the material processing has been the most revolutionised field in the last decade due to the introduction of fiber lasers and laser diodes at the industrial grade.

Until a few years ago, laser material processing was dominated by CO<sub>2</sub> lasers, gas laser exhibiting fine cutting for thick metallic workpieces. However, the CO<sub>2</sub> laser reveals a very low wall plug efficiency and mechanical reliability issues; hence, since cutting and welding require high beam quality, these lasers have been easily replaced by fiber lasers, which are marked out by higher gain and higher efficiency. Indeed, since 2013, fiber lasers have been prevailing in the worldwide industrial laser revenues.

Due to the revolution of fiber lasers in the material processing sector, the development of high power laser modules arises because the fiber lasers are usually pumped by high-power laser diodes (HPLDs), characterized by compactness, high efficiency, high reliability and low ownership costs.

From an application point of view, laser diodes are the most widely used lasers thanks to several advantages [1]: great range of power emission (from mW to W), wide range of wavelength selection from ultraviolet to infrared, long lifetime and operation both in continuous mode and pulse mode.

Nevertheless, laser diodes need the passing of high current density through the tiny layer where carriers combine in order to emit light; so, they are sensitive to current spike and also to electric static discharge. Moreover, they can be multi-modes and provide modal competition. Critical shortcomings are also the beam astigmatism and large divergence.

This thesis focuses on the employment of laser diodes in the material processing contest, particularly they can be used for applications like cutting, marking and welding. The simplest laser diode is a single emitter, whose state of art in high-power applications is more than 10 W, but, in order to achieve kilowatt range sources, different beam combining techniques are employed. As a result, the laser diode modules have been introduced.

The main purpose of the thesis project is to realise a MATLAB software tool capable of modeling the laser diode emission evolving through different optical systems, and to simulate the high-power multi-emitter device.

Applications such as material cutting require laser beam shaping in order to replicate on the target the desired outline; the software then provides the possibility of producing laser line or circular profiles, obtained respectively by means of cylindrical or conical lenses (axicon).

The laser emission analysis, described in details in the first chapter, is based on the Gaussian beam theory, which asserts that ideally the laser beam intensity is characterized by a Gaussian profile. Nevertheless, it is also possible to examine beams marked out by non-Gaussian behavior by introducing the  $M^2$  parameter. The  $M^2$  factor describes the deviation of a beam from a ideal Gaussian beam; real-world lasers  $M^2$  factor is always  $> 1$ .

In the second chapter a representation of the beam based on the *Ray Tracing Technique* has been applied. The model introduced, called Gaussian beam ray-equivalent model, relies onto a set of five rays (chief ray, waist rays and divergence rays), specified by a certain origin and slope. Such approach is valid in the limits of the paraxial approximation, so the angles involved must be smaller than  $20^\circ$ . The main disadvantage of rays is that being paths, they cannot be associated to an amplitude and a phase: the Gaussian beam model was exploited to provide a complete perspective of the beam under analysis.

In order to demonstrate the correctness of the developed MATLAB codes, in the third chapter comparisons between the simulation outputs and the physical measurements carried out in laboratory have been fulfilled. Two lasers having different  $M^2$  values have been analysed during the laboratory experiences: a quasi-Gaussian beam laser (He-Ne) and an astigmatic beam laser (green pointer).

Once ascertained the congruence of the tool, the main theme of the thesis was treated in the fourth chapter: high-power laser modules. The developed MATLAB software is able to simulate a fiber-coupled laser module with a variable number of chips and to arrange them in the desired structure (array, rectangle, circle, etc.) by selecting the positions where to locate the diodes. The code provides as outputs the total power intensity on the fiber lens and at the input of the fiber core; furthermore, the power loss in the fiber core and the power in the fiber numerical aperture can be evaluated.

In the last chapter, several setups to shape the beam intensity profile have been realised. By means of beam shaping, various optical elements can be employed to design the laser beam spot size geometry: for example, the axicon implementation resulted into a ring-shaped profile intensity. A cylindrical lenses setup was instead realized in laboratory and was applied to achieve a laser line able to cut materials, e.g. paper or metal. Lastly, optimization tools were exploited to minimize (or maximize) the function under analysis by choosing the input values within a given range.

# Contents

<b>1</b>	<b>Introduction To Lasers</b>	<b>1</b>
1.1	Lasers historical evolution . . . . .	1
1.2	Laser diode operating principle . . . . .	3
1.3	High-power lasers . . . . .	5
1.3.1	Beam combining for laser modules . . . . .	8
1.4	Gaussian beams . . . . .	12
1.4.1	Complex beam parameter . . . . .	14
1.4.2	Non-Gaussian beams: $M^2$ factor . . . . .	15
1.4.3	High-power laser diode emission . . . . .	16
1.5	Higher order modes . . . . .	18
1.5.1	Hermite-Gaussian modes . . . . .	18
1.5.2	Super-Gaussian beams . . . . .	19
<b>2</b>	<b>Ray Tracing Technique</b>	<b>21</b>
2.1	Mathematics of lenses . . . . .	22
2.2	Five rays technique . . . . .	26
2.3	Beam focalisation . . . . .	27
2.3.1	Thin focusing lens . . . . .	28
2.3.2	Thick focusing lens . . . . .	30
2.4	Beam collimation . . . . .	32
2.4.1	Thin collimating lens . . . . .	33
2.4.2	Thick collimating lens . . . . .	34
2.5	Off-axis propagation . . . . .	35
<b>3</b>	<b>Laser Beam Tool Validation</b>	<b>38</b>
3.1	He-Ne Laser . . . . .	39
3.1.1	Source characterization . . . . .	40
3.1.2	Spherical lens setup . . . . .	42
3.1.3	Cylindrical lens setup . . . . .	43
3.2	Green Laser Pointer . . . . .	45
3.2.1	Source characterization . . . . .	46
3.2.2	Spherical lens setup . . . . .	49
3.2.3	Cylindrical lens setup . . . . .	50

---

<b>4</b>	<b>High Power Laser Module</b>	<b>52</b>
4.1	Module setup . . . . .	53
4.2	Module software preparatory insight . . . . .	54
4.3	Source analysis . . . . .	59
4.3.1	$M^2$ and BPP parameters . . . . .	59
4.3.2	Source chips statistical analysis . . . . .	60
4.4	Field propagation inside the module . . . . .	64
4.5	Simulation results . . . . .	68
4.5.1	Single laser diodes stack . . . . .	69
4.5.2	Super-Gaussian laser diodes stack . . . . .	70
4.5.3	Double laser diodes stacks . . . . .	72
4.5.4	Multiple stacks . . . . .	73
4.5.5	New geometries . . . . .	74
4.5.6	Double laser diodes stacks - chips statistical analysis . . . . .	76
<b>5</b>	<b>Beam Shaping Applications</b>	<b>78</b>
5.1	Round wedge prism . . . . .	79
5.2	Axicon . . . . .	81
5.3	Laser line . . . . .	85
5.3.1	Optimization methods . . . . .	86
5.3.2	Experimental setup . . . . .	90
	<b>Bibliography</b>	<b>96</b>

# List of Figures

1.1	First laser: Maiman's ruby laser, 1960. . . . .	2
1.2	Example of direct (GaAs) and indirect (Si) bandgap semiconductor [3].	3
1.3	Photon stimulated emission phenomenon [4]. . . . .	4
1.4	Laser diode optical cavity. . . . .	4
1.5	Laser diode emission [1]. . . . .	5
1.6	High power laser applications [7]. . . . .	6
1.7	High power laser market in the last few years [7]. . . . .	6
1.8	CO <sub>2</sub> laser operation scheme. . . . .	7
1.9	Fiber laser operation scheme. . . . .	7
1.10	Fiber laser emission. . . . .	8
1.11	Laser module package. . . . .	9
1.12	Classification of the beam combining [12]. . . . .	9
1.13	Spatial [15] beam combining techniques. . . . .	11
1.14	Wavelength beam combining techniques. . . . .	11
1.15	Polarization beam combining techniques. . . . .	11
1.16	Gaussian beam intensity and amplitude distribution [18]. . . . .	13
1.17	Gaussian beam intensity [19]. . . . .	14
1.18	Gaussian beam profile along the SA (left) and FA (right). . . . .	16
1.19	Gaussian beam cross section when changing the distance between the source point ( $z = 0$ mm) and the observation point with a step of 6 mm up to $z = 30$ mm. . . . .	17
1.20	Intensity profile of the Hermite-Gaussian modes up to the TEM <sub>2,2</sub> order. . . . .	19
1.21	Intensity profile of super-Gaussian beams. . . . .	20
2.1	Rays diagram of a lens. . . . .	22
2.2	Refraction through a thin lens. . . . .	23
2.3	Refraction through a thick lens. . . . .	24
2.4	Rays trajectory through a thick lens. . . . .	25
2.5	Correct (left) and wrong (right) orientations of a plano-convex aiming at minimizing the spherical aberrations. . . . .	26
2.6	Example of the five rays trajectories for the Gaussian beam ray-equivalent model of a laser source. . . . .	27
2.7	Gaussian beam and five rays equivalent model propagating through a thin lens ( $f = 15$ mm) placed at 10 mm from the source. . . . .	28

2.8	Gaussian beam and five rays equivalent model propagating through two thin lenses placed at 10 mm ( $f_1 = 15$ mm) and 50 mm ( $f_2 = 25$ mm) from the source. . . . .	29
2.9	Plano-convex thick lens. . . . .	30
2.10	Gaussian beam and five rays equivalent model propagating through a thick lens placed at 10 mm from the source. . . . .	31
2.11	Five rays equivalent model of a Gaussian beam propagating through a thick lens placed at 150 mm from the source. . . . .	32
2.12	Gaussian beam and five rays equivalent model propagating through a thin lens ( $f = 10$ mm) placed at 10 mm from the source. . . . .	33
2.13	Gaussian beam and five rays equivalent model propagating through a thick lens placed at 11.6 mm from the source. . . . .	34
2.14	Five rays equivalent model of an off-axis Gaussian beam focusing through a thick lens placed at 11.6 mm from the source. . . . .	35
2.15	Five rays equivalent model of an off-axis Gaussian beam collimating through a thick lens placed at 11.6 mm from the source. . . . .	36
2.16	Off-axis beam focusing through a thick lens placed at 11.6 mm from the source provided by TracePro. . . . .	36
2.17	Off-axis beam collimation through a thick lens placed at 11.6 mm from the source provided by TracePro. . . . .	37
3.1	Gaussian fitting of the intensity function extrapolated from the image related to the He-Ne beam at $z = 100$ mm from the laser output. . .	39
3.2	Astigmatism of He-Ne laser source. . . . .	41
3.3	Comparison between measured and simulated spot sizes of the He-Ne laser. . . . .	41
3.4	Setup mounted to evaluate the effect of a focusing spherical lens on the He-Ne beam. . . . .	42
3.5	Comparison between measured and simulated spot sizes of the He-Ne laser through a thin spherical lens. . . . .	43
3.6	Setup mounted to evaluate the effect of a focusing cylindrical lens on the He-Ne beam. . . . .	44
3.7	Comparison between measured and simulated spot sizes of the He-Ne laser through a thick cylindrical lens. . . . .	44
3.8	CMOS camera image of a green laser pointer beam. . . . .	45
3.9	Gaussian fitting of the intensity function extrapolated from the image related to the green laser beam at $z = 30$ mm from the laser output. .	46
3.10	Setup for green laser pointer characterization. . . . .	47
3.11	Astigmatism of green laser pointer. . . . .	47
3.12	Comparison between measured and simulated spot sizes of the green laser pointer. . . . .	48
3.13	Setup mounted to evaluate the effect of a focusing spherical lens on the green laser pointer. . . . .	49
3.14	Comparison between measured and simulated spot sizes of the green laser through a thin spherical lens. . . . .	50

3.15	Setup mounted to evaluate the effect of a focusing cylindrical lens on the green laser pointer. . . . .	51
3.16	Comparison between measured and simulated spot sizes of the green laser through a thick cylindrical lens. . . . .	51
4.1	Multi-emitter laser diode module. . . . .	53
4.2	Reference scheme for the laser diode module. . . . .	54
4.3	Main GUI to set the simulation parameters. . . . .	55
4.4	Module chips array. . . . .	56
4.5	GUI to choose the desired chips location. . . . .	56
4.6	GUI to choose the lens type. . . . .	57
4.7	GUIs to choose the lenses parameters. . . . .	57
4.8	Example of report file automatically generated by the software. . . . .	58
4.9	Laser diode radiation model. . . . .	59
4.10	Laser diode source emission. . . . .	60
4.11	Source analysis reference scheme. . . . .	61
4.12	Beam captured by the CCD camera. . . . .	61
4.13	Histograms of collected data along the beam two directions. . . . .	62
4.14	PDF of SA and FA divergence angles. . . . .	62
4.15	Comparison between measured and simulated PDF of the spot sizes. . . . .	63
4.16	Chip beams of the module at $z = 20$ mm from the sources. . . . .	65
4.17	Module radiation incident on the fiber lens. . . . .	65
4.18	Beam focalised in the fiber core by one fiber lens. . . . .	66
4.19	Beam focalised in the fiber core by two fiber lenses. . . . .	67
4.20	Beam irradiance at the fiber lens for $EFL_{FAC} = 0.3$ mm; $EFL_{SAC} = 24$ mm (left) and $EFL_{FAC} = 3$ mm; $EFL_{SAC} = 12$ mm (right). . . . .	68
4.21	First module configuration: Yu outcome. . . . .	69
4.22	First module configuration: field at fiber lens and in fiber core. . . . .	70
4.23	Second module configuration: Yu outcome. . . . .	71
4.24	Second module configuration: field at fiber lens and in fiber core. . . . .	71
4.25	Third module configuration: Yu outcome. . . . .	72
4.26	Third module configuration: field at fiber lens and in fiber core. . . . .	72
4.27	Fourth module configuration: Yu outcome. . . . .	73
4.28	Fourth module configuration: field at fiber lens and in fiber core. . . . .	74
4.29	Fifth module configuration field at fiber lens and in fiber core. . . . .	75
4.30	Sixth module configuration field at fiber lens and in fiber core. . . . .	75
4.31	Seventh module configuration: field at fiber lens and in fiber core. . . . .	77
5.1	Examples of beam shaping [34]. . . . .	78
5.2	Two equal round wedge prisms. . . . .	80
5.3	Superimposition of beam profiles in different time stamps produced by two round wedge prisms rotating at same (left) and at different speeds (right). . . . .	80
5.4	Long-exposure photographs provided by Thorlabs of beam profiles produced by two round wedge prisms rotating at same (left) and at different speeds (right). . . . .	80
5.5	Axicon operation scheme. . . . .	81

---

5.6	Ray equivalent model of beam propagation through an axicon. . . . .	82
5.7	Bessel beam intensity. . . . .	83
5.8	Side view of depth of focus where the Bessel beam is generated. . . . .	83
5.9	Power-rays equivalent model of the axicon input beam intensity. . . . .	84
5.10	Annular beam intensity profile in far field region. . . . .	85
5.11	Laser line example. . . . .	86
5.12	Nelder-Mead simplex method flowchart. . . . .	87
5.13	Particle swarm flowchart. . . . .	88
5.14	Example of laser line optimization output provided by the algorithm <i>fminsearch</i> implementing 30 chips. . . . .	89
5.15	Disassembled module suitable to test the cutting properties of a single chip. . . . .	90
5.16	Configuration employing the SAC with the longest focal length (50 mm). . . . .	91
5.17	Microscope photographs of the paper cutting obtained in the 20 mm SAC focal length configuration in 200 ms (left) and in 500 ms (right). . . . .	92
5.18	S322C power-meter employed to perform the power measurement of an infrared radiation. . . . .	92

# List of Tables

1.1	Source parameters for cross section simulation. . . . .	17
2.1	Source parameters. . . . .	28
2.2	Fig. 2.7 output parameters. . . . .	29
2.3	Fig. 2.8 output parameters. . . . .	30
2.4	Thick lens parameters. . . . .	30
2.5	Fig. 2.10 output parameters. . . . .	31
2.6	Fig. 2.11 output parameters. . . . .	32
2.7	Source parameters. . . . .	32
2.8	Fig. 2.12 output parameters. . . . .	33
2.9	Thick lens parameters. . . . .	34
2.10	Fig. 2.13 output parameters. . . . .	35
2.11	Thick lens output parameters in off-axis propagation. . . . .	36
3.1	Thorlabs DCC3260C sensor characteristics. . . . .	38
3.2	Uniphase 1105/P specifications. . . . .	40
3.3	He-Ne source measured parameters. . . . .	42
3.4	He-Ne through a spherical lens - experimental and analytical comparison. . . . .	43
3.5	He-Ne through a cylindrical lens - experimental and analytical comparison. . . . .	45
3.6	CPS520 specifications. . . . .	45
3.7	Experimental and expected results comparison for green laser source. . . . .	48
3.8	Experimental and expected BPP for green laser source. . . . .	48
3.9	Experimental and analytical results comparison for spherical lens setup. . . . .	50
3.10	Experimental and analytical results comparison for cylindrical lens setup. . . . .	51
4.1	Input and quality parameters of the laser diode source. . . . .	60
4.2	Mean and variance divergence angles along the beam axes. . . . .	63
4.3	Error analysis results. . . . .	63
4.4	Parameters of the laser diode module example. . . . .	64
4.5	Power entering the fiber lens in different collimating lenses configurations. . . . .	68
4.6	Parameters of first module configuration with wavelength = 450 nm and stack height = 2.9 mm. . . . .	70
4.7	First module configuration outputs with fiber core diameter = 105 $\mu\text{m}$ and NA = 0.22. . . . .	70
4.8	Parameters of second module configuration with wavelength = 920 nm and stack height = 0.4 mm. . . . .	71

---

4.9	Second module configuration outputs with fiber core diameter = 105 $\mu\text{m}$ and NA = 0.22. . . . .	72
4.10	Parameters of third module configuration with wavelength = 450 nm and stack height = 2.9 mm. . . . .	73
4.11	Third module configuration outputs with fiber core diameter = 105 $\mu\text{m}$ and NA = 0.15. . . . .	73
4.12	Parameters of fourth module configuration with wavelength = 450 nm and stack height = 2.9 mm. . . . .	74
4.13	Fourth module configuration outputs with fiber core diameter = 105 $\mu\text{m}$ and NA = 0.22. . . . .	74
4.14	Fifth module configuration outputs with fiber core diameter = 105 $\mu\text{m}$ and NA = 0.22. . . . .	75
4.15	Parameters of sixth module configuration with wavelength = 450 nm and stack height = 0.9 mm. . . . .	76
4.16	Sixth module configuration outputs with fiber core diameter = 105 $\mu\text{m}$ and NA = 0.22. . . . .	76
4.17	Seventh module configuration outputs with fiber core diameter = 105 $\mu\text{m}$ and NA = 0.15. . . . .	77
5.1	Parameters of round wedge prism. . . . .	79
5.2	Parameters of axicon. . . . .	82
5.3	Laser line system input parameters. . . . .	86
5.4	Optimization algorithms results comparison. . . . .	89
5.5	Laser diodes measured power. . . . .	93

# Chapter 1

## Introduction To Lasers

The purpose of the first chapter is to provide an overview on lasers, especially on their evolution in the last few decades and their operating principles. Successively, a concise scenario about high power lasers and beam combining techniques is provided. In the thesis project the Gaussian beam theory is adopted to describe the laser diode emission. Nevertheless, it is necessary to highlight that a Gaussian beam is just an approximation: the output of a laser is assumed to have an intensity profile following an ideal Gaussian distribution, but actually the emitted light presents always a deviation from ideality.

### 1.1. Lasers historical evolution

The word *laser* is an acronym for *Light Amplification by Stimulated Emission of Radiation*. The first device capable of generating light basing on the stimulated emission process has been realised in 1960 by Theodor H. Maiman, who demonstrated the first solid state laser (Fig. 1.1).

Later, in the same year, a gas laser was developed using a mixture of helium and neon. Successively, in the 70s, GaAs semiconductor lasers operating at room temperature were realised, and more and more improvements followed allowing new and innovative device operations, e.g. evolving from pulsed mode to continuous wave (CW) mode.

The main laser categories are listed below.

**Solid state lasers** The active medium of the first realised class of lasers is in the solid state. Typically, rare-earth ions are introduced in a host material, as glass or crystals, which is also in the solid state. This kind of laser relies on optical pumping, provided initially by lamps and then, more recently, also by other lasers, especially laser diodes, capable of supplying high power up to the kilowatt range. Different solid state lasers applications require specific wavelength and power level, then the pumping system must be designed properly to provide the requested power. The primary applications include surgery (specifically the popular Nd:YAG laser is largely employed in cataract and glaucoma treatments) and welding oriented to material processing.



Figure 1.1: First laser: Maiman's ruby laser, 1960.

**Gas lasers** The gas lasers are named after the nature of their gain medium, which is a gas or a mixture of different gases. Gas lasers are mostly pumped by electric discharge, which causes the electrons to collide with the gas atoms, that, as a consequence, are excited to higher meta-stable states [2].

The most widespread gas laser is based on a combination of helium and neon gases and commonly emits in the red portion of the visible range.

**Semiconductor lasers** Semiconductor lasers belong to the category of solid state lasers, but found a proper class based on the use of semiconductor as gain medium. Conversely to the solid state lasers, semiconductor lasers are more compact and efficient; moreover the excitation takes place through current injection. The optical gain is achieved by generating photons and, according to the stimulated emission phenomenon, the number of photons increases leading to light amplification.

Semiconductor laser diodes are *pn* junctions where electrons and holes recombine in a direct bandgap semiconductor in order to reach the lasing condition. Since laser diodes are realized by exploiting wafer scale processes, they are much more inexpensive in comparison with the other laser kinds. The main applications of the laser diodes are in telecommunications and in pumping of optical systems, e.g. fiber lasers.

**Fiber lasers** Fiber lasers rely on an optical fiber doped with rare-earth elements (like erbium, ytterbium or neodymium) as active gain medium. The primary feature is that they provide light amplification without exploiting a resonant cavity. They are optically pumped usually through semiconductor lasers, and suitable beam coupling devices are needed to inject the pumped radiation into the fiber core.

Nowadays, the fiber lasers are able to produce several tens of kilowatts.

Fiber lasers were mostly employed in telecommunication systems and, since a few years, they are used in material processing.

## 1.2. Laser diode operating principle

The light emitted by a laser diode is produced by a tiny active layer that acts as gain medium, where the radiation is confined by means of the variation of the different semiconducting layers refractive index. Basically, the gain medium of the device is a direct bandgap semiconductor, or rather the maximum and minimum of respectively the valence band (VB) and the conduction band (CB) occur at the same  $k$  wave vector. Indeed, this type of semiconductor is able to directly interact with photons by producing an energy of the same magnitude of the energy gap, defined as the forbidden gap where electronic states cannot exist; moreover, since the only particles involved are electrons and photons, the interaction probability is high [3]. As shown in Fig. 1.2, the silicon, which is the most widespread semiconductor in electronics, is an indirect bandgap semiconductor, hence the transition among CB and VB relies also on other particles, the so called phonons. Consequently, silicon cannot be used in optoelectronic devices such as lasers. On the contrary, alloys of direct bandgap semiconductors are employed: gallium-arsenide (GaAs) for laser diodes operating in a range of 0.7-1  $\mu\text{m}$ , indium-phosphide (InP) for laser diodes operating in a range of 1.3-1.55  $\mu\text{m}$  and gallium-nitride (GaN) for blue lasers (0.36-0.48  $\mu\text{m}$ ).

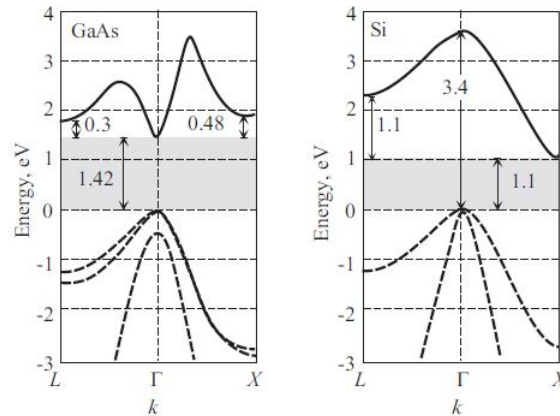


Figure 1.2: Example of direct (GaAs) and indirect (Si) bandgap semiconductor [3].

According to quantum mechanics, a non-degenerate semiconductor, thus in thermal equilibrium condition, is described by a band structure model, where electrons and holes occupy energy levels close to the energy band gap. When the semiconductor is out of equilibrium, or in other words an external source is applied, a rearrangement of the carrier population takes place. As a result, electrical current starts to flow due to the carriers motion and transitions between two energy states occur, in particular electrons recombine with holes, generating photons. The latter are mainly confined in the active layer and they are involved in turn in the so-called *stimulated emission*, the process that leads to producing a large number of photons, in which an incident

photon causes the recombination of an electron-hole pair and, as a consequence, an additional photon is generated (Fig. 1.3).

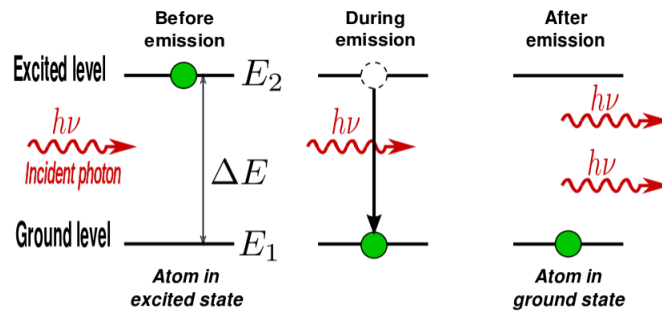


Figure 1.3: Photon stimulated emission phenomenon [4].

Conversely to LED, where the primary phenomenon is the *spontaneous emission*, the stimulated photons are coherent [3], thus they contribute to the amplification of the laser output beam, because they have the same wavelength and the same energy of the incident photons. It has to be reminded that also the spontaneous emission contributes to the lasing; nevertheless, above the lasing threshold, the number of photons generated by spontaneous emission and the associated power are much lower.

In order to achieve light amplification an optical cavity has to be exploited. The simplest cavity is made up of a gain medium placed between two mirrors (Fig. 1.4). The pump is provided by current injection and light amplification follows according to the stimulated emission phenomenon.

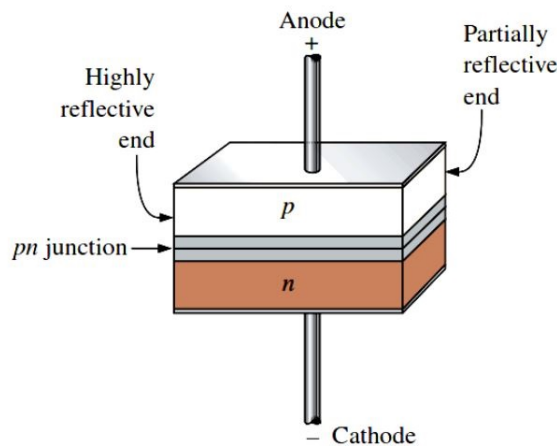


Figure 1.4: Laser diode optical cavity.

In the cavity a feedback mechanism occurs because of beam multiple reflections by means of the two mirrors; since a very high reflective mirror, providing about 99% of reflections, and another mirror with a reflectivity of about 30% are provided [1], photons travelling along the optical axis  $z$  undergo different processes: some of them

are back reflected inside the resonant cavity in order to be involved in the stimulated emission; other photons could be absorbed by the material or could undergo non-radiative recombination events; the remainders turn into the output laser beam. This structure is also called laser oscillator or optical resonator.

In order to realise the resonator, the laser optical gain must overcome the optical losses to prevent the device from switching off. The constrain is to satisfy the so called Barkhausen criterion, or rather at each round-trip the loop gain amplitude must be equal to 1 and, at the same time, the loop gain phase has to be an integer multiple of  $2\pi$ . When the criterion is satisfied, just the light patterns that remain stable at every round-trip can exist in the cavity; these are called *modes*.

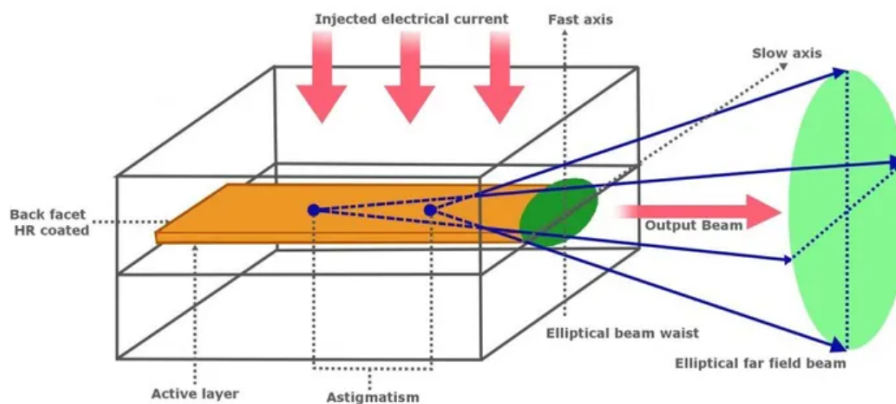


Figure 1.5: Laser diode emission [1].

The output beam of a laser diode resonant cavity is characterized by asymmetric dimensions because of the rectangular shaped cross section of the active layer: the length along the vertical direction is about one micron, whereas it is few microns in the other direction in low power diodes used in telecommunications and hundreds of microns for the high power version. As a result, the output radiation has an elliptical shape, as depicted in Fig. 1.5.

### 1.3. High-power lasers

High-power lasers are characterized by a power higher than at least few tens of watts. A great number of high-power laser types can be identified, such as solid-state, gas or fiber lasers, and the main applications in which they are involved belong to the following fields: material processing (e.g. cutting and welding of metals), medical and military. A pie chart in Fig. 1.6 shows the different sectors where the high-power lasers are exploited.

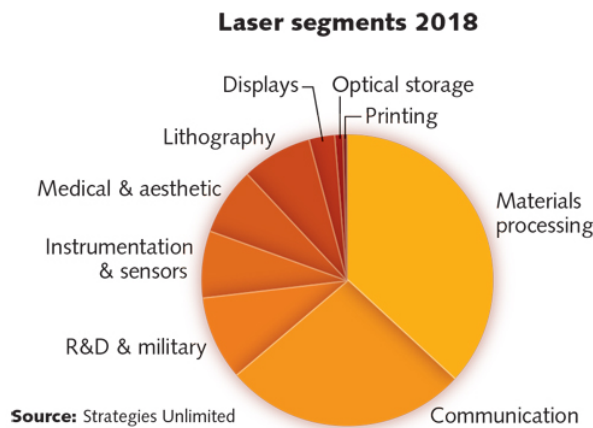


Figure 1.6: High power laser applications [7].

As for the material processing, several laser kinds are adopted, but the most employed laser up to 2013 was the CO<sub>2</sub> (*carbon dioxide*) laser, a gas laser exhibiting high emission at 10 μm and fine cutting for thick metallic workpieces.

However, a competition with the other laser types arose because the CO<sub>2</sub> laser has a very low *wall plug efficiency*, in other words the amount of electrical power converted into optical one is very low [5][6].

This is one of the main reasons why fiber lasers have been used in the industrial applications, leading to wide employment of laser technologies.

As shown in the bar chart in Fig. 1.7, fiber lasers are prevailing in the worldwide industrial laser revenues since 2013, when the fiber laser production outdid the CO<sub>2</sub> laser one [8]. Indeed, they are suitable for high power applications.

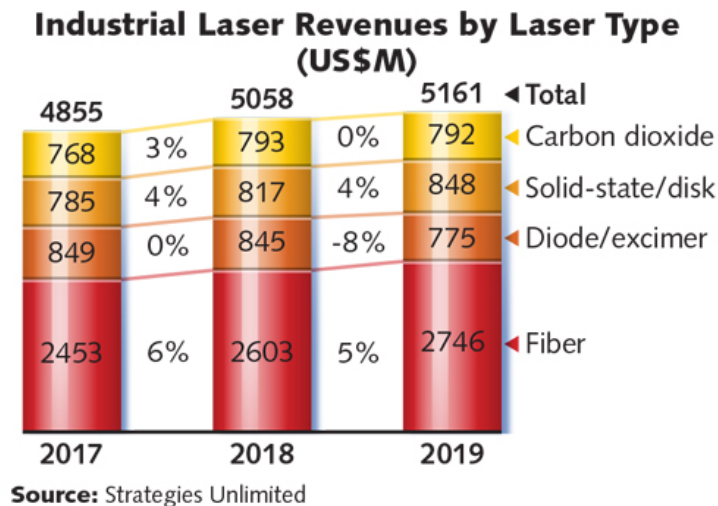


Figure 1.7: High power laser market in the last few years [7].

The revolution of the high-power fiber lasers has been made possible because of the development of the high-power laser diode modules, which have substituted the single semiconductor laser. A more detailed explanation of high-power laser diode module can be found in the Chapter 4.

**CO<sub>2</sub> lasers** One of the first gas lasers to be realised has been the carbon dioxide (CO<sub>2</sub>) laser. The emitted radiation falls in the infrared range and the gain medium is made up of a mixture of carbon dioxide, hydrogen, nitrogen, helium and xenon. Being an optical resonator, clearly the CO<sub>2</sub> laser cavity contains two concave mirrors besides the active medium (Fig. 1.8). Generally, a CO<sub>2</sub> laser is based on a gas discharge providing the energy required for the excitation: nitrogen molecules are excited to a meta-stable level and their excitation is transferred to CO<sub>2</sub> molecules, which are mostly involved in laser transitions, whereas helium removes heat [6].

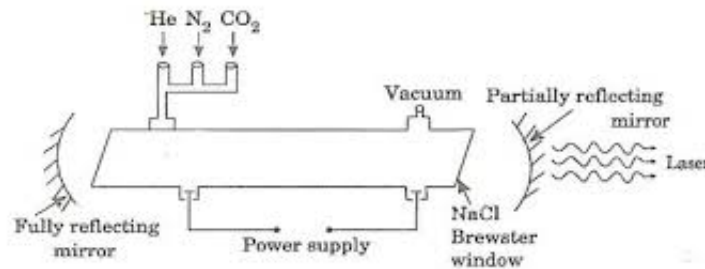


Figure 1.8: CO<sub>2</sub> laser operation scheme.

CO<sub>2</sub> lasers are employed in several fields, like material processing and medical surgery, because the emitted wavelength is compatible with some materials spectrum of absorption. One of the main applications is cutting: if a thick material must be cut, CO<sub>2</sub> lasers are the best devices to achieve the goal in the shortest time. However, they dissipate a lot of power because of the large heat quantity to be removed and the efficiency is not so high (about 10-20%): thus, the wall plug efficiency is very low. These are the main reasons why CO<sub>2</sub> lasers have been overcome by fiber lasers.

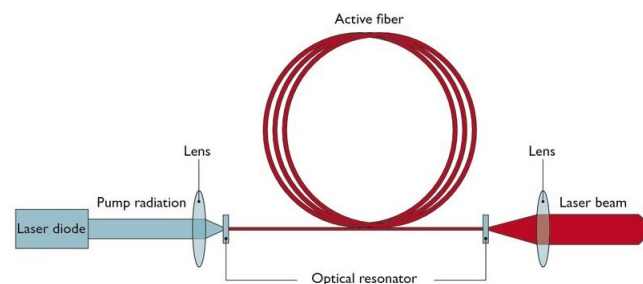


Figure 1.9: Fiber laser operation scheme.

**Fiber lasers** Fiber lasers are mainly characterized by an optical fiber as gain medium, whose glass core is doped by rare-earth elements. Due to such elements, high optical gain is produced inside the fiber, which can then be characterized by the adjective “active”; moreover, wide emission wavelength tunability is provided by means of the core doping.

The pumped light is usually fed by a semiconductor laser diode or by a laser-based module (Fig. 1.9); beam coupling devices must be employed to transfer the pump

output power to the fiber core [9]. Fiber lasers are marked out by brightness higher than the pump light one, whereas the power of the the output radiation is slightly lower due to the attenuation caused by the combining devices and mainly to the non-unitary laser intrinsic efficiency.

As shown in Fig. 1.10, related to erbium-doped fiber, the fiber laser is pumped by a source with a given wavelength of 980 nm or 1480 nm. The energy band diagram includes a ground state and two excited states. The state related to the doping is unstable, indeed, once absorbed the photons constituting the incident radiation, the electrons promoted in the upper state decay in the lower excited one. Thereafter, stimulated emission occurs, leading to an emitted radiation falling into a spectrum between 1520 nm and 1570 nm, or rather inside the C-band of the optical communication wavelength bands. The large emission spectrum is caused by the presence of the doping ions inside the fiber glass, that consequently is characterized by broadened energy states.

The output radiation is highly coherent and low-noisy. The emitted power clearly depends on the fiber kind, but, generally, the fiber laser power should be quite low if a single mode fiber is exploited, whereas for higher powers the core area must be larger, allowing multimode propagation.

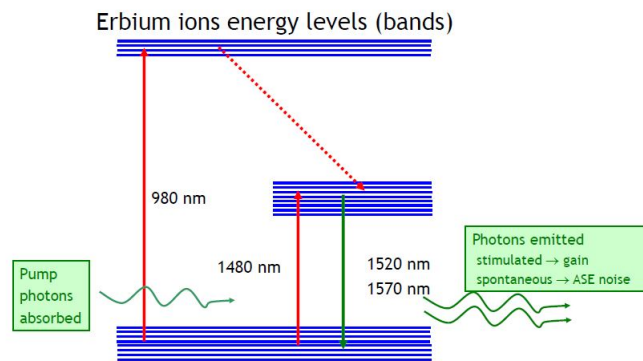


Figure 1.10: Fiber laser emission.

Fiber lasers are more compact than the solid-state or  $\text{CO}_2$  lasers and are electrically and optically more efficient. Finally, due to high area to volume ratio, fiber cooling for heat management is easier and, as a consequence, the power scaling is allowed [10].

### 1.3.1. Beam combining for laser modules

The growing request for high power laser applications implies the development of new techniques in order to increase the laser system output power.

It could be naively thought that a power boost may be obtained by extending the laser active region size, but the consequences would be non-linear phenomena, increase of laser size and costs. For semiconductor lasers, a feasible solution to achieve a large amount of output power is to develop an array of many lasers, thus realising high-power laser diode modules. An example of a laser diode module available on the market is proposed in Fig. 1.11.

The purpose is to combine the beams generated by the array to obtain a single beam propagation characteristics [11]: the radiations emitted by laser diodes are optically shaped, then they are aligned and combined together by optical components in order to get at the output a focused beam with high power density. The number of chips is set by the module output power, which may reach also thousands of watts, and by laser beam parameters (divergence angle, beam waist etc.).



Figure 1.11: Laser module package.

A constraint of the beam combining is to control the beam quality, because it limits the number of the array elements, according to the intended application. The parameter employed to characterize the beam quality is the beam parameter product (BPP), defined as the product of the far field divergence angle (half-angle) and the beam waist (half of the source diameter) of the laser emission. As the beam quality impacts on the beam capability to be focused, for example reaching a certain spot size given a fixed divergence angle, the lower the BPP, the higher the beam quality.

Beam combining techniques are classified into coherent and incoherent, with the main difference in the phase stability control, that must be strictly guaranteed in the first case; the most widespread technique is the incoherent one, since it is the simplest and demands no phase control.

In Fig. 1.12 a preliminary classification of beam combining is proposed:

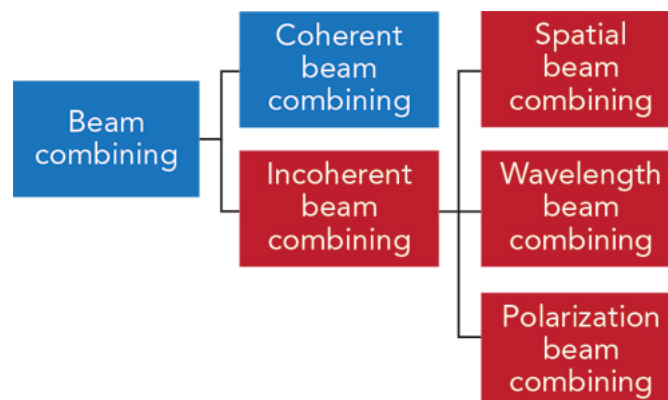


Figure 1.12: Classification of the beam combining [12].

**Coherent combining** One of the possible power scaling methods is the coherent beam combining, where out of multiple beams a single beam with higher power is obtained. The key point is to produce kilowatts of power by preserving beam quality and increasing the brightness (which will be defined in details in Chapter 4). Indeed, the main advantage is that, theoretically, several emitters can be combined by maintaining the beam quality of a single beam.

The result of this technique is a constructive interference in far field region among the coupled beams; however, phase noise is always present and, since it causes the beams to lose the coherence and to interfere destructively, it reduces the combined beam performances. Therefore, the phase noise effect of each beam should be prevented and carefully controlled. Furthermore, in order to achieve the right kind of interference, the emissions should have the same wavelength. As a result, coherent combining is usually employed when a narrow emission spectrum is required.

The reasons why coherent beam combining is not very popular in high power applications are explained by the following limiting factors [13]: phase coherence must be achieved, hence beam phase control is always required, leading to expensive system implementation; nonlinear effects, like the stimulated Brillouin scattering or Raman scattering and mode instabilities.

**Incoherent combining** Conversely to the coherent case, the incoherent combining consists in obtaining a single beam by summing several lasers that do not interfere with each other. The leading advantage of incoherent beam combining is the lack of phase stability control, that could complicate the whole system handling enough to prevent the attainment of stable operations at high power levels. As depicted in Fig. 1.12, the incoherent combining is in turn classified into [12]:

- spatial beam combining;
- wavelength beam combining;
- polarization beam combining.

In the spatial beam combining technique (Fig. 1.13) many chips, emitting the same (or different) wavelength, are spatially superimposed in order to get a multi-emitter module. This combining method is the only one exploited in the thesis project and a more substantiated explanation can be found in Chapter 4.

The wavelength beam combining (Fig. 1.14) is based on the coupling of different wavelengths through wavelength-sensitive combiners, such as dichroic mirrors, prisms or gratings. As a result, a co-linear beam is achieved by properly deflecting beams according to their wavelength. The output radiation of this technique is marked out by multiple wavelengths, but each laser emission wavelength must be stabilized to avoid a reduction of beam quality.

The last incoherent technique is the polarization beam combining (Fig. 1.15), allowing the combination of orthogonally polarized lights through a beam splitter cube in order to provide an unpolarized output beam [14]. Particularly, the polarized light beams are transmitted to different sides of a polarization beam splitter, thus

obtaining the reflection of one polarization and the transmission of the other. As a result, the output beams propagate in the same direction and they are incoherently summed leading to an unpolarized radiation with the same beam quality and almost double power with respect to that carried by the single input radiations.

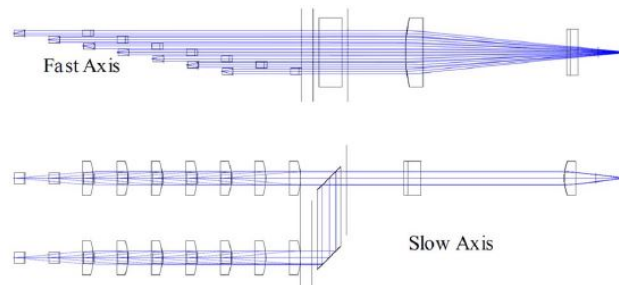


Figure 1.13: Spatial [15] beam combining techniques.

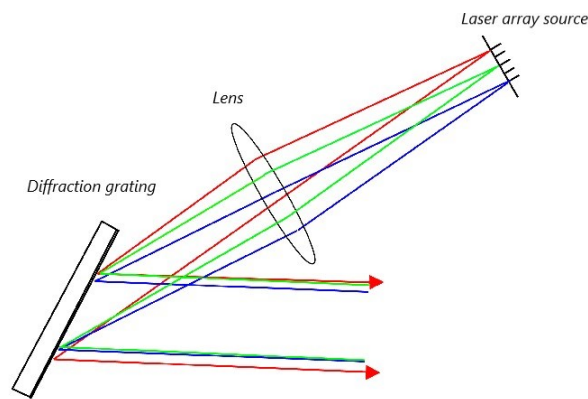


Figure 1.14: Wavelength beam combining techniques.

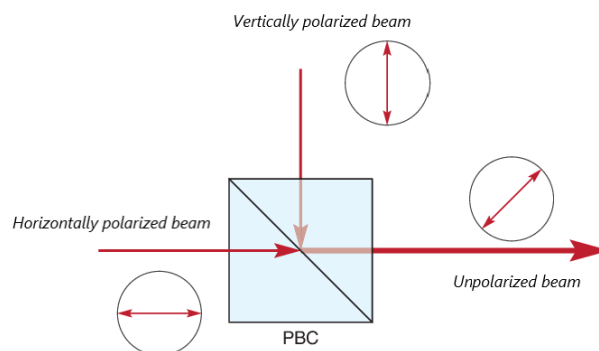


Figure 1.15: Polarization beam combining techniques.

## 1.4. Gaussian beams

As is well known, the emitted light of most lasers is an electromagnetic wave showing an intensity profile comparable to a Gaussian distribution; hence, the laser output is basically identified by a Gaussian beam. Before explaining it and the related parameters, it is appropriate to understand the main reasons why the Gaussian beam is introduced as an approximated solution of the so called *wave equation*.

The Helmholtz equation is the wave equation in a time independent form and it is expressed by the following formula:

$$(\nabla^2 + k^2)E(\vec{r}) = 0; \quad (1.1)$$

where  $k = \omega/c$  is the wave number,  $\omega$  is the angular frequency and  $E(\vec{r})$  is the complex field amplitude. In the case of homogeneous media or free space, the fundamental solution of the Helmholtz equation is the plane wave, a field depicted by planar wavefronts:

$$E(\vec{r}) = E_0 e^{-ik \cdot \vec{r}} \quad (1.2)$$

However, an approximated solution of the Helmholtz equation is needed because a plane wave leads to divergent wavefronts, since its electric and magnetic fields extend to infinity; as a consequence, it carries an infinite amount of energy [16]. In other words, a plane wave cannot be physically realized. The adopted approximation is the *paraxial Helmholtz equation*, which can be found by looking for the solution in the form of an envelope:

$$E(\vec{r}) = E_0(\vec{r}) e^{-ik \cdot \vec{r}} \quad (1.3)$$

where  $E_0(\vec{r})$  is a slowly varying function of  $z$  in terms of wavelength, or rather  $\frac{\partial E}{\partial z} \ll E/\lambda$ . By substituting Eq. 1.3 in Eq. 1.1 and by expanding the Laplace operator, the result is:

$$\left( \frac{\partial^2}{\partial x^2} + \frac{\partial^2}{\partial y^2} \right) E_0(\vec{r}) e^{-ik \cdot \vec{r}} - 2ik e^{-ik \cdot \vec{r}} \frac{\partial}{\partial z} E_0(\vec{r}) + e^{-ik \cdot \vec{r}} \frac{\partial^2}{\partial z^2} E_0(\vec{r}) = 0$$

According to the main assumption, the second order partial derivative along  $z$  is neglected. As a result, the paraxial Helmholtz equation (Eq. 1.4) is obtained.

$$\left( \frac{\partial^2}{\partial x^2} + \frac{\partial^2}{\partial y^2} - 2ik \frac{\partial}{\partial z} \right) E(\vec{r}) = 0 \quad (1.4)$$

The solutions of the approximated Helmholtz equation are paraboloid waves which are called propagation modes, in other words electric field distributions showing constant transverse intensity profile during the propagation. In the laser contest, these modes are the Gaussian beams.

Several modes can exist, but, at first, only the fundamental mode is analysed.

The equation describing a Gaussian beam is [17]:

$$E(x, y, z) = E_0 \frac{w_0}{w(z)} \exp \left[ -\frac{r^2}{w^2(z)} \right] \cdot \exp \{ -j [kz - \phi(z)] \} \cdot \exp \left[ -j \frac{kr^2}{2R(z)} \right] \quad (1.5)$$

The first exponential, the peak field amplitude  $E_0$  and the decay factor  $w_0/w(z)$  constitute the amplitude factor, whereas the following exponentials are respectively the longitudinal and radial phase factors. Going into detail, the amplitude factor explains how the field amplitude changes as a function of the spatial coordinate  $r$  and of the propagation direction  $z$ , while the phase factors describe the change in the beam phase along the optical axis  $z$  and the shape of the wavefront. Indeed, Gaussian beams are characterized by wavefronts which behave like plane waves where the spot size is minimum; then, moving away from this point, wavefronts modify into spherical.

A representation of the beam distribution and of its main parameters is proposed in Fig. 1.16.

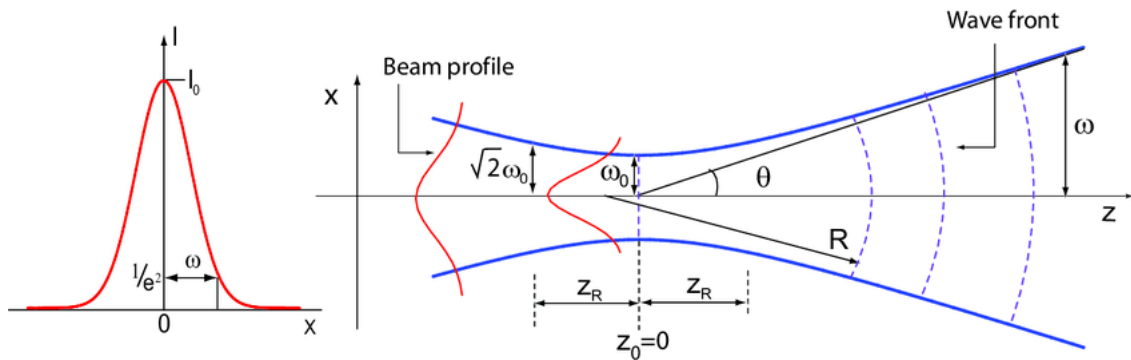


Figure 1.16: Gaussian beam intensity and amplitude distribution [18].

Referring to Eq. 1.5, the primary parameters are the following [17]:

- the beam radius of curvature  $R(z)$ , describing the wavefront of the beam along the propagation direction  $z$

$$R(z) = z \left[ 1 + \left( \frac{z_R}{z} \right)^2 \right] \quad (1.6)$$

- the beam waist  $w_0$ , defined as the minimum point of the beam radius  $w(z)$ ; in other words, it represents the smallest section of the spot size

$$w^2(z) = w_0^2 \left[ 1 + \left( \frac{z}{z_R} \right)^2 \right] \quad (1.7)$$

- the Rayleigh range  $z_R$ , representing the distance along  $z$  from the waist position to the location where the cross section area is doubled

$$z_R = \frac{\pi n w_0^2}{\lambda_0} \quad (1.8)$$

- the divergence angle  $\theta$ , identifying the half angle between the optical axis and the cone-shaped beam curve in far field conditions

$$\theta = \frac{\lambda_0}{\pi n w_0} \quad (1.9)$$

- the Guoy phase  $\phi$ , a correction factor representing the Gaussian phase shift acquired around the focal point

$$\phi(z) = \arctan\left(\frac{z}{z_R}\right) \quad (1.10)$$

In all the introduced formulas, the symbol  $n$  is used for the refractive index of the medium in which the beam is propagating and  $\lambda_0$  is the source wavelength.

As for the beam intensity, it is maximal in the waist position and then decays exponentially (Fig. 1.17). According to Eq. 1.11, the Gaussian intensity (also called irradiance) distribution is perpendicular to the optical axis  $z$  and is proportional to the parameter  $I_0(z)$ , which is the peak irradiance in the beam center depending on the total beam power  $P$ .

$$I(r, z) = I_0 \left(\frac{w_0}{w(z)}\right)^2 \exp\left\{\frac{-2r^2}{w(z)^2}\right\} \quad (1.11)$$

$$I_0 = \frac{2P}{\pi w_0^2}$$

In the previous equations, the beam radius  $w(z)$  is defined as the distance between the beam vertical axis (orthogonal to the optical one) and the point where the intensity level is  $1/e^2 \sim 0.135$  of the peak value. Thus, the beam diameter is twice the intensity value corresponding to the 13.5% of its maximum.

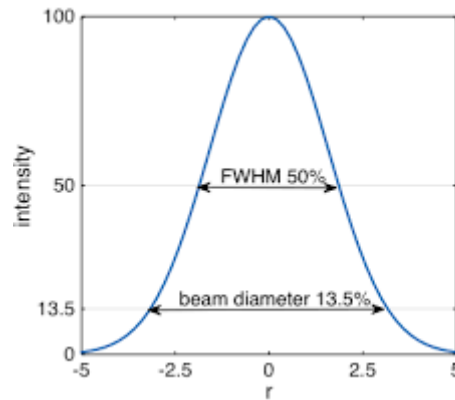


Figure 1.17: Gaussian beam intensity [19].

### 1.4.1. Complex beam parameter

The complex beam parameter  $q(z)$  provides an exhaustive and alternative description of the Gaussian beam. Indeed, the real and imaginary parts of the complex number  $1/q(z)$  specify respectively the phase of the beam and its amplitude.

The  $q(z)$  parameter in a given point  $z$  of the propagation direction and the beam

waist are related as explained in Eq. 1.12 [16], that includes the propagation constant  $k = 2\pi n/\lambda_0$ .

$$q(z) = z - j\frac{k}{2}w_0^2 \quad (1.12)$$

The advantage resulting from the aforementioned representation is that it can exploit the ray transfer matrices (also known as *ABCD* matrices) for the beam propagation through an optical system, composed for example by a cascade of lenses.

Since the complex beam parameter is a perfectly equivalent representation of the Gaussian beam as described by Eq. 1.5, the MATLAB simulations based on  $q(z)$  are not treated in this document because they led to identical results with respect to those presented in Chapter 2.

### 1.4.2. Non-Gaussian beams: $M^2$ factor

The expressions presented in the previous section provide exact results only if the laser beam is perfectly Gaussian, thus requiring a strong ideality that is far from the real world context.

A more realistic description of the laser beam can be carried out by introducing the  $M^2$  factor, a parameter that quantifies the deviation of a real beam from a Gaussian one.

The  $M^2$  of a Gaussian beam is equal to 1, which is the lowest value physically meaningful that the parameter can assume. For instance, according to their typical  $M^2$  value, the low power Helium-Neon lasers emission is a good approximation of an ideal Gaussian beam, leading to a  $M^2$  factor that does not exceed 1.1. On the contrary, in the case of high power and multimode emissions,  $M^2$  may even reach values of 20 or 30 [20].

The  $M^2$  factor can be easily computed once acquainted with the main parameters fully describing the beam:

$$M^2 = \theta \frac{\pi n w_0}{\lambda_0} \quad (1.13)$$

The formulas introduced for the computation of the spot size  $w(z)$  and of the radius of curvature  $R(z)$  are valid also in the presence of a non ideal beam only if the definition of the Rayleigh range is adjusted as follows:

$$z_R = \frac{\pi n w_0^2}{M^2 \lambda_0} \quad (1.14)$$

Eq. 1.9 instead is not correct anymore, since the far field divergence beam depends on the  $M^2$  factor. The value of  $\theta$  can be easily deduced from Eq. 1.13 if all the other parameters are known.

$$\theta = \frac{M^2 \lambda}{\pi n w_0} = \frac{w_0}{z_R} \quad (1.15)$$

Lastly, the intensity distribution law (Eq. 1.11) does not include the  $M^2$  factor because a non-diffraction limited Gaussian beam is typically distinguished by a top-flat field distribution [5].

### 1.4.3. High-power laser diode emission

Because of the rectangular shape of the active layer, the emission of laser diode for high-power application can be approximately factorized into two Gaussian beams moving along the same propagation direction  $z$  and extending along two orthogonal directions, commonly known as *slow axis* (SA) and *fast axis* (FA).

The axes names are related to the beam divergence [21]: moving along the FA direction, the divergence angle is huge because of the narrow height of the active layer (about  $1\ \mu\text{m}$ ), which guarantees a single mode propagation with a  $M^2$  factor approximately unitary; on the contrary, along the SA direction the divergence angle is very small due to the large thickness of the active layer (about  $100\ \mu\text{m}$ ) and, as a consequence, the beam quality decreases, leading to an increase of  $M^2$  factor and to a multi-peaked beam profile.

The FA and SA contributions cause the beam cross section at the emission facet to outline an elliptical shape. The beam intensity profile along the two axes is depicted in Fig. 1.18.

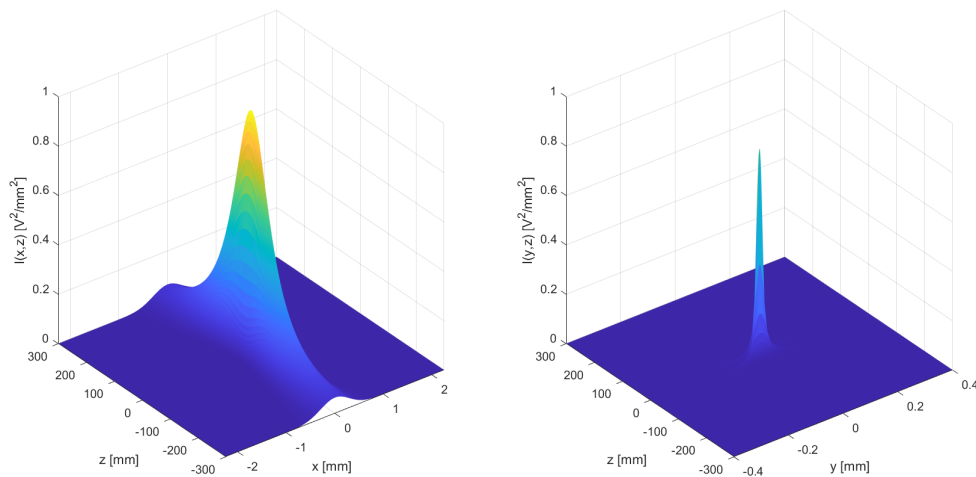


Figure 1.18: Gaussian beam profile along the SA (left) and FA (right).

The beam evolution along the propagation direction  $z$  is illustrated in Fig. 1.19. Initially, close to the source, the cross section area is minimal and it mainly extends along the SA direction; as the beam propagates, the cross section enlarges along the two transverse axes and clearly the beam mostly extends in the FA direction, since the FA divergence angle is much larger than the SA one.

In conclusion, during the propagation a rotation of  $\pi/2$  of the initial cross section occurs.

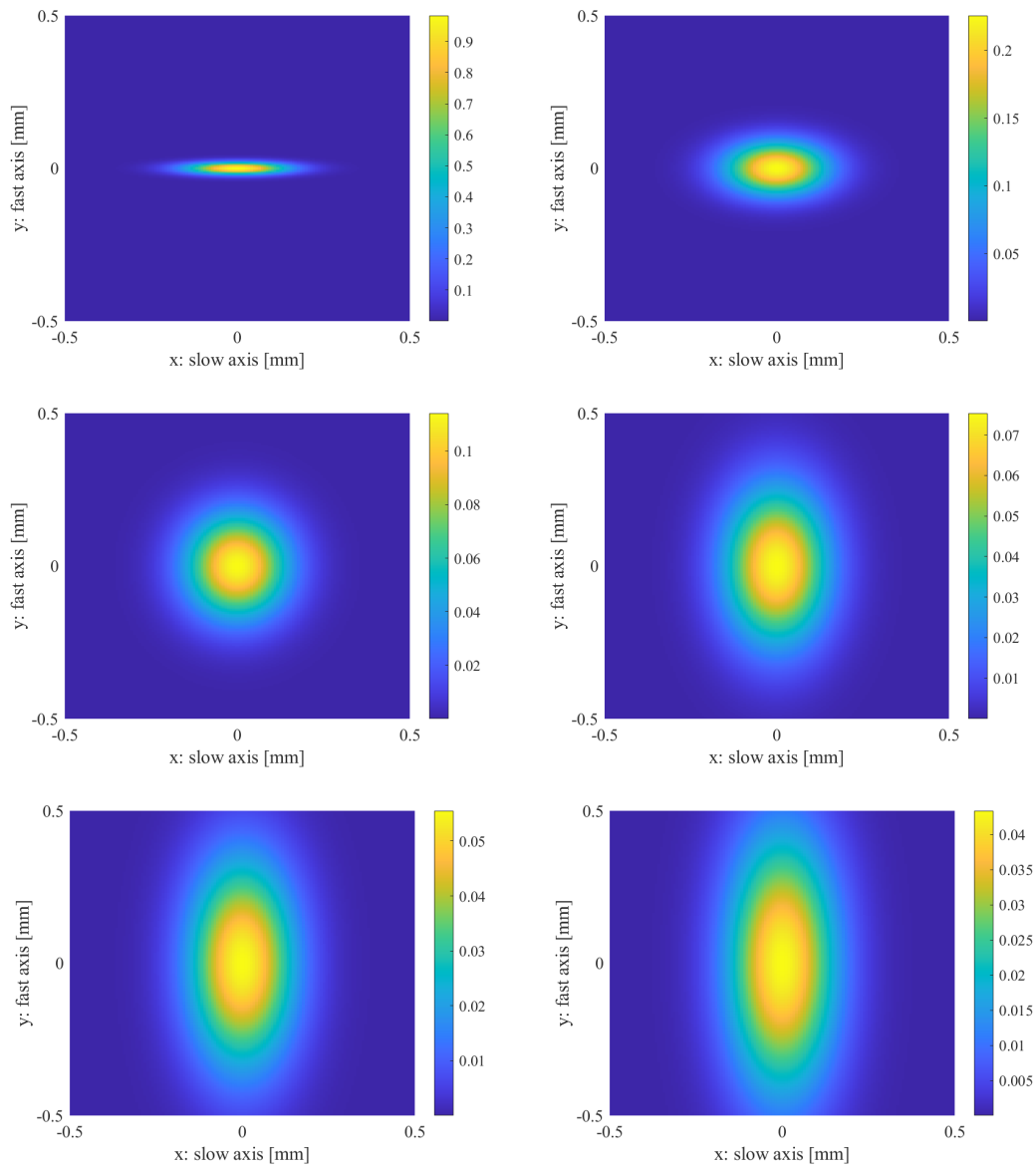


Figure 1.19: Gaussian beam cross section when changing the distance between the source point ( $z = 0$  mm) and the observation point with a step of 6 mm up to  $z = 30$  mm.

The *colorbars* associated to the simulation pictures in Fig. 1.19, representing the normalized beam intensity, demonstrate how the power intensity of the field naturally decreases if the observation point is moved far from the laser source.

The input parameters (Tab. 1.1) employed to simulate the laser diode emission are:

Table 1.1: Source parameters for cross section simulation.

Wavelength	SA Beam waist	FA Beam waist
900 nm	150 $\mu\text{m}$	20 $\mu\text{m}$

Obviously, such laser diode behaviour must be controlled because the beam in the FA direction spreads very rapidly. This is the reason why many laser diode systems make use of a *fast axis collimator* (FAC) lens close to the active layer facet.

Another drawback of the active layer rectangular shape is the *astigmatism*, or rather the beam waist of the slow axis is different from the fast axis one (see Fig. 1.5). In a single mode laser the astigmatism is typically few  $\mu\text{m}$ .

## 1.5. Higher order modes

As mentioned in the previous section of the chapter, to solve the paraxial Helmholtz equation means to find the laser propagation modes. The modes are characterized by different propagation constants and different intensity profiles; the mode marked out by the simplest intensity profile is defined *fundamental mode*, whereas the others are called *higher-order modes*.

The request to analyse the higher-order modes comes from the laser cavity design, because, even if a single mode laser is designed, distortion of the output laser and a superposition of higher transverse modes may occur due to some cavity design imperfections [22].

### 1.5.1. Hermite-Gaussian modes

Two or more modes characterized by the same propagation constant can undergo the modal decomposition of the propagating beam. A classic decomposition of an arbitrary field distribution consists in the production of a set of the so-called *Hermite-Gaussian modes*, depicted by rectangular symmetry with respect to the optical axis. These TEM modes are approximate solutions of the wave equation in the paraxial conditions (the field intensity must be weak enough to satisfy the approximation) and their formula [23] is:

$$E_{nm}(x, y, z) = E_0 \frac{w_0}{w(z)} \cdot H_n \left( \sqrt{2} \frac{x}{w(z)} \exp \left( -\frac{x^2}{w(z)} \right) \right) H_m \left( \sqrt{2} \frac{y}{w(z)} \exp \left( -\frac{y^2}{w(z)} \right) \right) \cdot \exp \left( -i \left[ kz - (1 + n + m) \arctan \left( \frac{z}{z_R} \right) + \frac{k(x^2 + y^2)}{2R(z)} \right] \right) \quad (1.16)$$

where  $n$  and  $m$  are the order mode referring to the  $x$  and  $y$  directions,  $H_n$  and  $H_m$  are the Hermite polynomials of order  $n$  and  $m$  and the other parameters are the same previously mentioned in Eq. 1.5.

Clearly, the Eq. 1.16 refers to a stigmatic case, thus the spot size  $w(z)$  is the same along the  $x$  and  $y$  directions. On the contrary, in the astigmatic case the spot size has two different components; hence, the Hermite polynomials  $H_n$  and  $H_m$  depend respectively on  $w_x(z)$  and  $w_y(z)$ , whereas the amplitude ratio  $w_0/w(z)$  is factorized as follows:

$$\frac{w_0}{w(z)} = \sqrt{\frac{w_{0x} \cdot w_{0y}}{w_x(z) \cdot w_y(z)}} \quad (1.17)$$

The values of  $n$  and  $m$  provide the beam profile shape along the two directions, leading to a 2D intensity profile.

All the excited modes of a waveguide are Hermite-Gaussian modes, or even the two-dimensional beam profile of a waveguide is the sum of all the excited modes multiplied by the Hermite coefficients, that have different weights in the beam distribution. Also the well known Gaussian beam results from the Hermite-Gaussian modes: precisely, when  $n = m = 0$ , the equation represents the fundamental mode, which is in fact the Gaussian beam with  $M^2 = 1$ . For the higher modes, the  $M^2$  factor is  $1 + 2n$  along the  $x$  direction and  $1 + 2m$  along the  $y$  direction [23].

A series of different Hermite-Gaussian modes is illustrated in Fig. 1.20.

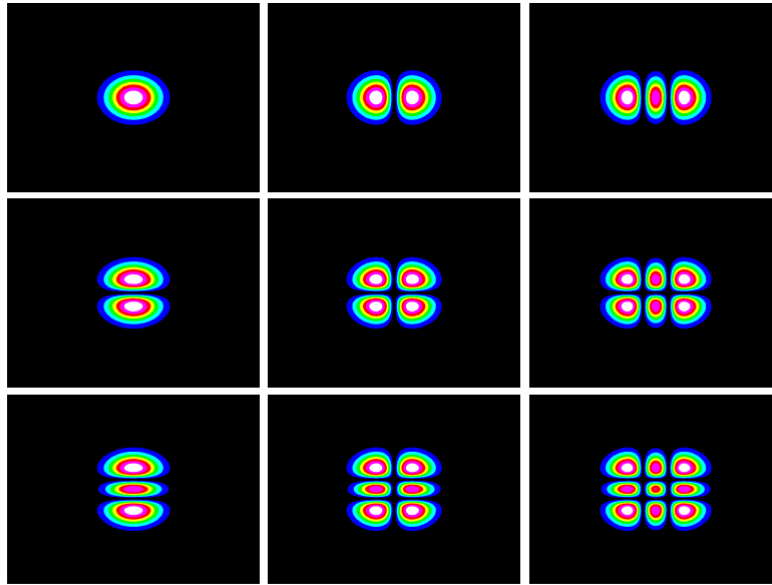


Figure 1.20: Intensity profile of the Hermite-Gaussian modes up to the  $TEM_{2,2}$  order.

By comparing the Hermite-Gauss modes equation with Eq. 1.5, some similarities can be noticed [17]: the amplitude factor and the radial phase exponential are unchanged. However, now the phase shift along the propagation direction depends on the mode order and the field distribution changes according to the Hermite polynomials: the larger the mode number becomes, the larger the field occupancy, or even the spot area. It must be emphasised that, even if the field broadens, the spot size  $w(z)$  is the same for all the depicted modes.

### 1.5.2. Super-Gaussian beams

In specific applications it is required to determine an almost flat intensity profile in order to reduce, for example, intensity variations, even if a non-parabolic shape causes also a reduction of the beam quality. This requirement is satisfied by the so-called *super-Gaussian*, characterized by a flat-top beam profile. A super-Gaussian

evolution is defined by the following law [24]:

$$I(r) = I_0 \exp\left\{-2\left(\frac{r}{w_0}\right)^n\right\} \quad (1.18)$$

where  $n$  is the super-Gaussian order and must be an even non-negative integer greater than 2. Clearly, if  $n = 2$ , the result is just a Gaussian beam; on the contrary, the higher the order, the steeper the intensity profile edges and the flatter the intensity peak.

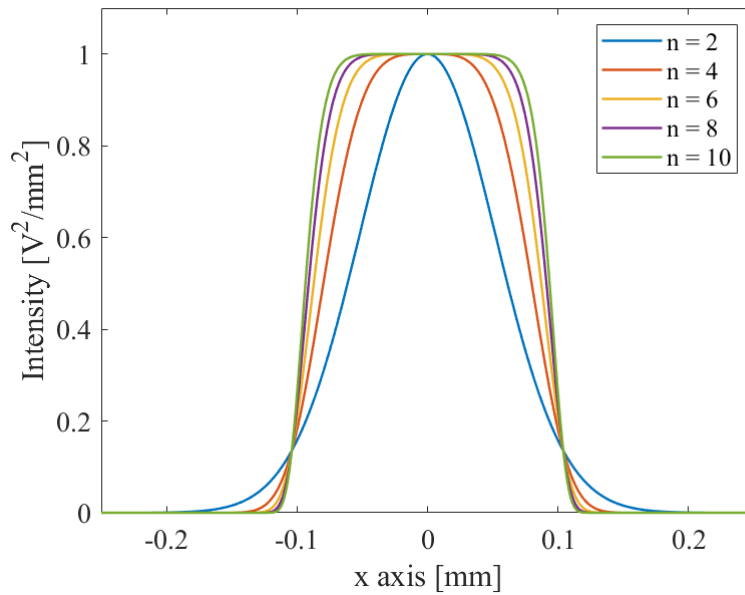


Figure 1.21: Intensity profile of super-Gaussian beams.

Fig. 1.21 points out that it is not required a very high super-Gaussian order to obtain a quite flat-top profile.

In contrast to Gaussian beams, a super-Gaussian is not a solution of the wave equation, hence it is not a mode of propagation. As a consequence, the field profile shape changes during the propagation, particularly when the beam order is quite high.

# Chapter 2

## Ray Tracing Technique

It is essential to point up that most of the present thesis work is developed according to the *paraxial approximation*, or rather in Gaussian optics the divergence angle along the slow axis and fast axis  $\theta$  must be smaller than  $20^\circ$ . Trigonometric functions are substituted by their first order approximations:  $\sin \theta \sim \theta$ ,  $\tan \theta \sim \theta$ ,  $\cos \theta \sim 1$ . All the formulas concerning the *Ray Tracing Technique* observe this approach. The method accuracy decreases when increasing the angles beyond the  $20^\circ$  bound.

The evolution of light through an optical system can be studied by resorting to the *Ray Tracing Technique*, which employs a set of rays specified by a certain origin and slope. Each point of the ray is described by a vector whose elements are the ray distance  $(x,y)$  from the propagation axis  $z$  and its slope  $\theta$ .

Rays are very handy when it comes to study the effect of an optical component, as a lens: the output ray is concisely computed as the matrix product between the vector containing the parameters of the incident ray and the *ABCD* matrix of the component.

The main disadvantage of such approach is that the ray is a path, thus it cannot be associated to an amplitude and a phase, contrarily to a field.

Assuming a bi-dimensional propagation in the  $(x,z)$  plane, the output  $\begin{bmatrix} x_1 \\ \theta_1 \end{bmatrix}$  right after a general element specified by the *ABCD* matrix is computed as a function of the ray parameters  $\begin{bmatrix} x_0 \\ \theta_0 \end{bmatrix}$  incoming on the element:

$$\begin{bmatrix} x_1 \\ \theta_1 \end{bmatrix} = \begin{bmatrix} A & B \\ C & D \end{bmatrix} \begin{bmatrix} x_0 \\ \theta_0 \end{bmatrix} \quad (2.1)$$

Intuitively, the matrix suitable to represent a system composed by multiple elements is computed by means of the multiplication shown in Eq. 2.2:

$$\begin{bmatrix} A & B \\ C & D \end{bmatrix} = \begin{bmatrix} A_n & B_n \\ C_n & D_n \end{bmatrix} \begin{bmatrix} A_{n-1} & B_{n-1} \\ C_{n-1} & D_{n-1} \end{bmatrix} \begin{bmatrix} A_1 & B_1 \\ C_1 & D_1 \end{bmatrix} \quad (2.2)$$

The element identified by the subscript  $n$  is the last of the system, whereas  $1$  symbolizes the first [20].

## 2.1. Mathematics of lenses

In geometrical optics the light interaction with a surface is described in terms of *light rays*, imaginary lines orthogonal to a series of wavefronts, showing the path where the light moves [26]. At each separation surface among two media characterized by different refractive indices, the rays undergo reflection and refraction phenomena. As for reflection, the angle described by the reflected ray and the surface normal is always equal to that defined by the incident ray and the same normal (*reflection law*), whereas the refraction is depicted according to Snell's law, describing the relationship between the incidence and refraction angles considering the refractive indices of their related media:

$$n_i \sin \theta_i = n_t \sin \theta_t \quad (2.3)$$

In contrast to mirrors (based just on the reflection law), lenses exploit the Snell's refraction law to manipulate beam propagation and to produce objects images. Lenses have typically round-shaped surfaces and are made up of a transparent refracting medium (glass or plastic in general) allowing the rays to be reflected at the front and rear surfaces (Fig. 2.1).

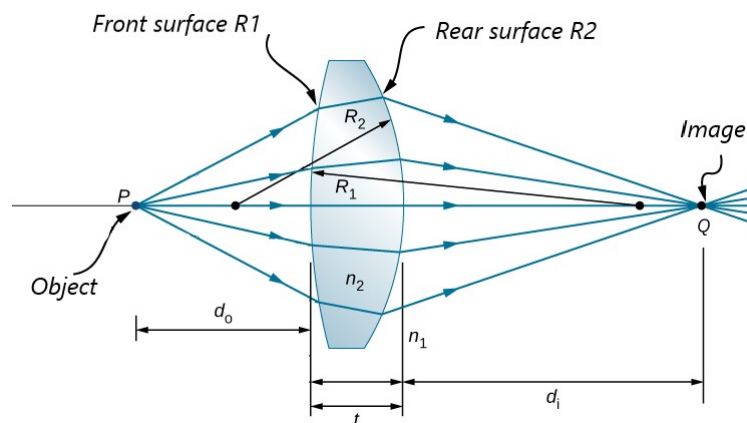


Figure 2.1: Rays diagram of a lens.

Firstly, lenses can be classified into two kinds: if the center thickness of the lens is much smaller than the surfaces radii of curvature, the lens should be treated as a *thin lens*; on the contrary, the lens has to be considered as a *thick lens*. An additional classification subdivides the lenses into converging and diverging lenses [26]: converging lenses (also called positive) are distinguished by a thicker shape in the middle with respect to the edges, whereas the diverging lenses (or negative lenses) are thinner in the central section. In this thesis just converging lenses are considered.

Lenses are marked out by two focal points that, in the thin lens case, are symmetric with respect to the lens location. As already mentioned, the paraxial approximation is involved, thus every ray orthogonal to the lens surface must converge exactly in one of the lens focal points. The radiation flow is slower in glass than in air; therefore, the middle part of the converging lens retards the light propagation the most, and,

as a consequence, the ray traveling through the lens center will cover the longest path both in terms of travelling time and distance.

An important design parameter of a lens is the numerical aperture (NA), which measures the portion of the incoming radiation that can be collected by the optical element; it is defined as a function of the refractive index  $n$  of the medium between the source and the lens, and of the half acceptance angle  $\alpha$ . An alternative formula can be used by employing the focal length  $f$  and the diameter  $D$  of the lens.

$$NA = n \sin \alpha = n \sin \left[ \arctan \left( \frac{D}{2f} \right) \right] \approx \frac{D}{2f} \quad (2.4)$$

**Lens maker equation** Ray diagrams are able to provide the image location, orientation and size starting from an object placed at the opposite side of the lens. The location and size of the image are determined by the awareness of at least three points: the object position, one focal point and the lens central position. Hence, only two rays are required to find in an approximate way the image (Fig. 2.2). Moreover, also the image type can be established: if the lens is positive, the formed image is real, otherwise in the case of a negative lens the image is virtual, since it is obtained by the extensions of the divergence rays.

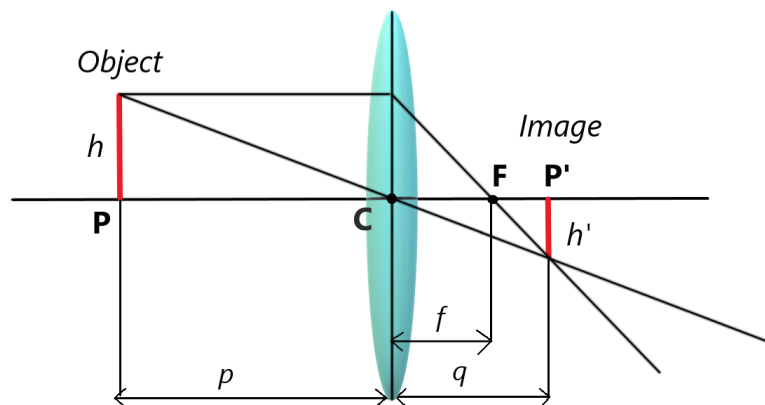


Figure 2.2: Refraction through a thin lens.

Before to proceed with the lenses equations, a convention must be adopted: if the Cartesian sign convention is employed, the positive direction is consistent with the light propagation and, as a result, the focal length is positive [27].

Lenses equations are different according to the lens kind and the simplest case refers to the thin lens. The thin lens equation (the lens maker equation) is the same of Gauss's equation for imaging and explains the relationship among the main lens parameters. The law is the following [16]:

$$\frac{1}{f} = \frac{1}{p} + \frac{1}{q} \quad (2.5)$$

where  $f$  is the focal length, while  $p$  and  $q$  are respectively the object and the image locations measured from the lens central axis, also called principal plane.

Generally, it is not enough to know just the position of the image, but also the size must be computed to obtain a full vision of the object transformation through the lens. Therefore, the magnification is introduced, providing information about the apparent enlargement of the initial object; concerning Fig. 2.2 the magnification is defined as the ratio between the image and object heights or as the inverse ratio among the image and object positions.

$$M = \frac{h'}{h} = -\frac{q}{p} \quad (2.6)$$

When a more precise analysis has to be computed and the lens center thickness  $d$  is no longer negligible with respect to the radii of curvature  $R_1$  and  $R_2$ , the thick lens equation must be exploited.

$$\frac{1}{f} = (n_l - 1) \left[ \frac{1}{R_1} - \frac{1}{R_2} + \frac{(n_l - 1)d}{n_l R_1 R_2} \right] \quad (2.7)$$

The magnification is the same as the previous case, but it is necessary to remark that a thick lens is described by two principal planes  $H_1$  and  $H_2$  (Fig. 2.3); hence, the image and object locations, measured properly from the principal planes, are clearly slightly different than the thin lens ones.

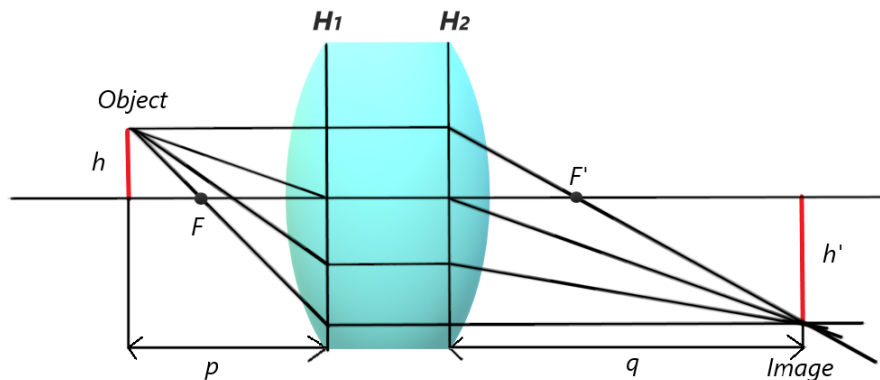


Figure 2.3: Refraction through a thick lens.

**Lenses ray transfer matrices** As already mentioned, a first lenses classification is based on their geometrical features.

The thickness of a thin lens can be neglected with respect to the radii of curvature of the surfaces, thus allowing important simplifications in the computations where thin lenses are involved. On the contrary, in the case of a thick lens it is not possible to implement any simplification because the distance between the lens surfaces is significant.

The ray transfer matrix of a thin lens (Eq. 2.8) depends only on the lens focal length  $f$  ( $f > 0$  for a convex lens).

$$\begin{bmatrix} A & B \\ C & D \end{bmatrix}_{thin\ lens} = \begin{bmatrix} 1 & 0 \\ -\frac{1}{f} & 0 \end{bmatrix} \quad (2.8)$$

The ray transfer matrix of a thick lens (Eq. 2.9) is obtained by following Eq. 2.2: the first matrix describes the second surface of the lens with radius of curvature  $R_2$ , the central matrix realises the propagation for a distance equal to the lens thickness  $t$ , and finally the third matrix corresponds to the first surface of the lens encountered, having a radius of curvature  $R_1$ . The refractive index inside the lens is  $n_2$ , outside of the lens it is  $n_1$ .

It has to be remarked that the curvatures can be either positive or negative: when describing a convexity oriented towards the source, the sign is conventionally positive.

$$\begin{bmatrix} A & B \\ C & D \end{bmatrix}_{thick\ lens} = \begin{bmatrix} 1 & 0 \\ \frac{n_2-n_1}{R_2 n_1} & \frac{n_2}{n_1} \end{bmatrix} \begin{bmatrix} 1 & t \\ 0 & 1 \end{bmatrix} \begin{bmatrix} 1 & 0 \\ \frac{n_1-n_2}{R_1 n_2} & \frac{n_1}{n_2} \end{bmatrix} \quad (2.9)$$

Despite Eq. 2.9 is certainly convenient to compute the output rays characteristics, it is not suitable for examining the rays trajectory inside the lens. To fulfill this analysis it is required to appreciate how rays incident at different heights with respect to the optical axis travel different paths from the source because of the lens curvature. The ray that covers the shortest distance to reach the lens, using as example a convex curvature, is the one propagating along the optical axis.

The rays progress inside a lens is then defined by evaluating the height of incidence on the lens and the distance covered from the source, in order to apply the renowned Snell's law and obtain the refraction angles.

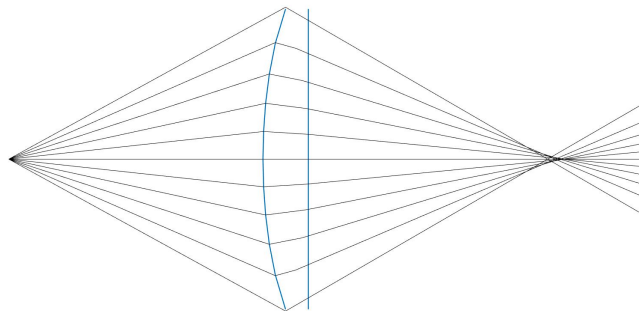


Figure 2.4: Rays trajectory through a thick lens.

The example in Fig. 2.4 does not fulfill the paraxial optics restrictions, and as a consequence aberrations appear. Indeed, when the rays that reach the lens surface farther from the vertex intersect the optical axis after the lens, they give rise to longitudinal spherical aberrations. According to this phenomenon, rays incident at different heights with respect to the optical axis are focused by the lens in different points along the propagation axis, and, referring to an incoming beam, the minimum

value of the spot size increases with respect to the ideal one computed by observing the paraxial approximation. [25]

When dealing with plano-convex lenses, a common good practice is to locate the lens so that its curvature is facing the collimated beam: the angles of incidence of the lens surface are then reduced and the aberrations are minimized with respect to the opposite possible orientation, as shown in Fig. 2.5.

Since the following analysis only realises the paraxial approximation, the aberrations are not included in the proposed simulations.

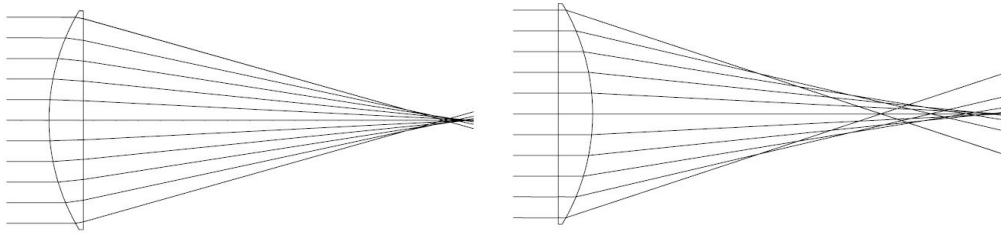


Figure 2.5: Correct (left) and wrong (right) orientations of a plano-convex aiming at minimizing the spherical aberrations.

The purpose of the next sections is to show the results of the MATLAB simulations of a Gaussian beam propagating through different optical systems, composed by specific lenses designed to obtain the beam focusing or collimation.

Specifically, the study follows two approaches, that eventually are proved to be congruent: the beam is represented by its Gaussian intensity distribution during the propagation and by an application of the *Ray Tracing Technique*, defined next. Since the two methods are equivalent, the reported results are valid for both the Gaussian beam and the Ray Tracing representations.

## 2.2. Five rays technique

A Gaussian beam that propagates in the limits of the paraxial approximation can be analysed by means of the Gaussian beam ray-equivalent model [5], exploiting five paraxial rays. This approach, and consequently also the simulation carried out by means of MATLAB, is not capable of modelling non-ideal behaviors in terms of aberrations, but is appropriate for the fitting of non-Gaussian beams with  $M^2 > 1$ . The five rays and their physical meaning for a laser beam source representation are presented below and depicted in Fig. 2.6.

- *Chief ray*: it is the symmetry axis of the beam, positioned at the center of the source; in case of an on-axis propagation through a lens, it coincides with the optical axis and its direction is not deflected.
- *Waist rays*: the two waist rays propagate straight along the  $z$  axis, defining the beam waist size.

- *Divergence rays*: the two divergence rays propagation is directed according the divergence angle  $\theta$  and their origin is the same as the chief ray.

As already mentioned, when a ray encounters the surface of a lens its angle is modified according to the  $ABCD$  matrix defining the lens. Different cases of Gaussian beam and ray propagation through a lens are illustrated in the next section.

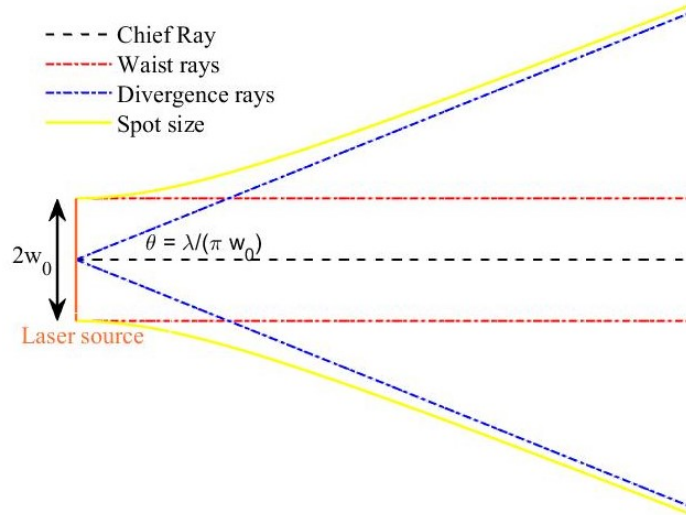


Figure 2.6: Example of the five rays trajectories for the Gaussian beam ray-equivalent model of a laser source.

## 2.3. Beam focalisation

This section examines the intensity profile of a Gaussian beam propagating through one or more focusing lenses and the related five rays equivalent model.

If a lens receives as input a collimated beam, ideally characterized by a plane wavefront and by a rather null divergence, it focuses the beam at a distance from the lens equal to its focal length. The divergence of a focused beam can be quite large, since the spot size reaches a very small value with respect to the input one.

A Gaussian beam can be considered collimated up to a distance from the source equal to the Rayleigh range  $z_R$ : as a consequence, the position of the lens in relation to  $z_R$  is very relevant. Nevertheless, in a paraxial analysis the divergence of the beam is usually not so large even for distances above the Rayleigh range; therefore, the beam can be focused still quite correctly also if the lens is farther than  $z_R$ .

An analysis of the different effects produced by the same lens when varying the source-lens distance is presented in the thick focusing lens analysis, proposed in Section 2.3.2.

The Gaussian beam source under test is described in Tab. 2.1. It is essential to highlight that all the input and output divergence angle and beam waist parameters related to the simulations from now on are considered with respect to the beam symmetry axis: the beam waist is half of the laser diode emission facet and the divergence angle is half of the total beam divergence.

Table 2.1: Source parameters.

Wavelength	Beam waist	Divergence angle	Rayleigh range
900 nm	150 $\mu\text{m}$	1.90 mrad	78.54 mm

### 2.3.1. Thin focusing lens

The lens employed in the simulation is characterized by a focal length  $f = 15$  mm. Fig. 2.7 demonstrates that the beam focusing is successful for the chosen collimated beam and lens position. Indeed, the original beam waist is reduced by a factor of about 5.25, as can be noted by comparing the input and output beam parameters (Tab. 2.1 and Tab. 2.2). Moreover, by observing the reported simulations, it is clear that the two employed models are perfectly equivalent in terms of evolution of the beam, as it is expected to be in a paraxial analysis. However, it has to be remarked that it is not possible to trace out the beam intensity profile when implementing the five rays model, then only the spot sizes are compared.

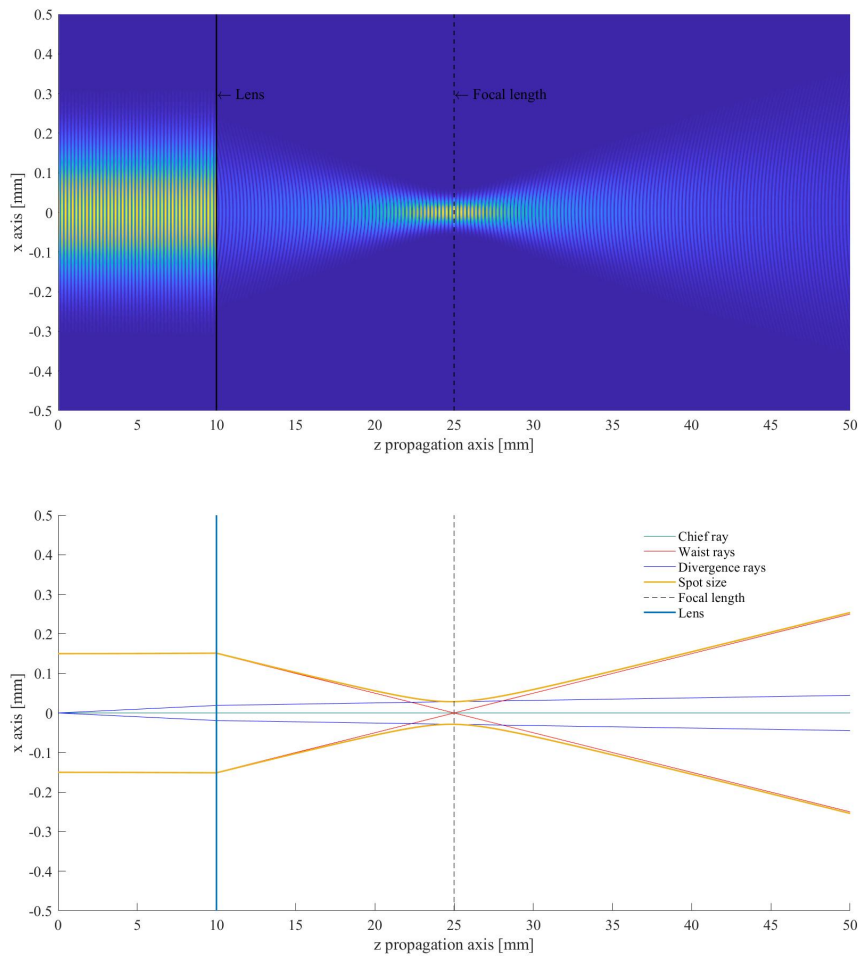


Figure 2.7: Gaussian beam and five rays equivalent model propagating through a thin lens ( $f = 15$  mm) placed at 10 mm from the source.

Table 2.2: Fig. 2.7 output parameters.

Wavelength	Beam waist	Divergence angle	Rayleigh range
900 nm	28.59 $\mu\text{m}$	10.02 mrad	2.85 mm

Once ensured the results congruence provided by the two different representations of the optical system, the derivation of a more complex configuration is straightforward. For instance, a second lens with focal length  $f_2 = 25$  mm is added to the previous system. If the distance between the first lens focal point and the second lens is equal to  $f_2$ , the final beam undergoes a collimation process, as illustrated in Fig. 2.8. The output beam is characterized by the parameters reported in Tab. 2.3. The condition that allows the collimation to take place is detailed in Section 2.4.

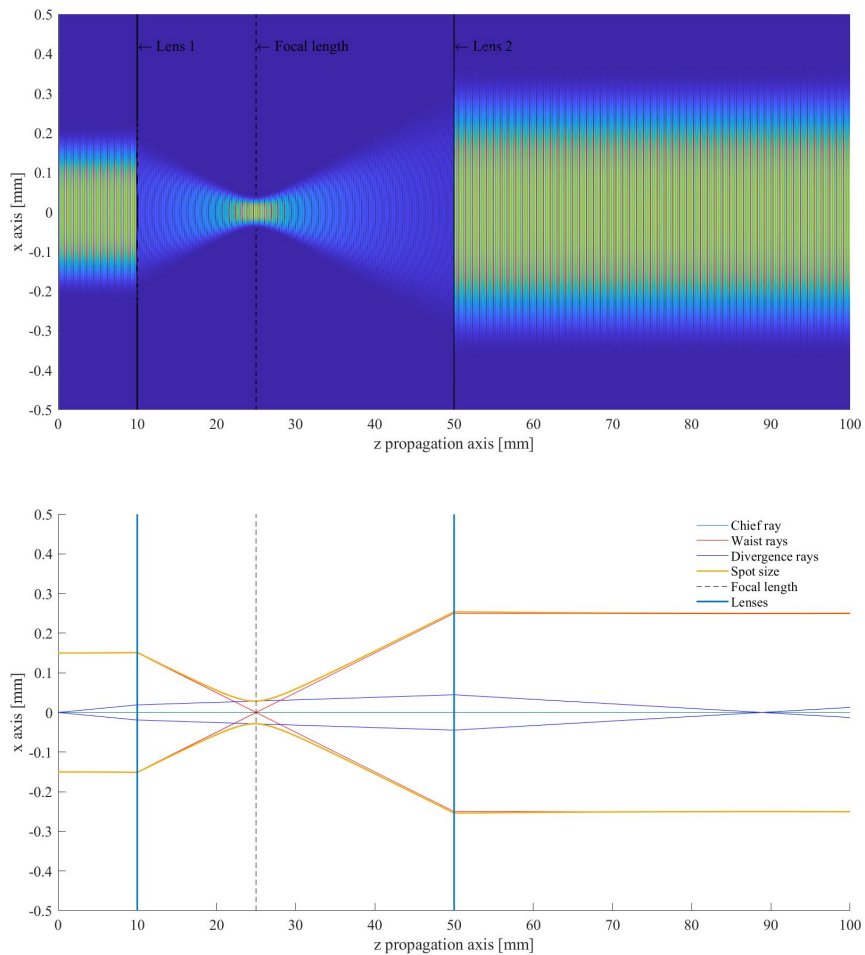


Figure 2.8: Gaussian beam and five rays equivalent model propagating through two thin lenses placed at 10 mm ( $f_1 = 15$  mm) and 50 mm ( $f_2 = 25$  mm) from the source.

Table 2.3: Fig. 2.8 output parameters.

Wavelength	Beam waist	Divergence angle	Rayleigh range
900 nm	250 $\mu\text{m}$	1.14 mrad	219 mm

### 2.3.2. Thick focusing lens

The lens type that has been used in the following simulations is a plano-convex lens, or rather it is a converging lens, since the lens is thicker in the middle (Fig. 2.9). All the rays passing through the lens are deflected towards the focal point and, as a result, the plane wavefronts are converted into spherical ones or vice-versa [26].

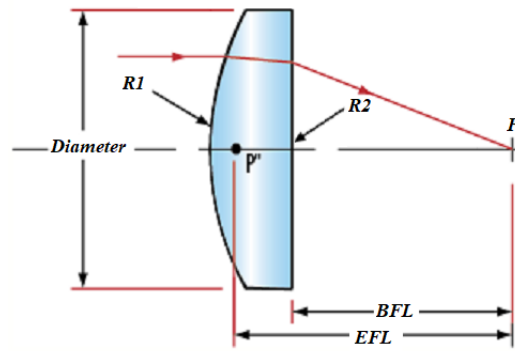


Figure 2.9: Plano-convex thick lens.

Tab. 2.4 describes the lens implemented in the simulation, considering the convexity oriented towards the collimated source. In the software, in order to simulate the planar facet of the lens, it is enough to set a value which is orders of magnitude higher than the other radius of curvature.

Table 2.4: Thick lens parameters.

Refractive index	Center thickness	Radii of curvature	EFL
1.515	5 mm	7.7 mm, $-1000$ mm	14.86 mm

By referring to Fig. 2.9, the term *EFL* attributes to the Effective Focal Length, which is the distance between the rear focal point *F* and the rear principal plane *P'* [28]; it can be computed by means of the following equation for a lens with a given geometry and refractive index *n*.

$$\frac{1}{EFL} = (n - 1) \left( \frac{1}{R_1} - \frac{1}{R_2} + \frac{(n - 1)t}{nR_1R_2} \right) \quad (2.10)$$

Instead, the Back Focal Length (*BFL*), in the case under analysis equal to 11.6 mm, is the distance between the rear focal point *F* and the rear vertex of the lens, that, in the case of a plano-convex lens, is just the planar facet *R*<sub>2</sub>.

The focalisation of the source beam described in Tab. 2.1 operated by the implemented thick lens (Tab. 2.4) is detailed in Fig. 2.10 and in Tab. 2.5.

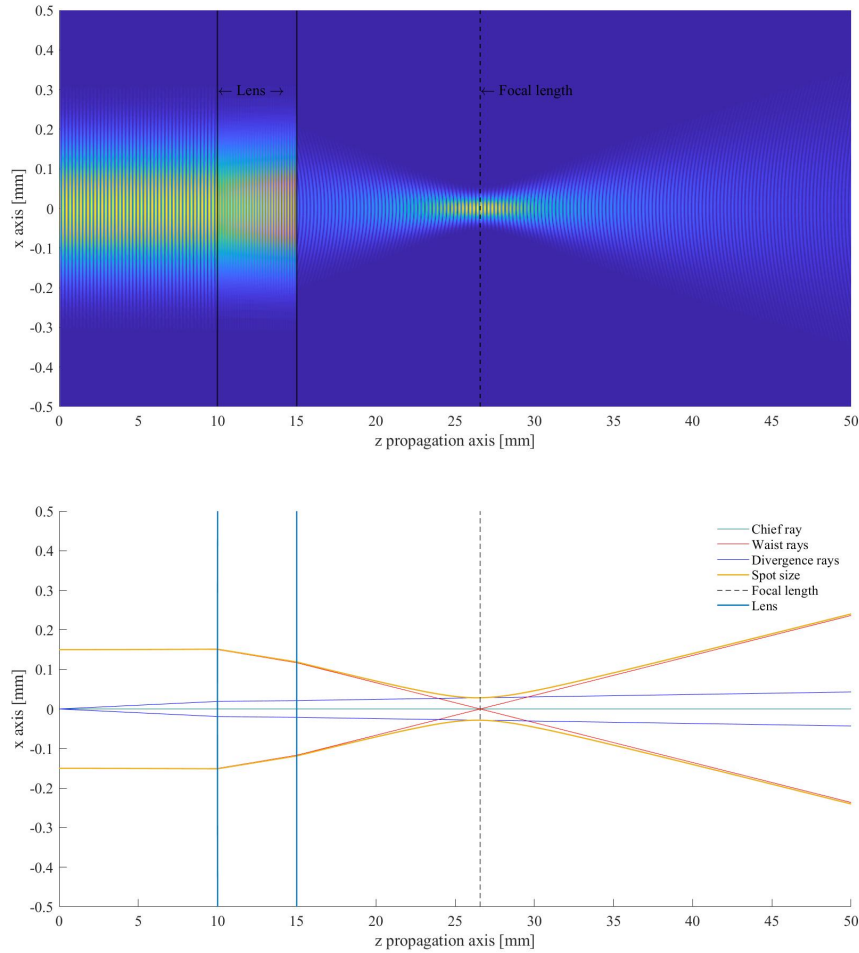


Figure 2.10: Gaussian beam and five rays equivalent model propagating through a thick lens placed at 10 mm from the source.

Table 2.5: Fig. 2.10 output parameters.

Wavelength	Beam waist	Divergence angle	Rayleigh range
900 nm	27.06 $\mu\text{m}$	10.58 mrad	2.55 mm

As previously mentioned, in contrast to the thin lens, rays propagate also inside the thick lens by means of refraction phenomenon, clearly explained by the Snell's law. Obviously, it is not possible to appreciate the lens geometry in Fig. 2.10, because the incident rays are not far from the optical axis. Indeed, being the curvature around the center of the lens insignificant, the rays angles are not greatly modified when crossing the interface air-lens; especially the divergence rays, which are the closest to the optical axis, have the lowest direction variation.

As already quoted, the beam focusing is ideal when the lens is closer to the source than  $z_R$ . Fig. 2.11 example demonstrates that, despite the lens position is larger than twice the Rayleigh range, the focusing takes place around the focal length; it is possible to measure that the minimum value of the spot size is obtained at about 1 mm from the theoretical focal point. With respect to the previously analysed configuration, the output beam is characterized by a larger divergence, which increases further when distancing more the lens and the source, because the beam incident on the lens is not collimated anymore. To avoid redundancy, only the five rays model is presented in Fig. 2.11 and in Tab. 2.6.

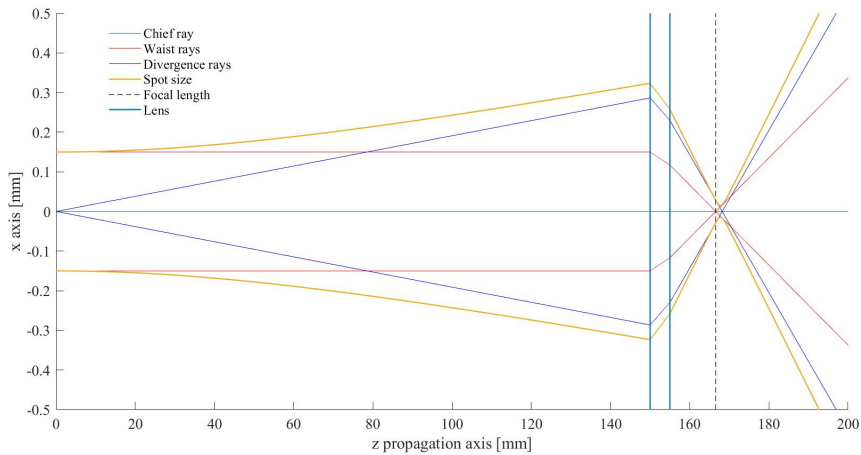


Figure 2.11: Five rays equivalent model of a Gaussian beam propagating through a thick lens placed at 150 mm from the source.

Table 2.6: Fig. 2.11 output parameters.

Wavelength	Beam waist	Divergence angle	Rayleigh range
900 nm	14.29 $\mu\text{m}$	20.08 mrad	0.71 mm

## 2.4. Beam collimation

A lens is regarded as collimating when the divergent incoming beam is transformed into a beam with negligible divergence. Particularly, the source must be placed at a distance from the lens equal to the focal length, because, by definition, the rays that pass through the lens focal length undergo the collimation process.

The Gaussian beam under test during the whole *Beam collimation* section is generated by a narrower source with respect to the one previously implemented, as can be observed by comparing Tab. 2.1 and Tab. 2.7.

Table 2.7: Source parameters.

Wavelength	Beam waist	Divergence angle	Rayleigh range
900 nm	10 $\mu\text{m}$	28.64 mrad	0.35 mm

### 2.4.1. Thin collimating lens

The lens used in the MATLAB simulation whose outputs are illustrated in Fig. 2.12 has a focal length  $f = 10$  mm. Indeed, the lens is placed at a distance  $d = 10$  mm from the source. The collimation takes place successfully because the spot size, in the analysed propagation range after the lens (shorter than the output beam Rayleigh range), is constant, or rather the beam divergence is essentially negligible, as illustrated in Tab. 2.8.

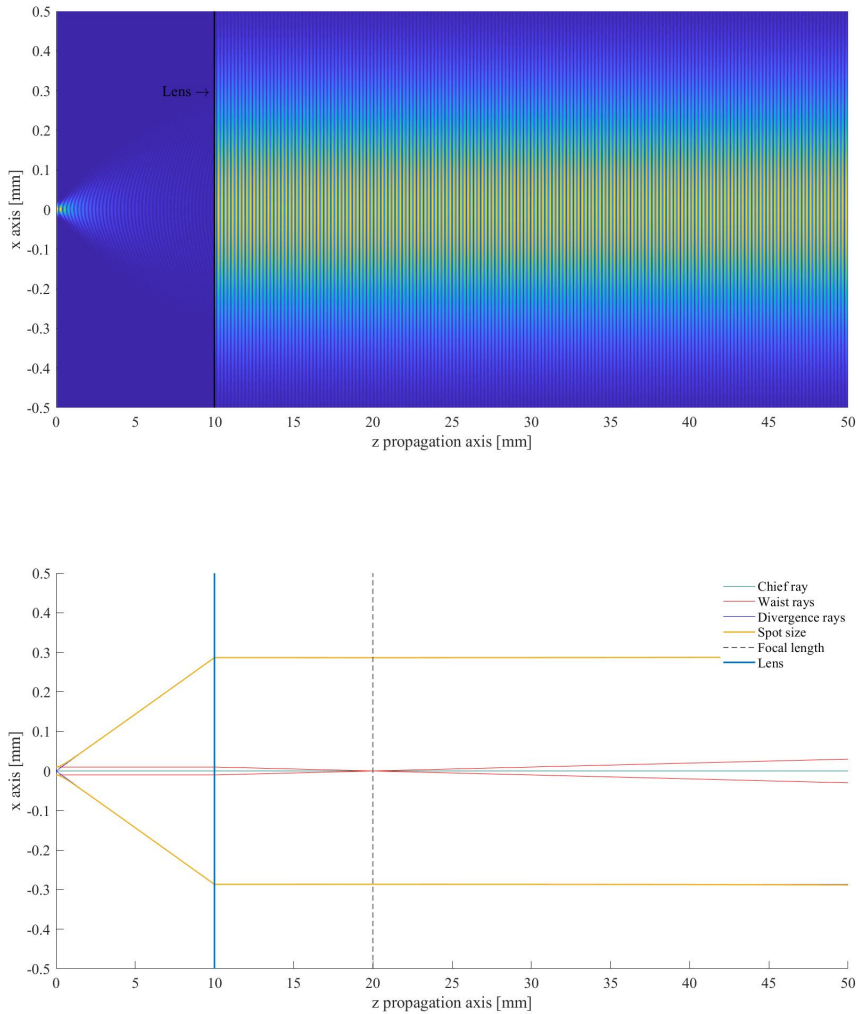


Figure 2.12: Gaussian beam and five rays equivalent model propagating through a thin lens ( $f = 10$  mm) placed at 10 mm from the source.

Table 2.8: Fig. 2.12 output parameters.

Wavelength	Beam waist	Divergence angle	Rayleigh range
900 nm	286 $\mu$ m	1 mrad	286.47 mm

### 2.4.2. Thick collimating lens

The same thick lens previously used is implemented in Fig. 2.13, whose outputs are detailed in Tab. 2.13. It has to be remarked that the plano-convex lens is conventionally oriented to have the planar surface facing the lens focus, so the parameters describing the radii of curvature must be modified as shown in Tab. 2.9:

Table 2.9: Thick lens parameters.

Refractive index	Center thickness	Radii of curvature	EFL
1.515	5 mm	1000 mm, $-7.7$ mm	14.86 mm

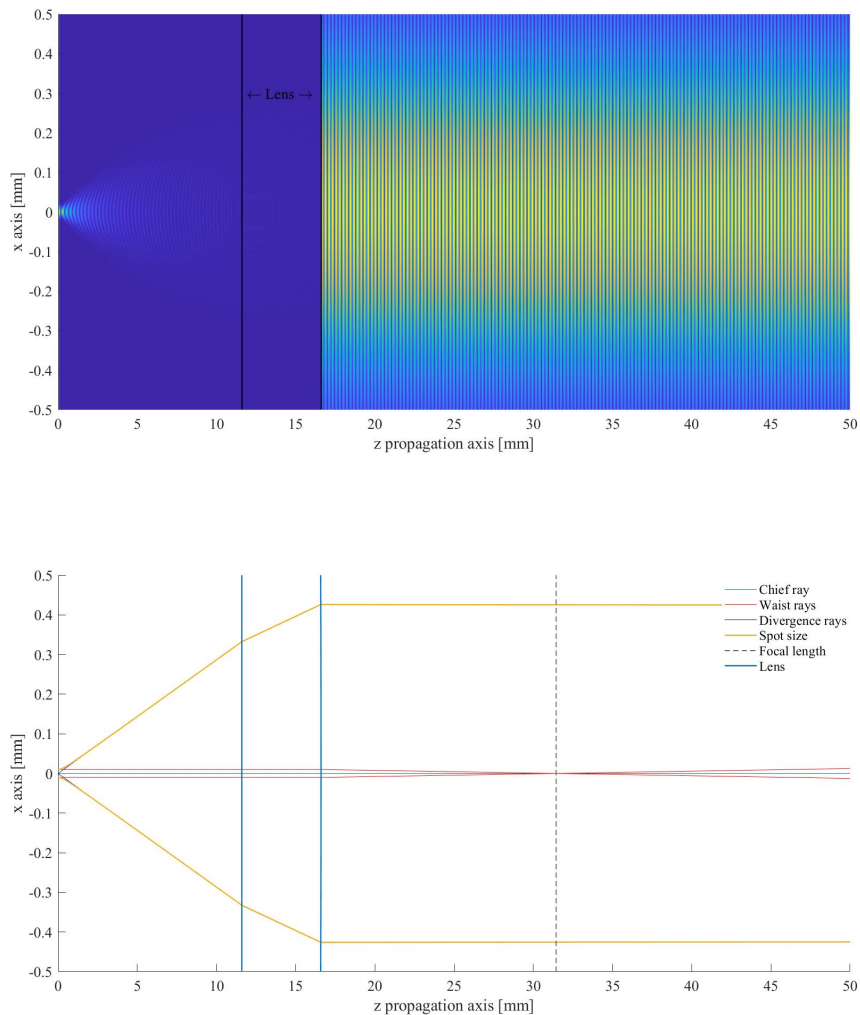


Figure 2.13: Gaussian beam and five rays equivalent model propagating through a thick lens placed at 11.6 mm from the source.

Table 2.10: Fig. 2.13 output parameters.

Wavelength	Beam waist	Divergence angle	Rayleigh range
900 nm	428 $\mu\text{m}$	0.67 mrad	0.35 mm

## 2.5. Off-axis propagation

When the light source is not located on the optical axis of the lens, the beam propagation is called off-axis.

Conversely to the on-axis propagation, in the off-axis case also the chief ray undergoes direction variations, particularly its angle changes since it must cross the focal point on the lens optical axis. Naturally, the waist and divergence rays follow the direction of the chief ray.

The off-axis configuration can be represented only by means of the five rays beam equivalent model, because the Gaussian beam optical axis remains unvaried along the propagation through the lenses present in the optical system.

Fig. 2.14 and Fig. 2.15 respectively illustrate the case of an off-axis focalisation and of an off-axis collimation; the results of both the simulations are reported in Tab. 2.11.

The thick lens parameters are the same of the previous simulations (Tab. 2.4 and Tab. 2.9); in the case of focusing lens the source parameters are reported in Tab. 2.1, whereas in the collimating case the source parameters are the same of Tab. 2.7.

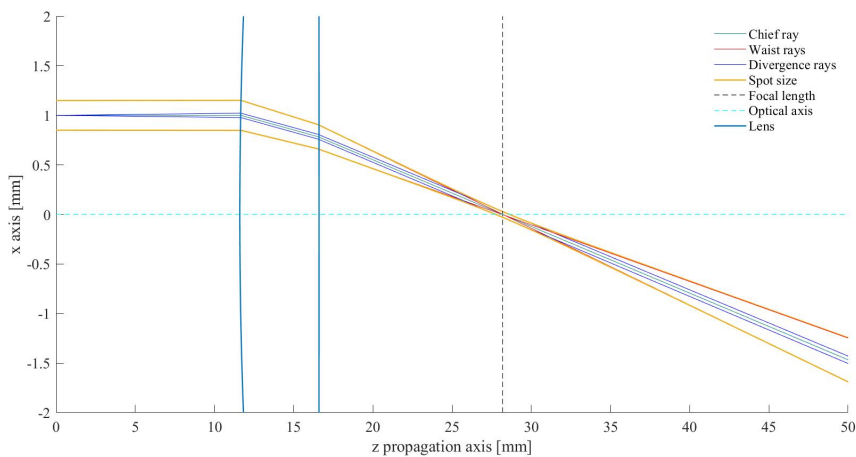


Figure 2.14: Five rays equivalent model of an off-axis Gaussian beam focusing through a thick lens placed at 11.6 mm from the source.

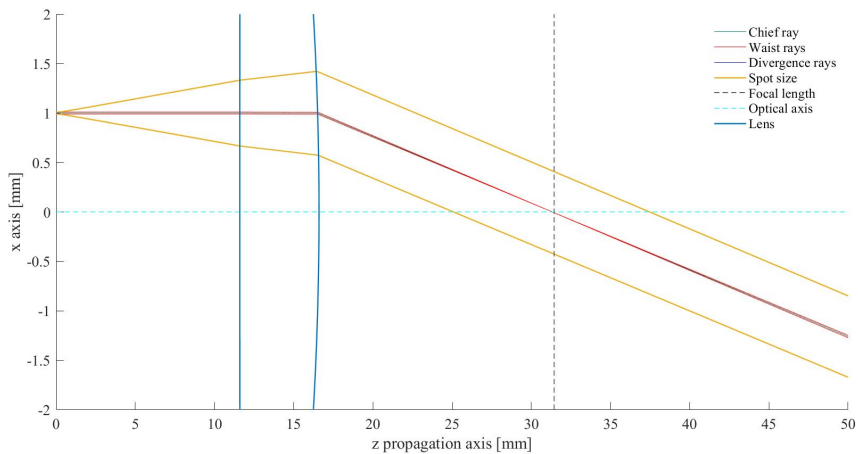


Figure 2.15: Five rays equivalent model of an off-axis Gaussian beam collimating through a thick lens placed at 11.6 mm from the source.

Table 2.11: Thick lens output parameters in off-axis propagation.

	Offset	Beam waist	Divergence angle	Rayleigh range
Focusing case	1 mm	28.7 $\mu\text{m}$	10.1 mrad	2.87 mm
Collimating case	1 mm	395 $\mu\text{m}$	0.233 mrad	543 mm

Setting the same input parameters, the commercial software TracePro produces very similar output beam waist values, thus confirming the correctness of the MATLAB developed code: 29.8  $\mu\text{m}$  413  $\mu\text{m}$  are the minimum of the spot sizes illustrated respectively in Fig. 2.16 and Fig. 2.17.

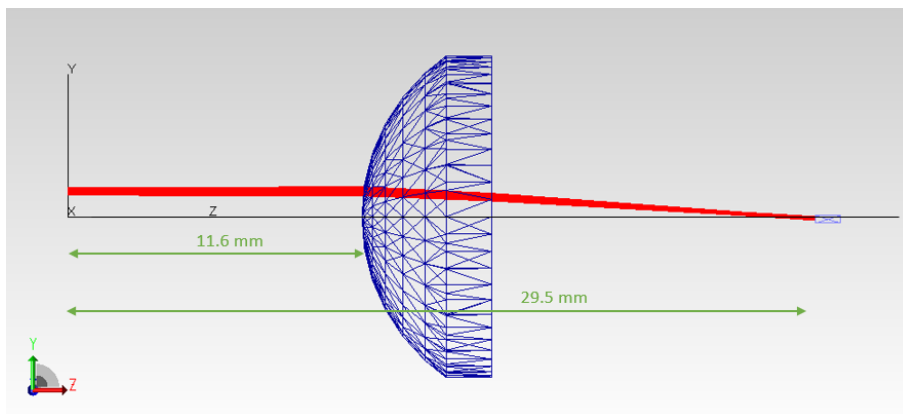


Figure 2.16: Off-axis beam focusing through a thick lens placed at 11.6 mm from the source provided by TracePro.

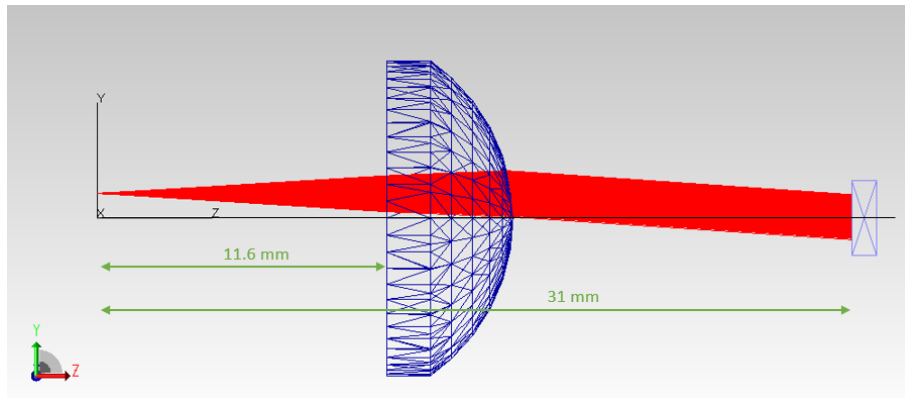


Figure 2.17: Off-axis beam collimation through a thick lens placed at 11.6 mm from the source provided by TracePro.

# Chapter 3

## Laser Beam Tool Validation

This section is intended to demonstrate the accuracy of the developed MATLAB programs. The purpose has been fulfilled by realizing a comparison between the simulations output and the physical measurements carried out in laboratory.

Lasers depicted by very different characteristics in terms of  $M^2$  have been analysed during the laboratory experiences: a quasi-Gaussian beam laser (He-Ne) and an astigmatic beam laser (green pointer). As a matter of fact, one of the main goals is to evaluate the beam quality, quantified by the  $M^2$  factor, and the beam parameter product (BPP), which theoretically should be constant during the beam propagation in an optical system. It is needed to remind that lower values of BPP and  $M^2$  mean higher beam quality.

Commercial beam profilers (for example based on CMOS or CCD cameras) are able to obtain the beam quality and the beam size measurements in a few seconds [29]; indeed, the experimental measurements, focused mainly on the estimation of the spot size of the beam, were obtained thanks to the high resolution CMOS camera *DCC3260C* by Thorlabs. The main sensor characteristics are shown in Tab. 3.1. The camera was mounted on a sliding rail, so that, by moving it along the propagation direction, it was possible to visualize the spot size at different distances from the source and then characterize its evolution.

The spot size is the quantity of major interest because it allows computing the other parameters fundamental to fully define a Gaussian beam, especially the beam waist and the half-divergence angle in the far field.

Table 3.1: Thorlabs DCC3260C sensor characteristics.

Imaging Area (Horizontal x Vertical)	11.340 mm x 7.130 mm
Number of Pixels (Horizontal x Vertical)	1936 x 1216
Pixel Size	5.86 $\mu\text{m}$

**Spot size computation** Before proceeding with the analysis of the devices utilized in laboratory, it is preliminary to explain how the images acquired by the camera were processed in order to obtain the spot size measurements.

The laser emission intensity in each point along the direction of propagation can be

approximated with a Gaussian, whose standard deviation is the beam spot size. Starting from this assumption, after the acquisition, the images were uploaded in MATLAB in order to find the Gaussian intensity function of the data contained in the color code of each picture. The standard deviation of the Gaussian that fits best the data corresponds then to the spot size in the analyzed propagation coordinate. An example of the result of such procedure is depicted in Fig. 3.1, related to the camera positioned at 100 mm from the He-Ne laser output.

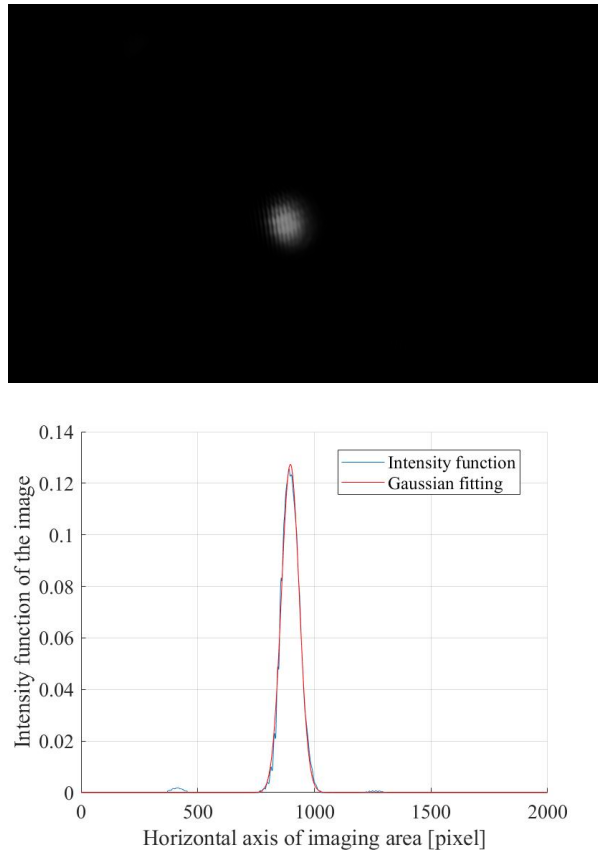


Figure 3.1: Gaussian fitting of the intensity function extrapolated from the image related to the He-Ne beam at  $z = 100$  mm from the laser output.

### 3.1. He-Ne Laser

The first device under test is a Helium-Neon red laser: in fact, it is very easy to handle thanks to the emission in the visible spectrum and the low power, usually around few milliwatts. Another advantage of the He-Ne laser is that the output light intensity, as well as the wavelength of emission, is really stable [30].

The He-Ne laser belongs to the gas lasers family, meaning that the active medium for laser amplification is at gaseous or plasma state. The gases that constitute the gain medium of the analysed laser are helium and neon, and are contained in a glass tube of a typical length of few tens of centimeters. Both the species are inert, so they do not bond forming a new stable molecule [30].

He-Ne lasers are characterized by a quality factor  $M^2$  very close to 1, so they represent a good approximation of the ideal case of a perfectly Gaussian emission. The employed device is the red laser *Uniphase 1105/P Helium-Neon*, described in terms of its primary parameters in Tab. 3.2.

The experimental characterization was carried out in three different configurations: using no lenses, then using a spherical lens, and finally using a cylindrical lens.

Table 3.2: Uniphase 1105/P specifications.

Wavelength	Beam diameter	Output power
632.8 nm	810 $\mu\text{m}$	10 mW

It has to be remarked that while analysing the He-Ne laser, the camera was used along with two neutral density filters, *NDUV10A* and *NDUV20A* by Thorlabs, to avoid the saturation of the acquired image that would have led to a wrong analysis of the data extracted from the images. An additional useful way to prevent the saturation is to work with low exposure time; the minimum available was equal to 0.034 ms.

### 3.1.1. Source characterization

The first experiment was intended to characterize the main parameters of the laser source, especially in terms of beam waist and divergence angle.

The beam was discovered to have a small astigmatism, in fact the spot sizes along the vertical and horizontal axes differ of about 0.03 mm along all the range of distances analysed, as shown in Fig. 3.2.

Due to the proved negligible difference between the two axes, successively in the document only the results related to the beam horizontal axis ( $x$ -axis) will be reported.

Fig. 3.3 presents the comparison between the measured spot size related to the  $x$ -axis and the results produced by the simulation. The latter was carried out by setting as beam waist necessary to analytically compute the spot size the minimum of the curve that fits the experimental data. As can be noted by He-Ne laser parameters described in Tab. 3.2, the beam waist found in laboratory is different from the one declared by the datasheet. According to the vendor data, the beam waist found should be around 400  $\mu\text{m}$ ; the measured value is instead 313.7  $\mu\text{m}$ .

This discrepancy has been addressed to the fact that the measurements, besides suffering from human error, have been taken without knowing the exact location of the source inside the laser structure. The value provided by the datasheet is then ignored and substituted with the measured one.

The other fundamental parameter necessary to describe a real-world beam is the divergence angle, whose value computed as the inverse tangent of the spot size in the far field was fed to the simulation. In order to provide a reasonable value, the computation of the divergence angle must rely on spot size measurements as far as possible from the Rayleigh range.

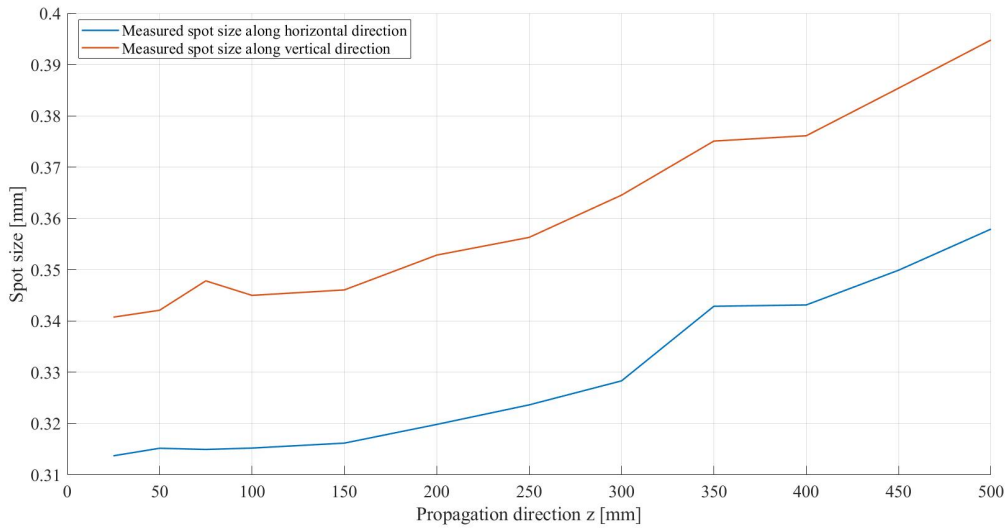


Figure 3.2: Astigmatism of He-Ne laser source.

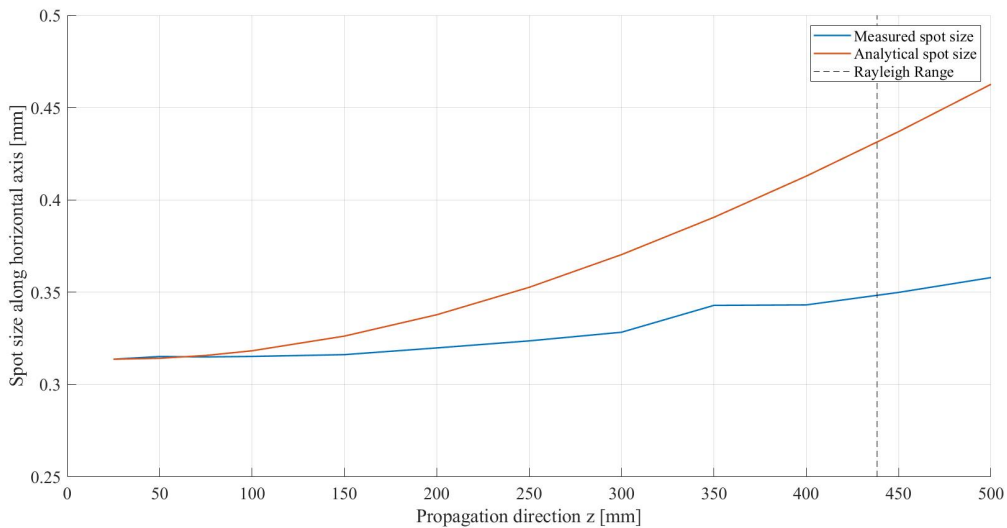


Figure 3.3: Comparison between measured and simulated spot sizes of the He-Ne laser.

It is evident that a quite significant variance between the two sets of spot size values for distances larger than 100 mm occurs. Nevertheless, the results can be considered undoubtedly coherent, since for the first points along the propagation direction they are perfectly comparable.

About the following points, the reason of the lower measured values with respect to the ideal ones can be addressed to the sensitivity of the camera, considering also the additional filters, implemented with the purpose of lowering the intensity of the input of the camera sensor to avoid image saturation. The side-effect of the filters behavior is that they lower the intensity of the tails of the Gaussian function below

the sensitivity of the camera. As a consequence, the tails, which constitute a non-negligible portion of the whole Gaussian intensity, are not sensed by the camera, and the overall represented intensity is lower than the expected one. Eventually, also the BPP parameter conservation through the lens is affected, since the field actual spot size cannot be detected in a proper way by the camera.

Despite the notable error due to the camera dynamic, the measured spot size and divergence angle were used to compute the factor  $M^2$  factor and the BPP of the laser source, resulting in reasonable values.

All the main parameters describing the He-Ne source, experimentally measured, are reported in Tab. 3.3; according to the  $M^2$  factor and the BPP, the beam quality should be considered very high.

Table 3.3: He-Ne source measured parameters.

Beam waist	Divergence angle	$M^2$	BPP
313.7 $\mu\text{m}$	0.71 mrad	1.11	$2.23 \times 10^{-7}$

### 3.1.2. Spherical lens setup

Once confirmed that the developed MATLAB codes are able to emulate the source beam evolution (excluding the error introduced by the camera sensitivity), the following purpose was to verify the effect of a lens on the laser emission. The realised setup is depicted in Fig. 3.4.

The spherical lens used in the proposed setup is the Thorlabs *AC254-200-A-ML* lens characterized by a focal length of 200 mm.

Since the output of the He-Ne laser is quite collimated, ideally the position of the lens should not affect the result of the experiment. The distance between the source and the lens was set to about 100 mm.

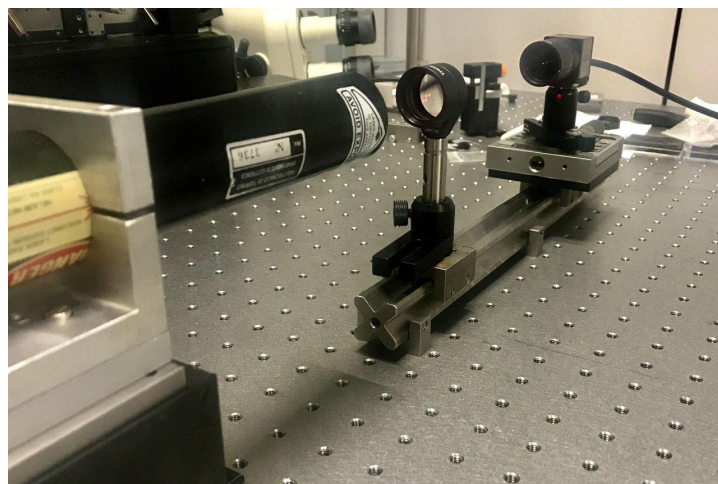


Figure 3.4: Setup mounted to evaluate the effect of a focusing spherical lens on the He-Ne beam.

The camera was initially located in the presumed focal point, and was subjected to translations of about 1 mm around it in order to empirically find the minimum value of the spot; then, it was moved beyond the Rayleigh range to characterize the beam in far field region. The spot size evolution was studied by following the procedure detailed in the paragraph **Spot size computation**.

The experiment configuration was successively simulated by means of the five rays equivalent model representing the source previously characterized, including also the effect of a thin lens with the same focal length as the the *AC254-200-A-ML* lens. The simulated beam propagation after the lens should be comparable with the experimental measurements; Fig. 3.5 shows clearly how the two sets of results are compatible, so the experience was claimed successful.

Moreover, as shown in Tab. 3.4, the BPP after lens is quite constant with respect to the one computed in the previous setup.

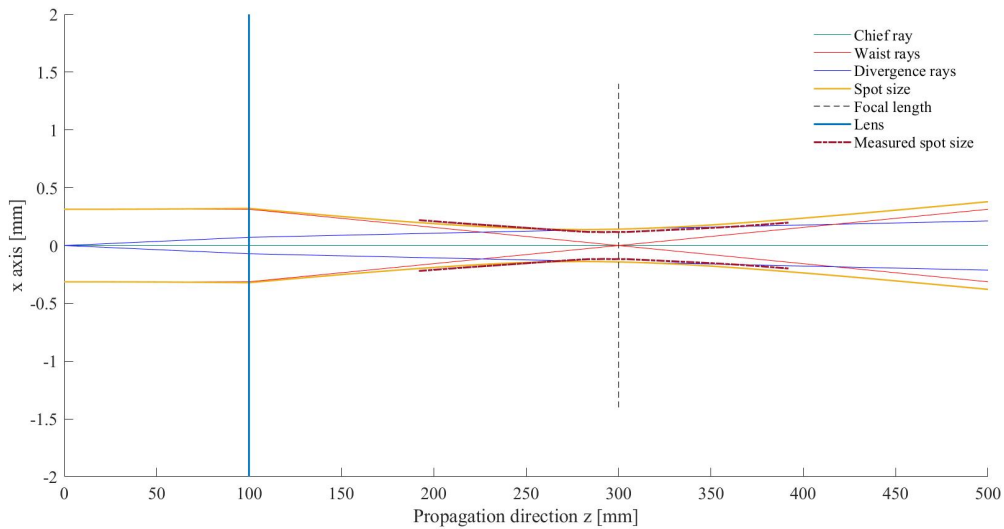


Figure 3.5: Comparison between measured and simulated spot sizes of the He-Ne laser through a thin spherical lens.

Table 3.4: He-Ne through a spherical lens - experimental and analytical comparison.

	Beam waist	Divergence angle	BPP
Experimental	116 $\mu\text{m}$	2.2 mrad	$2.55 \times 10^{-7}$
Analytical	138 $\mu\text{m}$	1.45 mrad	$2 \times 10^{-7}$

### 3.1.3. Cylindrical lens setup

The cylindrical lenses, according to their curvature, operate only on one axis of the incoming beam, so they are largely employed to generate a laser line.

The Edmund Optics plano-convex lens employed in the presented configuration has a focal length equal to 100 mm.

Due to the orientation used in the setup (Fig. 3.6), it modifies only the horizontal

axis of the beam, thus causing its focusing at about 100 mm from the lens. Once again, the measured values regarding the laser source were exploited to simulate the beam propagation through the lens by means of the five rays approach. The cylindrical lens has been described as a thick lens, referring to its physical parameters: the radius of curvature is 51.85 mm and the center thickness is 7.7 mm. The result of the comparison, depicted in Fig. 3.7, can be considered appropriately congruent: the MATLAB program is suitable also to simulate the beam transformation operated by cylindrical lenses. The comparisons between experimental and analytical measurements is reported in Tab. 3.5.

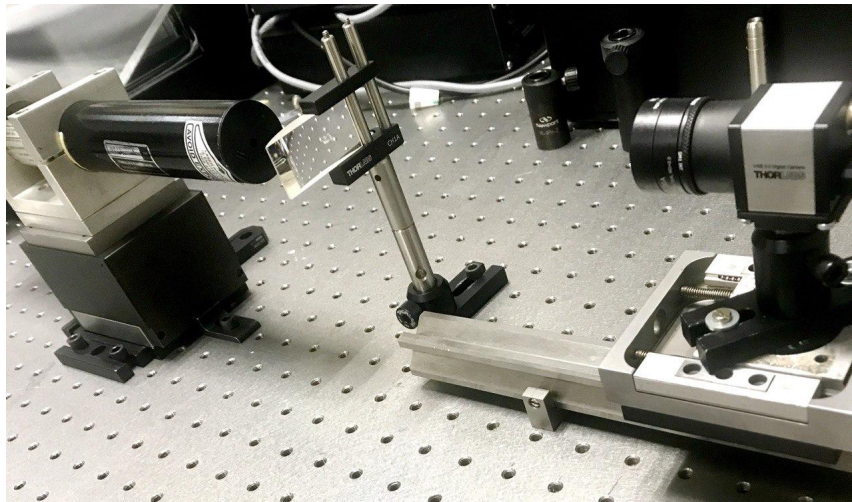


Figure 3.6: Setup mounted to evaluate the effect of a focusing cylindrical lens on the He-Ne beam.

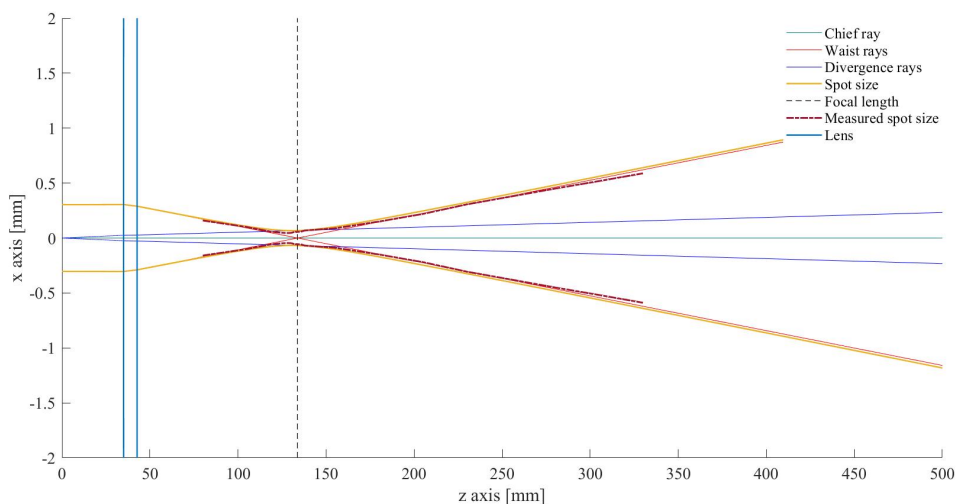


Figure 3.7: Comparison between measured and simulated spot sizes of the He-Ne laser through a thick cylindrical lens.

Table 3.5: He-Ne through a cylindrical lens - experimental and analytical comparison.

	Beam waist	Divergence angle	BPP
Experimental	45.8 $\mu\text{m}$	2.9 mrad	$1.33 \times 10^{-7}$
Analytical	67.4 $\mu\text{m}$	3.16 mrad	$2.13 \times 10^{-7}$

## 3.2. Green Laser Pointer

The green laser pointer is a tiny device, belonging to the frequency-doubled solid-state lasers category, that emits in the visible range, precisely between 510 and 570 nm. It is more complex and more expensive than the red counterpart, since the laser diodes in the green emission range are no longer available [31]. The emitted beam of the green pointer appears to much brighter than the red laser pointers.

By virtue of its reduced dimensions, the low emitted power of few milliwatts and the use of a battery as power source, the green laser pointer is very manageable.

The primary drawbacks of the available green laser pointer are the huge  $M^2$  factors along the two directions, leading to a radiated field which is far from the ideal Gaussian distribution. It is then expected that the beam quality of the green laser beam is lower than the He-Ne one.

The acquired image of the green source is illustrated in Fig. 3.8.

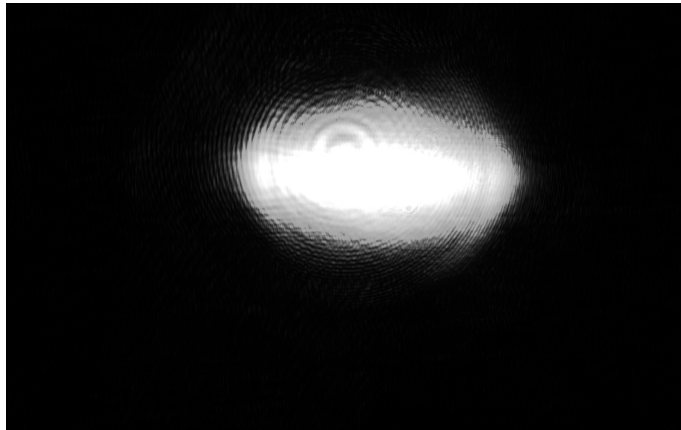


Figure 3.8: CMOS camera image of a green laser pointer beam.

The experimental measurements have been computed by means of the Thorlabs green laser pointer *CPS520*. The pointer produces a coherent, astigmatic and collimated beam, depicted by the parameters contained in Tab. 3.6.

Table 3.6: CPS520 specifications.

Wavelength	Beam shape	Output power
520 nm	4.6 mm $\times$ 1.7 mm	4.5 mW

As well as in the He-Ne laser case, the spot size of the radiated beam was obtained from the Gaussian curve that best fitted the data.

Due to large and different  $M^2$  factors, the pointer radiation does not follow a Gaussian distribution. Indeed, as illustrated in Fig. 3.9, besides the different widths of the intensity functions along the horizontal and vertical direction (consequence of the astigmatism), it is evident that the Gaussian fitting is more critical for the beam in the horizontal axis, which is the direction where the light is more enlarged.

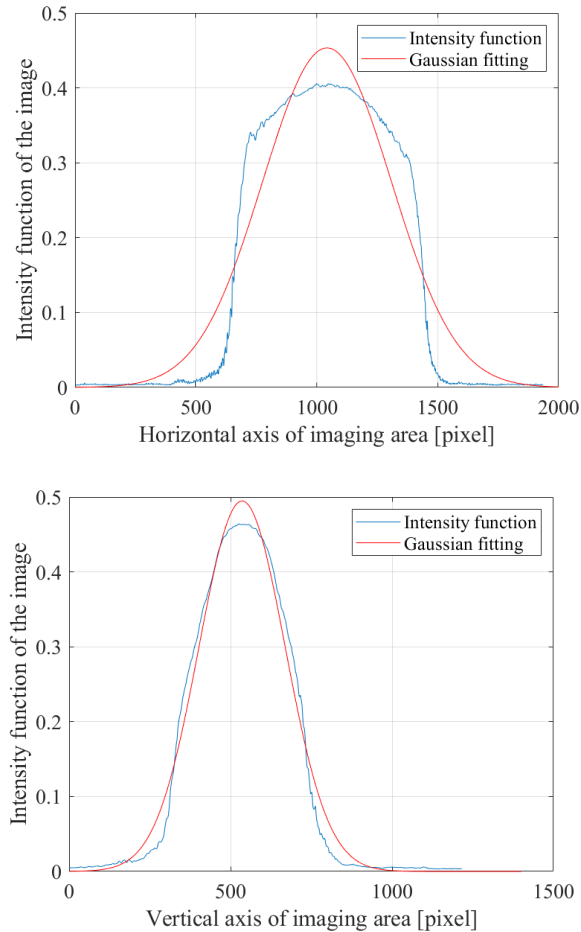


Figure 3.9: Gaussian fitting of the intensity function extrapolated from the image related to the green laser beam at  $z = 30$  mm from the laser output.

Following the same procedure of the He-Ne laser analysis, the experiments concerning the green laser pointer were carried out according to three different configurations: using no lenses for the source characterization, using a spherical lens, and using a cylindrical lens.

Furthermore, the CMOS camera was again used with two Thorlabs filters, *NDUV05A* and *NDUV20A*, in order to avoid the saturation of the acquired images.

### 3.2.1. Source characterization

First of all, the laser source was analysed without other optical components to characterize the output beam and its main parameters. The mounted setup is represented in Fig. 3.10.

Once turned-on the laser pointer, the CMOS camera was moved along the sliding rail to verify that the radiated beam was collimated.

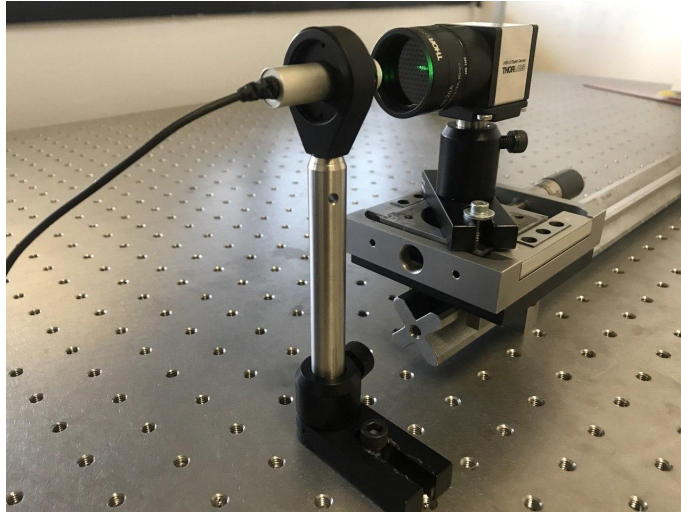


Figure 3.10: Setup for green laser pointer characterization.

In contrast to the He-Ne laser, the green laser has provided a large astigmatism, as shown in Fig. 3.11 and as disclosed in the previous paragraph.

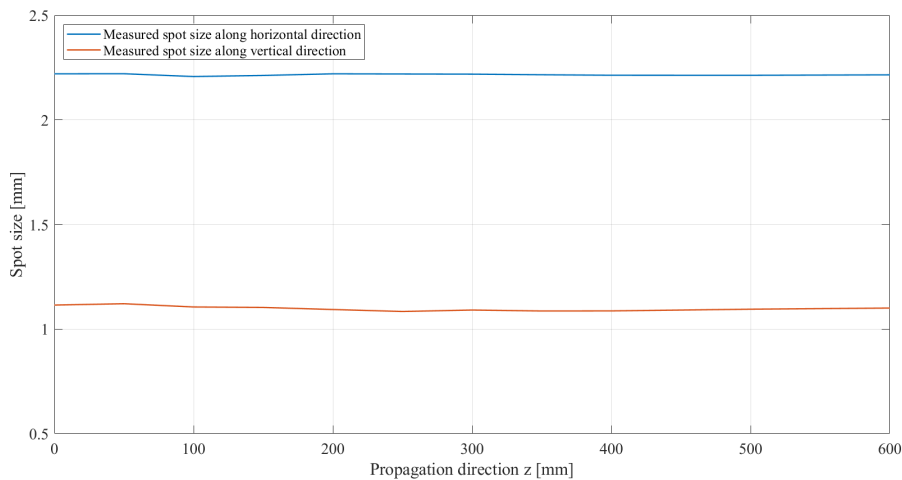


Figure 3.11: Astigmatism of green laser pointer.

The spot size computation of the field along the two propagation directions provided sufficiently constant results, demonstrating that the source beam is collimated. As depicted in Fig. 3.12, the measured and analytical spot sizes are close for the near field measurements, whereas they clearly differ by increasing the distance. Moreover, the measured beam parameters are slightly different from the datasheet. In Tab. 3.7 and Tab. 3.8 the experimental and analytical results are compared.

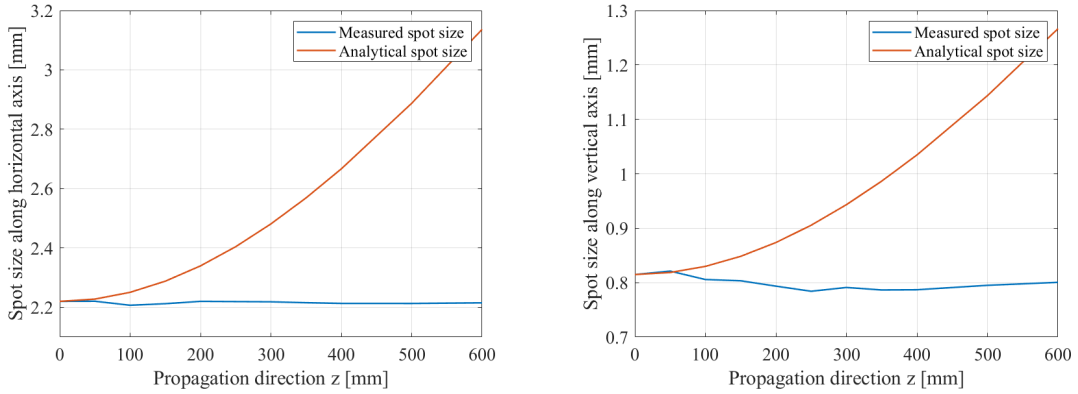


Figure 3.12: Comparison between measured and simulated spot sizes of the green laser pointer.

The reasons why the parameters diverge are the following: the sensitivity of the camera underestimates the real results, due to the set exposure time; the filters attenuate the field tails, leading to a reduction of the real spot size; the divergence angle is not computed in far field conditions because the Rayleigh range is large (about 610 mm for both directions).

Although these discrepancies, the  $M^2$  factor of the source was computed from the experimental values along the horizontal and vertical directions:

$$M_x^2 = 49.53$$

$$M_y^2 = 12.35$$

Table 3.7: Experimental and expected results comparison for green laser source.

	Beam Waist (x y)		Divergence angle (x y)	
Experimental	2.2 mm	0.81 mm	1.8 mrad	3.7 mrad
Datasheet	2.3 mm	0.85 mm	1.5 mrad	> 1.5 mrad

Table 3.8: Experimental and expected BPP for green laser source.

	BPP (x y)	
Experimental	$3.96 \times 10^{-6}$	$3 \times 10^{-6}$
Datasheet	$3.45 \times 10^{-6}$	$> 1.27 \times 10^{-6}$

As expected, the BPP is worse than the one of He-Ne.

The following simulation results concern just the horizontal direction  $x$ , since it is the most critical in terms of deviation from a Gaussian beam.

### 3.2.2. Spherical lens setup

Once analysed all the main parameters of the source, the effect of a lens on the green laser beam was studied. At first, the Thorlabs spherical lens *AC254-080-A* was introduced into the setup (Fig. 3.13).

The spherical lens is characterized by a focal length of 80 mm and, since the output beam of the pointer is collimated, the location of the lens may be chosen as desired (obviously, the residual divergence of the collimated beam has been taken into account). The selected distance among laser source and lens was set to 35 mm.

As well as in the He-Ne laser case, the CMOS camera was arranged in the supposed focal point at the beginning; successively, the image acquisitions were computed by moving the camera back and forth of about 1 mm in order to find the real focal point, and finally also far field measurements have been accomplished.

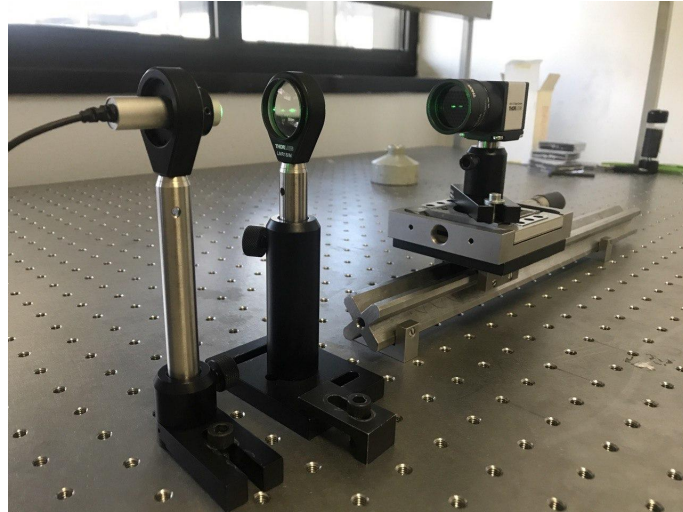


Figure 3.13: Setup mounted to evaluate the effect of a focusing spherical lens on the green laser pointer.

The spot size evolution was simulated by means of the five rays equivalent model (Fig. 3.14), where the spherical lens was treated as an equivalent thin lens. The experimental results are coherent with the numerical ones just around the focal point because the CMOS camera exposure time was set to provide congruent images when located at the focused beam waist position; otherwise, the field tails are attenuated due to camera sensitivity and, as a result, the spot size detected by the camera is underestimated during the beam propagation.

The comparison of the results is shown in Tab. 3.9.

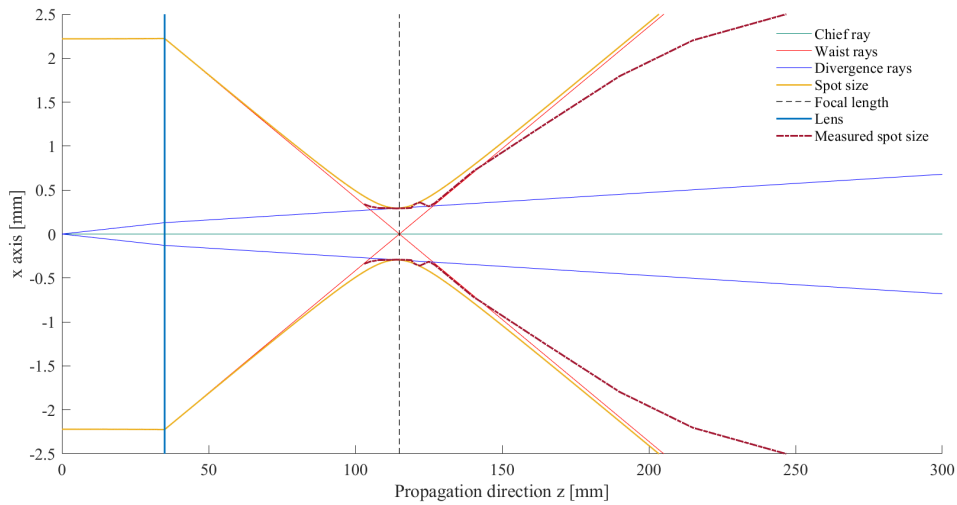


Figure 3.14: Comparison between measured and simulated spot sizes of the green laser through a thin spherical lens.

Table 3.9: Experimental and analytical results comparison for spherical lens setup.

	Beam waist	Divergence angle	BPP
Experimental	292 $\mu\text{m}$	1.8 mrad	$5.26 \times 10^{-7}$
Analytical	295 $\mu\text{m}$	2.1 mrad	$6.2 \times 10^{-7}$

In this case the BPP seems changed due to the introduction of the lens, because of the underestimation of the spot size evolution.

### 3.2.3. Cylindrical lens setup

The last experimental analysis for the validation of the laser beam modeling studied the green laser beam evolution through a cylindrical lens. The exploited optical component is a 50 mm  $\times$  25 mm Edmund Optics plano-convex lens, having a focal length of 100 mm. Being a cylindrical lens, according to its orientation, theoretically it modifies just the one axis of the beam (in this current case the horizontal one), whereas the other should remain unvaried. Actually, due to sensitivity and resolution of the camera, the images of the beam along both axes turned out to be slightly modified.

The picture of the assembled setup is represented in Fig. 3.15.

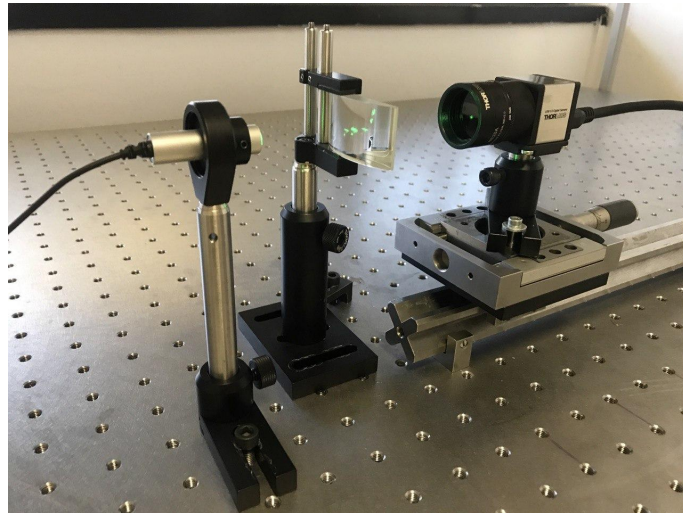


Figure 3.15: Setup mounted to evaluate the effect of a focusing cylindrical lens on the green laser pointer.

Once measured the spot size, the beam propagation through the lens was fulfilled by means of the five rays approach. Unlike the previous case, the cylindrical lens has been described as a thick lens, with a radius of curvature of 51.85 mm and a central thickness of 7 mm.

The result of the simulation is illustrated in Fig. 3.16 and all the considerations on the spherical lens case suit also the current one. Again, the BPP parameter does not remain constant, as shown in Tab. 3.10.

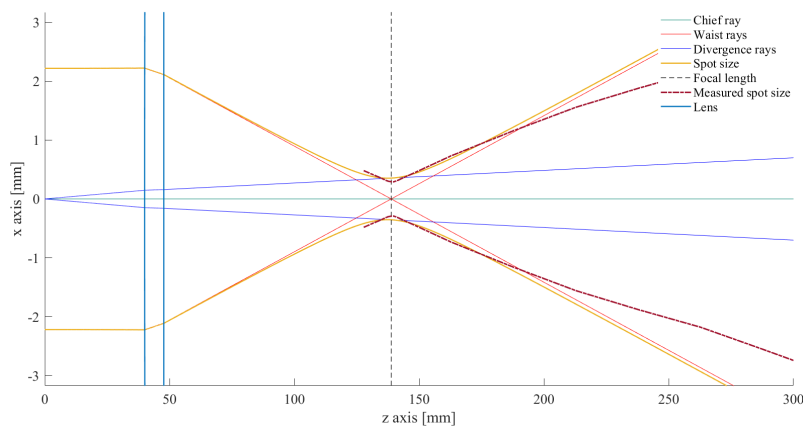


Figure 3.16: Comparison between measured and simulated spot sizes of the green laser through a thick cylindrical lens.

Table 3.10: Experimental and analytical results comparison for cylindrical lens setup.

	Beam waist	Divergence angle	BPP
Experimental	310 $\mu\text{m}$	1.6 mrad	$4.96 \times 10^{-7}$
Analytical	368 $\mu\text{m}$	2.2 mrad	$8.1 \times 10^{-7}$

# Chapter 4

## High Power Laser Module

If a single laser diode chip may be employed as a light source supplying about tens of watts, the combination of more chips provides a powerful output beam. High-power laser diode modules are trivially light generators engaged in direct applications, especially material processing, or in fiber laser pumping.

Their primary advantages are high wall-plug efficiency, high optical power and long lifetime. Unfortunately, besides these benefits, the leading shortcomings are the low brightness and the poor beam quality [32]. The beam quality has the most important role among the module performances because it establishes the number of diodes that can be combined into a given output fiber. Reminding that the beam parameter product for a Gaussian beam is  $BPP = w_0 \cdot \theta$ , the brightness of a laser diode beam (Eq. 4.1) is defined by the laser power  $P$  and the total BPP (Eq. 4.2).

$$B = \frac{P}{\pi^2 BPP_{tot}^2} \quad (4.1)$$

$$BPP_{tot}^2 = BPP_{slow}^2 + BPP_{fast}^2 \quad (4.2)$$

The technological progresses computed in the last few years aim to produce laser modules with a larger amount of power by preserving or increasing performances and by reducing the cost per emitted watt. Concerning production costs, the reduction of laser module price may be obtained by decreasing the number of optical elements and, as a consequence, the assembly time. On the other hand, a brightness enhancement can be achieved by reducing the slow axis divergence and by rising the output power per emitter [32]. Otherwise, the brightness of a laser module is widely improved by means of specific incoherent methods: polarization combining and wavelength multiplexing.

As already quoted in the first chapter, exclusively the incoherent combining is treated in this project work and the primary motivation is the beam phase control. As a matter of fact, all lasers radiations oscillate along two different directions, stimulating at least a lateral fundamental mode and a longitudinal mode. Wherefore, interference arises and techniques of phase stability are requested; particularly, the frequencies must be locked out as well as the phases [33].

In spite of its practicality, the incoherent beam combining limits the potential attainment of high beam quality and does not provide the brightness improvement.

The main cause is the mandatory spacing among chips, producing a reduction of the output beam quality and, as a consequence, of the brightness of the diode stack with respect to the single diode. Even if chips must be as close as possible, heat dissipation is a constraint.

The laser diode modules described next are based on the spatial combining, or rather semiconductor laser chips are located side by side along one or two directions yielding a divergent beam in the FA and the SA directions. Given an array of  $N$  chips, the coupling carried out in a fully incoherent way provides a total beam intensity of  $N$  times the intensity of a single chip. If coherence between diodes occurs, beams begin to interfere, leading to a smaller intensity distribution.

In the following sections the high-power laser modules and their optical components are analysed in detail; finally, the simulations provided by the developed software tool are illustrated and discussed.

## 4.1. Module setup

A multi-emitter laser diode module (Fig. 4.1) consists of stacking multiple single emitter chips in order to develop a compact laser source delivering few hundreds of watts. The main task is to couple the diode beams stack with an output fiber and to obtain an acceptable filling in the fiber core, thus reducing the percentage of power loss. A clear graphical portrayal is depicted in Fig. 4.2.

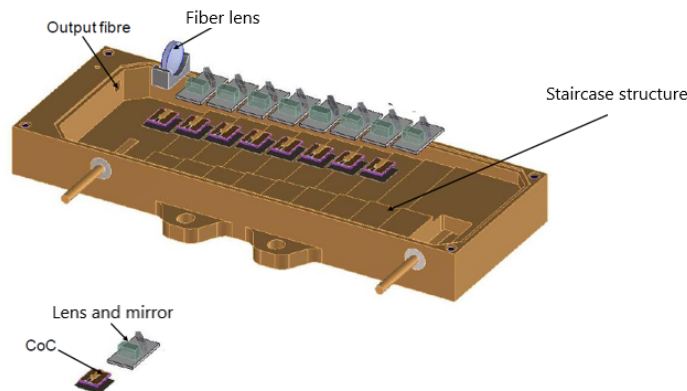


Figure 4.1: Multi-emitter laser diode module.

For an easier overview, some assumptions are implemented [15]:

- all the diodes emitted beams are incoherent with respect to each other; hence interference does not occur;
- the beam divergence after collimation is negligible;
- laser chips have the same specifications;
- lenses are aberrations free;

- the numerical aperture (NA) of each lens is equal to 1; thus, no truncation of the beam takes place.

According to Fig. 4.2, the radiations emitted by laser diodes are divergent along the fast axis and slow axis directions; therefore, the beams need to be collimated by specific cylindrical lenses, called *fast axis collimator* (FAC) and *slow axis collimator* (SAC), leading to a negligible divergence. Firstly, the FAC lenses have to be integrated in the module structure in order to collimate the beams in the FA direction; since the divergence angle along the fast axis is very huge, the FAC lenses are arranged in proximity to the diodes facet and they are marked out by high numerical aperture. Afterwards, the SAC lenses are located, collimating the beams along the SA direction; a high numerical aperture for the SAC lenses is not strictly required.

FAC and SAC lenses are in the same number of the source chips: the propagation of the beams through these collimating lenses is on-axis, or better the lens and the beam optical axis coincide, and latter is is not modified.

The collimated beams are oriented, for example by mirror reflections, towards the output fiber and, at the end, they are incoherently combined through a fiber lens in order to be focused in the fiber core. Sometimes, two fiber lenses are integrated: one lens focalises the beam propagating along the FA direction, whereas the other one focalises the beam in the SA direction.

The transmission inside a fiber is not marked out by contamination and misalignment of optical elements, thus preventing beam quality deterioration [9].

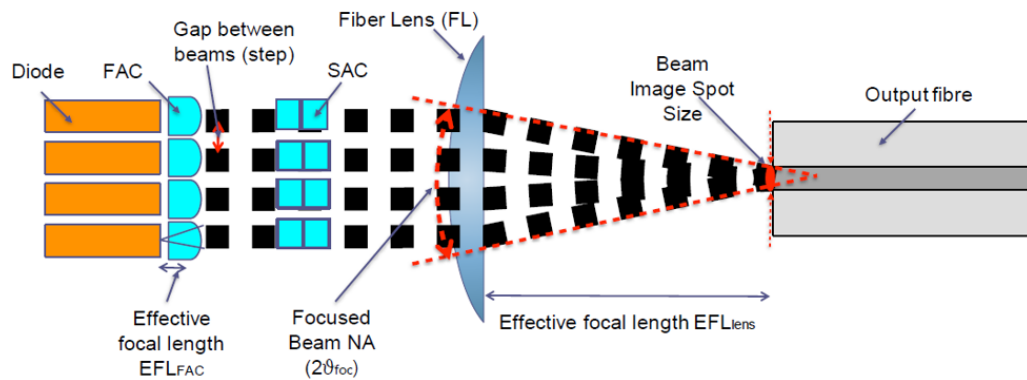


Figure 4.2: Reference scheme for the laser diode module.

## 4.2. Module software preparatory insight

In this section the developed MATLAB tool for the high power laser module simulation is explained to the reader. The software realization is based on a modular structure: in order to achieve high versatility of the tool, object-oriented programming (OOP) approach has been used. Each element involved in the module description, as the module itself, the source chips, the lenses and the five rays set to represent the beams, belongs to a specific class. In OOP the fields that must be filled to identify

the instances of a class are the so called properties; for example, every instance of the class *Lens* is defined by the distance from the source, the focal length and the other geometrical parameters. The objects procedures are named methods and they implement the functions that the class instances can carry out. One example of a method of the class *Lens* is the function that creates the ray transfer matrix associated to the lens starting from its properties data.

As a matter of fact, the OOP method allows a great reusability of the code: in Chapter 5 the software is implemented to reproduce another application, without requiring modifications, except for some simple adjustments.

The software should be considered user-friendly thanks to the proposed Graphical User Interface (GUI), depicted in the following pictures. The GUI offers point-and-click control of the software tool, allowing the user who is not familiar with the programming language to run the application in an efficient way.

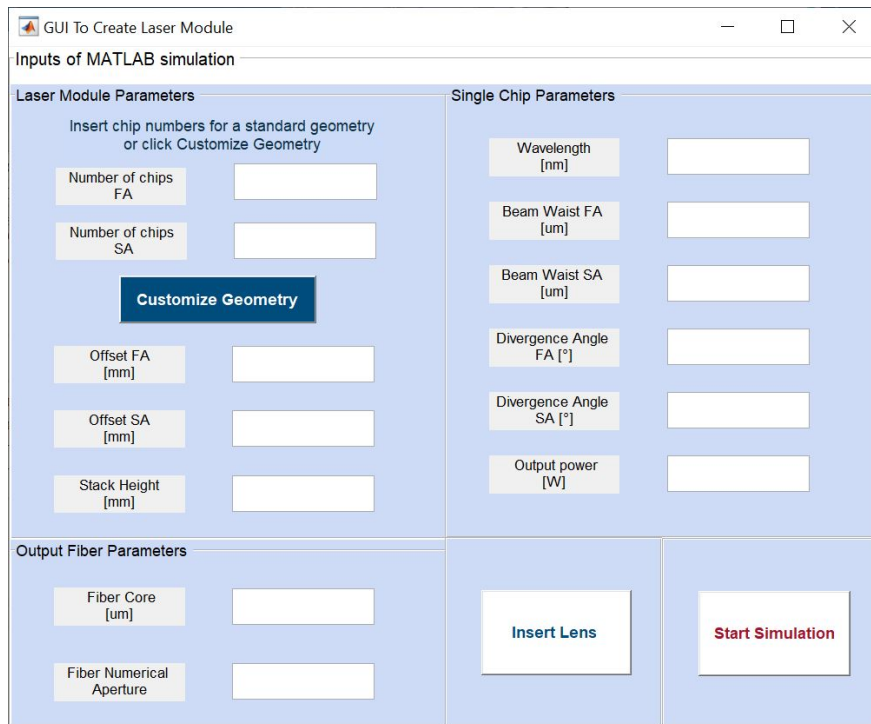


Figure 4.3: Main GUI to set the simulation parameters.

Initially, the user comes across Fig. 4.3 interface, and is required to define the geometry according to which the chips composing the module must be disposed. There are two possibilities: a standard or a customized geometry. The first choice creates a total number of diodes equal to  $Number\ of\ chips\ FA \times Number\ of\ chips\ SA$ ; the first factor describes the number of chips disposed along the vertical direction that give rise to the staircase, whereas the second one is the number of chips placed side by side laterally. If the user needs instead to simulate a different kind of geometry, he can press the push button *Customize Geometry*. Then, he needs to insert two parameters defining an array of possible positions where to collocate the

chips. Each position is identified by a checkbox, that can be selected or left blank if it must not originate a chip. The example of Fig. 4.5 generates 16 chips arranged in a circular layout: such disposition of the sources traces the shape of the fiber core, thus allowing a more uniform filling.

After their arrangement, it is necessary to define the distances between the chips in the 3D space: referring to Fig. 4.4, the *offset SA* concerns the distance among two chips located in two different stacks and at the same height, whereas the *offset FA* is defined as the gap between two nearby diodes in the same stack and, finally, the *stack height* is the vertical distance among two consecutive chips.

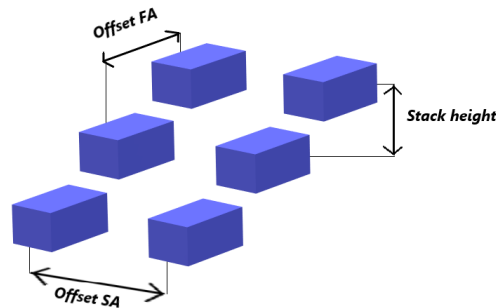


Figure 4.4: Module chips array.

The output fiber must be described by means of the core diameter and the fiber numerical aperture (NA), related to the maximum angle that can enter the fiber and undergo total inner reflection, thus avoiding being refracted and consequently being dissipated in the cladding.

The customer successively can characterize the chips in terms of wavelength, beam waist and divergence angles along both the slow axis and the fast axis, and output power.

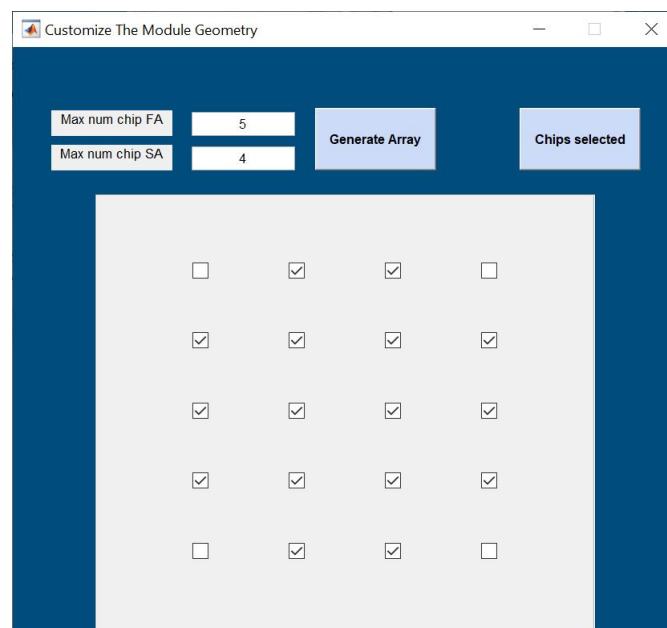


Figure 4.5: GUI to choose the desired chips location.

Once determined the source parameters and the laser diodes disposition, a series of optical elements has to be inserted in the module system: FAC lenses to collimate the beam along the fast axis, SAC lenses to collimate the beam in the other direction and fiber lenses to focalise the total incident beam in the fiber core.

In order to integrate a lens in the structure, the consumer must press the button *Insert Lens*. Afterwards, he has to opt for the thin or thick type of lens according to the desired level of accuracy (Fig. 4.6): indeed, it is necessary to remark that both lenses are described in terms of ray transfer matrix, which is a full-fledged paraxial approximation. Hence, it is suitable for the user to select the lens kind according to the awareness of the parameters. The matrices employed in the tool are described in the second chapter (Eq. 2.8, Eq. 2.9).

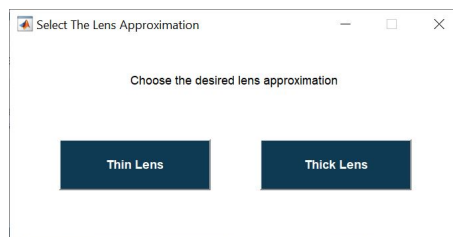


Figure 4.6: GUI to choose the lens type.

As well known, the primary differences among the two lens types are the following: thin lens approximation is much easier because it does not take the lens geometry into account, requesting just the knowledge of the focal point, and it is described by a very simple ray transfer matrix; on the contrary, the thick lens is a more realistic representation, requires a larger number of parameters (e.g. radii of curvature, refractive index, center thickness) and it is characterized by a more complex ray transfer matrix. The GUIs conceived to insert the lenses parameters are depicted in Fig. 4.7.

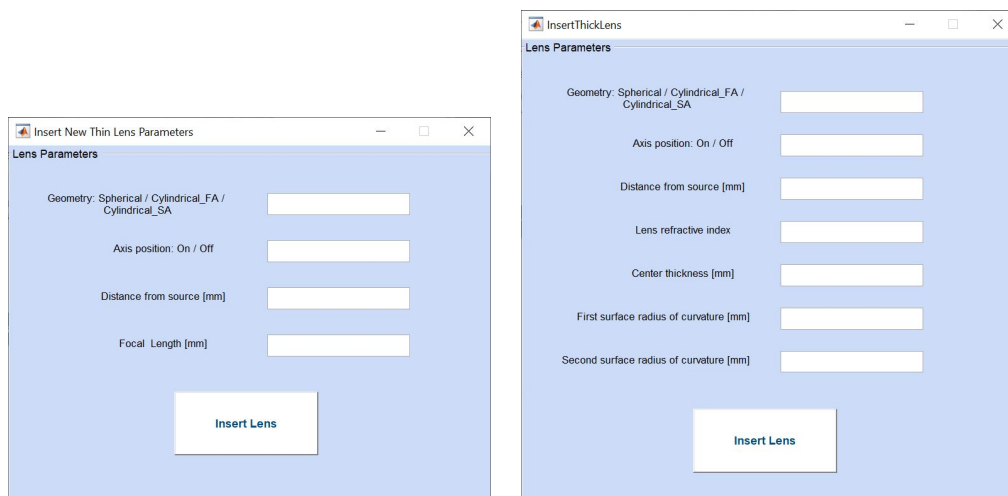


Figure 4.7: GUIs to choose the lenses parameters.

After the creation of the lens instance, the latter is joined to a list containing every lens of the module. Hence, the user can repeat the lens insertion procedure until all the lenses are described. Moreover, the software is able to organise the lenses position according to ascending order, thus it is not mandatory that the lens insertion order follows the module actual layout.

Once the module structure, the source and the optical components are introduced, the user should press the *Start Simulation* button on the main GUI to launch the simulation.

In order to allow the user to visualise the primary parameters of the simulation without accessing the MATLAB *workspace*, the software also includes the possibility to save the module configuration parameters and the most significant output values in a report file automatically generated (Fig. 4.8). The file summarises the adopted parameters to build the laser module, such as lenses position, chips constants etc.; the mainly relevant outputs reported are the spot size of the beams incident on the fiber lens and in the fiber core, the power entering the fiber numerical aperture and the losses due to the beam truncation in the fiber core.

```

25-Sept-2020 09:57:06

The laser module characteristics are presented:
      Number of chips:          8
      Chips offset along SA direction:  0.40 mm
      Chips offset along FA direction:  6.50 mm
      Stack height:             0.40 mm
      Fiber core diameter:       105.00 um
      Fiber numerical aperture:  0.22
-----
Each chip emits a beam characterized by the following parameters.
      Wavelength:              925.000 nm
      Slow axis beam waist:    7.000 um
      Fast axis beam waist:    0.700 um
      Slow axis divergence angle 113.446 mrad
      Fast axis divergence angle 523.599 mrad
      Slow axis M2 factor      2.697
      Fast axis M2 factor      1.245
-----
Each beam undergoes the effect of a "Thin-Cylindrical_FA" lens.
      Distance between lens and chip output: 0.30 mm
      Lens focal length: 0.30 mm

Each beam undergoes the effect of a "Thin-Cylindrical_SA" lens.
      Distance between lens and chip output: 12.00 mm
      Lens focal length: 12.00 mm

Each beam undergoes the effect of a "Thin-Cylindrical_FA" lens.
      Distance between lens and closest chip output: 20.00 mm
      Lens focal length: 18.00 mm

Each beam undergoes the effect of a "Thin-Cylindrical_SA" lens.
      Distance between lens and closest chip output: 29.00 mm
      Lens focal length: 9.00 mm
-----
The beam travelling the longest path to the (last) fiber lens
has the following dimensions.
      Slow axis spot size: 1.3617 mm
      Fast axis spot size: 0.1246 mm
-----
The travelling the longest path to the fiber has the following
dimensions.
      Slow axis spot size: 0.0053 mm
      Fast axis spot size: 0.0420 mm
-----
      The power in the fiber numerical aperture is: 99.514 %
      The losses in the fiber core are: 1.249 %
-----

```

Figure 4.8: Example of report file automatically generated by the software.

### 4.3. Source analysis

The module understanding cannot leave the analysis of its basic elements out of consideration.

Since the developed software allows to realize any kind of chip, initially an example described by realistic parameters is proposed to deduce reasonable values of  $M^2$  and BPP quality factors of the laser diode sources.

Then, a statistical analysis based on the measurement of several chips emissions actually employed as laser modules sources is carried out; this type of investigation is very useful to model the tolerances that distinguish each real chip size and divergence.

#### 4.3.1. $M^2$ and BPP parameters

The emission of a single emitter is exhibited in Fig. 4.9: it is possible to appreciate that the radiation is characteristically astigmatic, or rather the laser output beam has not perfectly Gaussian distribution intensity along one direction. Consequently, the  $M^2$  factor is measured and taken into account in the following analyses. Moreover, in order to compute the beam quality of the laser diode source, the beam parameter product BPP is calculated.

It is well known that a laser diode is characterized by near-diffraction-limited beam quality and a large divergence along the FA direction; on the contrary, in the SA direction the beam quality is worse, but the divergence angle is smaller. In conclusion, the BPP should be better for the fast axis direction.

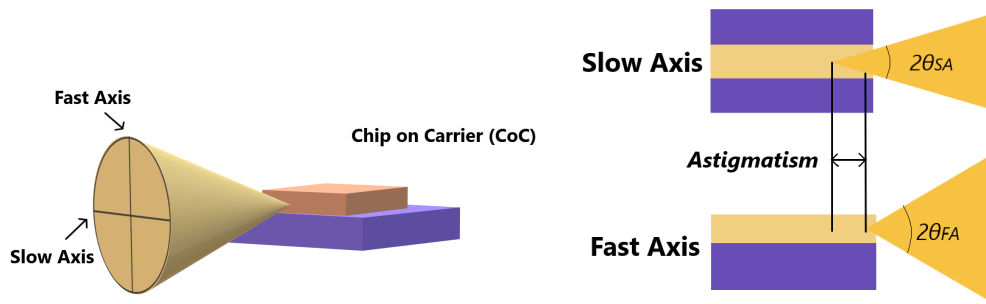


Figure 4.9: Laser diode radiation model.

The characteristics of the 920 nm laser diode source employed in the module are listed in Tab. 4.1: the values chosen are fictitious data useful to esteem the quality of a feasible chip emission.

Table 4.1: Input and quality parameters of the laser diode source.

Parameters	Fast Axis	Slow axis
Beam Waist [ $\mu\text{m}$ ]	0.8	65
Divergence angle [mrad]	524	105
$M^2$	1.43	23.24
BPP [mm·rad]	0.00042	0.00680

As expected from theory, the beam quality along the fast axis is much better than along the slow axis, since the BPP and the  $M^2$  are smaller in the FA direction. The emission at the diode facet is shown in Fig. 4.10.

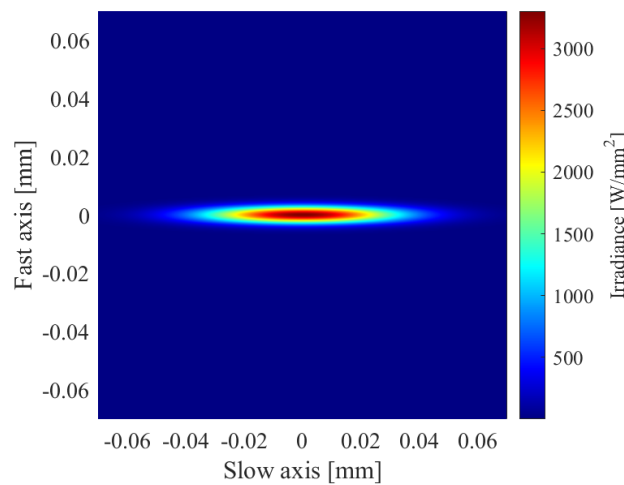


Figure 4.10: Laser diode source emission.

### 4.3.2. Source chips statistical analysis

The software tool is based on the assumption that all the laser diode chips integrated in the laser module have exactly the same characteristics. Obviously, the current simplification has very little to do with the real world, where process variability cannot be avoided.

Indeed, even if laser diodes are characterized by the same nominal values, actually the tolerances cause a slight difference among the parameters of the chips belonging to the same laser module. An input parameter variation provides output parameters fluctuations, that can be associated to a certain probability density function (PDF), used to find the probability of a random variable in a well defined range.

In order to understand the PDF according to which the possible values of a certain amount of laser diode chips are distributed, the emission of several chips has been analysed by resorting to the capabilities of a CCD camera.

Since the current analysis concerns confidential data, the real results cannot be explicitly reported.

Firstly, the laser beam passes through the FAC and the SAC lenses in order to reach the collimation; then, it is focalised by a final spherical lens. The CCD camera is placed in the focal point of the last lens, to acquire the image of the focused beam. The graphical representation of the measurement setup is illustrated in Fig. 4.11.



Figure 4.11: Source analysis reference scheme.

The dimension of the visualised spot is related to the size of the chips by means of the magnification factor, different in the SA and FA directions, defined as the ratio of the focal lengths of the employed lenses.

$$M_{SA} = \frac{f_{foc}}{f_{SAC}}; \quad M_{FA} = \frac{f_{foc}}{f_{FAC}} \quad (4.3)$$

The emission of the selected laser diodes has been acquired by the CCD before to mount the chips in the assigned modules; the obtained images have been analysed to perform a statistic analysis of the samples.

The involved model is stochastic, because the available fluctuations of the output (the dimension of the spot size at the camera), are exploited in order to understand the corresponding unknown variations of the input (the chip length and height). It is assumed that, if the input variability is defined by a certain probability distribution, also the output variations must follow the same law. Analogously, the distribution that best fits the CCD data is therefore exploited to build the probability distribution of the input data.

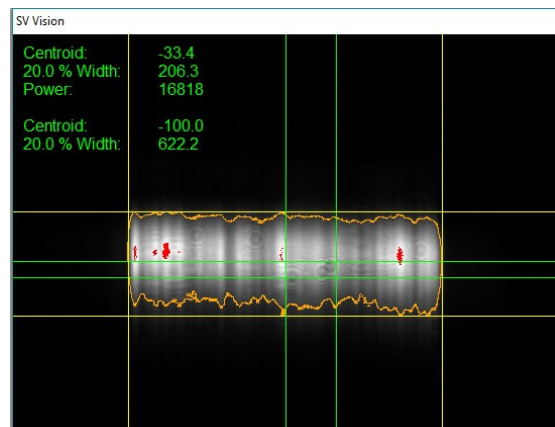


Figure 4.12: Beam captured by the CCD camera.

The first step is to analyse the images provided by the camera (e.g. Fig. 4.12) by extracting the spot size values using the proper pixel to  $\mu\text{m}$  conversion. About 100 samples have been collected to compute a satisfactory statistical analysis. The histogram representing the information is approximately symmetrical with respect to the mean value, therefore the best fitting probability distribution is a Gaussian, as proved in Fig. 4.13.

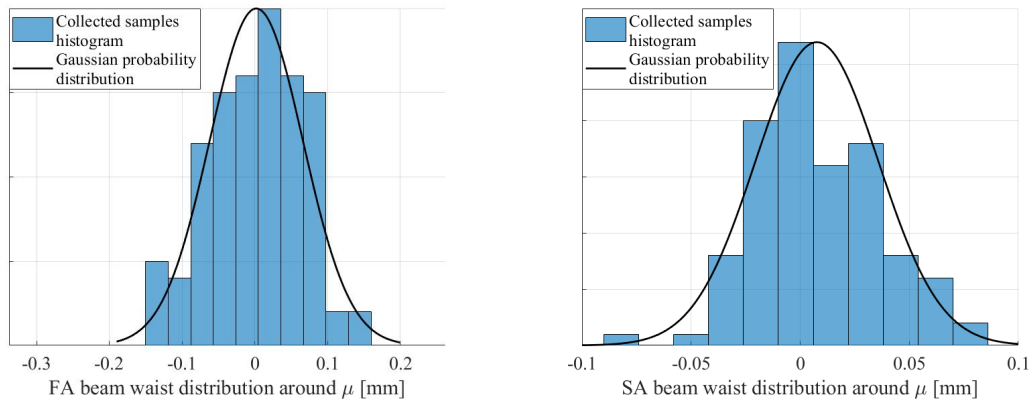


Figure 4.13: Histograms of collected data along the beam two directions.

Once established that the output and the input beam parameters obey a Gaussian probability density function, the sources divergence angles have been distributed according to the mean and the variance values (Tab. 4.2), measured experimentally in far-field conditions. In Fig. 4.14 the PDFs are represented as a function of the variance: the Gaussian distribution along the fast axis is broader due to the larger variance.

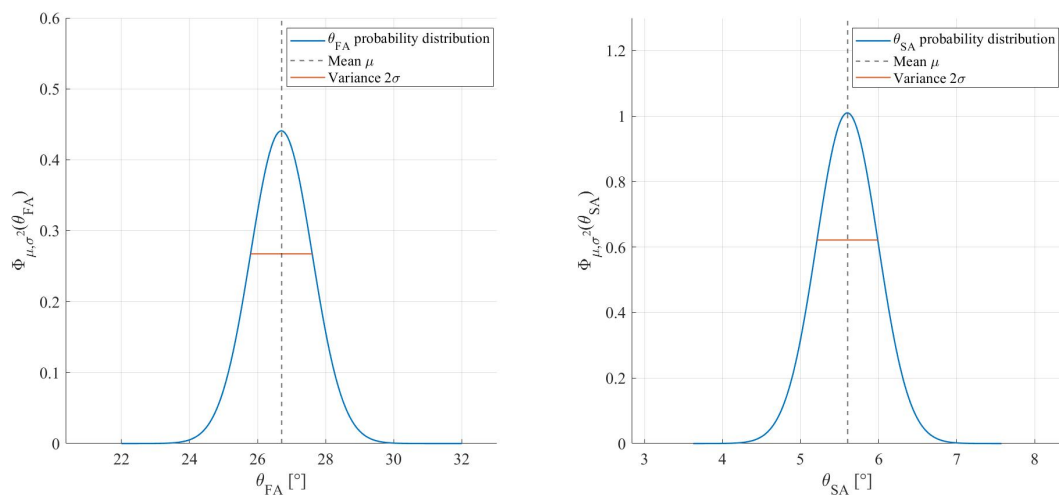


Figure 4.14: PDF of SA and FA divergence angles.

Table 4.2: Mean and variance divergence angles along the beam axes.

	Mean	Variance
Slow Axis Half Divergence [°]	5.6	0.395
Fast Axis Half Divergence [°]	26.7	0.905

Thereafter, a set of 500 simulations, emulating the beam propagation through the optical system of Fig. 4.11, has been performed: for each simulation the chip beam waists were kept constant, whereas the divergence angles were chosen randomly from the Gaussian distributions depicted in Fig. 4.14.

From the resulting spot sizes distribution in the last lens focal point, the Gaussian mean and variance were extrapolated and confronted with the ones describing the spot sizes detected by the camera. The percent error between the mean values of the two set of results (Tab. 4.3) is lower than 10%, thus the developed model used for the beam propagation is affirmed to be reliable.

As demonstrated in Fig. 4.15, the representation of the beam along the fast axis is very accurate because the proper  $M^2 = 1.288$  factor has been introduced. On the contrary, the radiation along the slow axis is less accurate due to the large  $M^2$  factor, leading to a non-Gaussian distribution.

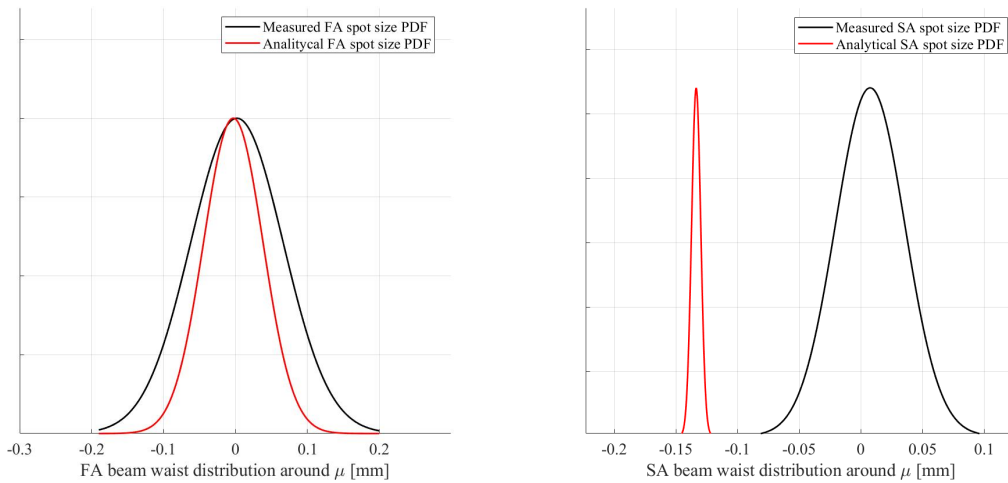


Figure 4.15: Comparison between measured and simulated PDF of the spot sizes.

Table 4.3: Error analysis results.

	PDFs mean values error [%]
Fast Axis	0.28
Slow Axis	4.49

## 4.4. Field propagation inside the module

After the analysis of the laser diode sources, a more substantiated description of the beam propagation inside the module follows. In order to explain every detail of the beams propagation inside the module, the example of a simple structure is proposed. The module is composed by a single staircase (stack height = 0.45 mm), made up of 9 chips emitting at 920 nm. Each one delivers an optical power of 2 W, therefore it is expected that the module output power is 18 W, since the fully incoherent combining has been implemented. The basic configuration concerns a single fiber lens, or rather a spherical lens causing the focalisation of both the SA and the FA in the fiber core. The parameters employed in the simulations are reported in Tab. 4.4.

Table 4.4: Parameters of the laser diode module example.

Parameters	Fast Axis	Slow axis
Beam waist [ $\mu\text{m}$ ]	0.8	65
Divergence angle [mrad]	524	105
Chips offset [mm]	7.5	-
Collimating lens EFL [mm]	0.3	12
Fiber lens EFL [mm]	12	12

Fig. 4.16 shows the chip fields at a distance  $z = 20$  mm from the source, so after the collimation of both axes; the beams mainly spread along the horizontal axis, since the diodes facet dimension along the SA is about two orders of magnitude larger than the one along FA.

The propagation through the module optical system has been described by means of the five rays equivalent model, that is the most convenient approach to represent the manipulation operated by the lenses on the beam. In general, rays cannot provide the beam intensity profile, in fact they define only the evolution of the spot size. Then, in order to visualise the irradiance distribution of the beams propagating in the module, it is necessary to resort to the Gaussian beam expressions; in particular the beam waist knowledge and the  $M^2$  factor are fundamental to fully determine the beam behavior. The beam waist value is unknown after the beam transformations due to the lenses, but it is implicitly contained in the spot size measurement at a certain distance from the beam origin. The  $M^2$  factor is instead evaluated basing on the source parameters, reasonably assuming that it is not affected by the lenses operation.

Eventually, by exploiting the spot size values available thanks to the ray tracing technique, the irradiance profile is obtained.

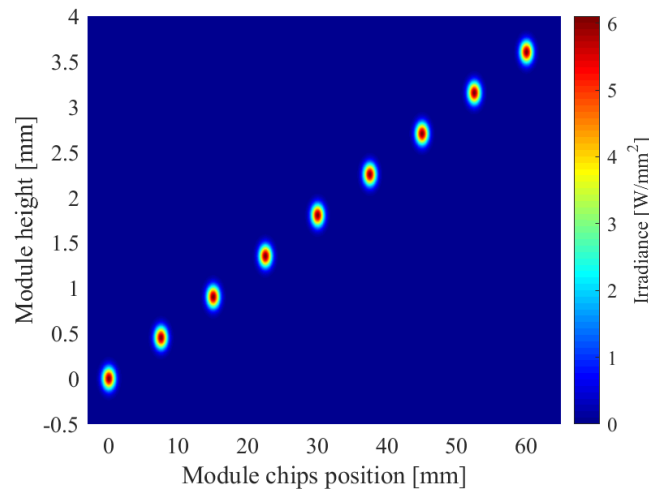


Figure 4.16: Chip beams of the module at  $z = 20$  mm from the sources.

According to the chips position, the beams propagating in the module have different dimensions and intensities in a given propagation coordinate because of what is defined as *offset FA*: if placing the origin of the frame of reference in the chip more distant from the output, the larger such offset, the smaller the path that separates the chip and the output fiber. If a beam propagates for a longer distance, its irradiance peak value decreases because the power, that is maintained constant along the propagation, is distributed over a larger spot size area. This phenomenon can be observed in the case of the total field incident on the fiber lens, where the farthest chip of the module is in the lower position (Fig. 4.17). Indeed, once crossed the FAC and SAC lenses, the chips radiations propagate up to high reflective mirrors, deviating the beams direction towards the fiber lens: being the mirrors in front of the related laser diodes, the path from the mirror to the fiber lens is different for each beam. Despite the presence of mirrors in the actual module structure, in this thesis project the mirror analysis has not been implemented.

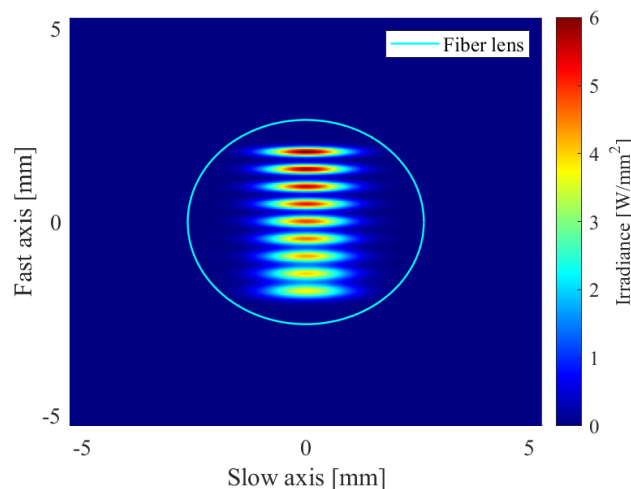


Figure 4.17: Module radiation incident on the fiber lens.

The distance between the fiber lens and the closest chip is 20 mm. Even if it was assumed that the collimating lenses do not cause truncation of the incoming beam, being their diameter much larger than the beam spot size, in the case of the fiber lens (Fig. 4.18) also the diameter must be considered, because it affects the power delivered to the fiber.

Indeed, in order to allow the beam propagation inside the fiber, the numerical aperture of the incident beam must be smaller or, at most equal, to the fiber numerical aperture: the condition Eq. 4.4 must be verified.

$$NA_{beam} \leq NA_{fiber} \quad (4.4)$$

The beam numerical aperture is computed basing on the beam diameter, given by the spot sizes along the slow and fast axes ( $D_{beam} = 2\sqrt{w_{SA}^2 + w_{FA}^2}$ ), and on the focal length of the lens causing the beam focalisation or collimation.

$$NA_{beam} = \frac{D_{beam}}{2f_{lens}} \quad (4.5)$$

Since the maximum value that the beam numerical aperture can assume in order to avoid the truncation by a lens is equal to the lens numerical aperture ( $NA_{beam} \leq NA_{lens}$ ), starting from Eq. 4.4 it is possible to relate  $NA_{lens}$  to  $NA_{fiber}$ . The diameter  $D$  of the fiber lens able to focalise in the fiber core a beam that, by virtue of its numerical aperture, can undergo total inner reflection and therefore can be propagated, is then expressed as:

$$D = f_{lens} \cdot 2NA_{fiber} \quad (4.6)$$

At the end, the total field is focalised in a fiber, precisely placed in the focal point of the fiber lens, thus providing the optimum fiber core filling (Fig. 4.18). The employed fiber is characterized by a core diameter of 155  $\mu\text{m}$  and it is possible to observe at first glance how the combined beam is well centered in the fiber core, leading to just a few power loss percentage. Clearly, the final irradiance is larger than the one shown previously, since the total power of 18 W is focused in a very small area.

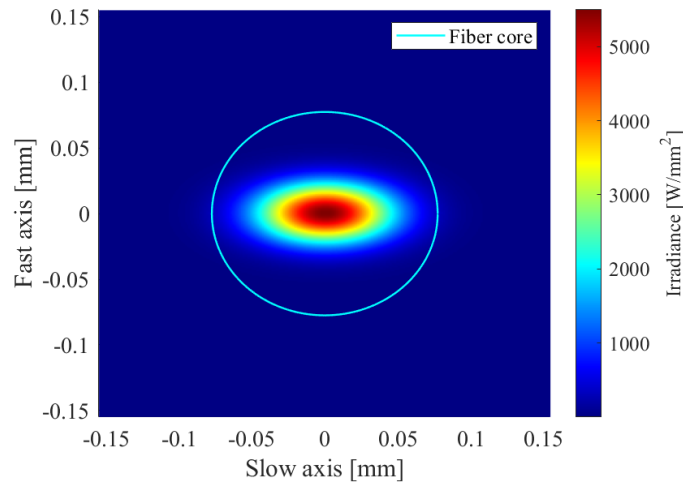


Figure 4.18: Beam focalised in the fiber core by one fiber lens.

The software gives the possibility to include in the module two different fiber lenses, useful to focalise the slow and the fast axes of the beam separately, and consequently more precisely. It is fundamental that the two lenses cause the beams focusing in the same propagation coordinate, because the fiber must be placed in the point where the spot size is minimum. If the previous constrain is not met, the fiber losses and the module performances get worse.

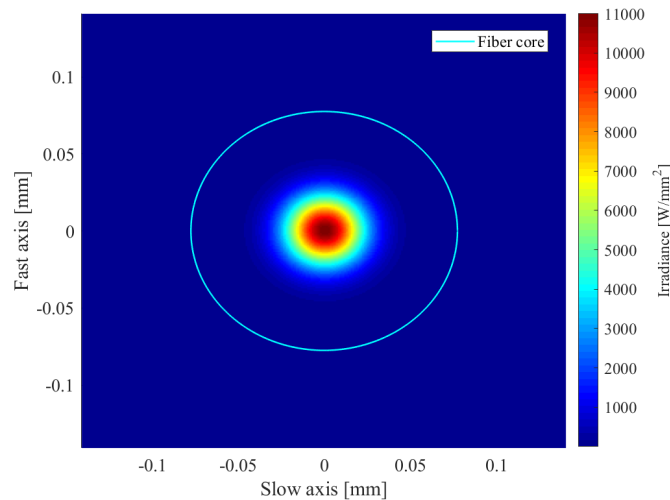


Figure 4.19: Beam focalised in the fiber core by two fiber lenses.

As illustrated in Fig. 4.19, the total beam is better focalised in the fiber core, leading to power losses of 0.001%. Despite the losses reduction, the solution with two fiber lenses is more expensive in terms of assembling time and optical devices costs.

It is essential to specify that the utility of the spatial offsets between the chips is to reach the maximum possible power at the fiber input: the higher the number of beams reaching the fiber lens, the more the power delivered by the system.

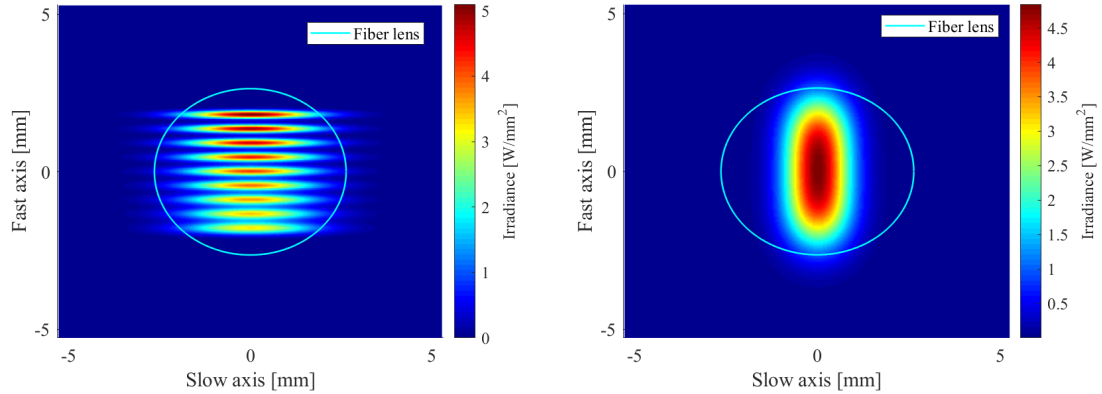
Therefore, the position and the focal length of the FAC and the SAC lenses are fundamental, because they determine the dimensions of the input field of the fiber lens. If the spot sizes increase too much before the collimation, the fiber lens and consequently the fiber core filling cannot be optimal, and the power coupled to the output decreases significantly.

Tab. 4.5 first line refers to Fig. 4.17, obtained with the ideal lenses configuration that provides a very high power incident on the fiber lens. The remaining examples (shown in Fig. 4.20) prove clearly that, if the collimating lenses are placed too far with respect to the source, the beams emission collected by the lens is truncated.

When increasing the FAC focal length and distance, it is not possible to distinguish anymore the contribution of each source, because the beams, due to the huge fast axis divergence, are superimposed.

Table 4.5: Power entering the fiber lens in different collimating lenses configurations.

FAC EFL	SAC EFL	Power in NA
0.3 mm	12 mm	99.9183 %
0.3 mm	24 mm	93.1049 %
3 mm	12 mm	94.2404 %

Figure 4.20: Beam irradiance at the fiber lens for  $EFL_{FAC} = 0.3$  mm;  $EFL_{SAC} = 24$  mm (left) and  $EFL_{FAC} = 3$  mm;  $EFL_{SAC} = 12$  mm (right).

## 4.5. Simulation results

Several simulations have been carried out to demonstrate the benefits of the developed tool. However, before to show the simulation outcomes, the correctness of the provided results has to be proved. Therefore, another software was involved: the *LD Module Design*, realized by the Dr. Hao Yu [5]. His software is equipped by a GUI for the insertion of the input data and is able to produce the same outputs of the MATLAB tool: the total field intensity at the fiber lens input and the focalised beam intensity in the fiber core.

Despite its clarity and its user-friendliness, the *LD Module Design* program is marked out by the following limitations:

- maximum 4 types of lenses can be introduced along each chip path (one FAC, one SAC and two fiber lenses), which is ideal for the laser module, but makes it difficult to adapt the program to simulate a different optical system;
- lenses are implemented only according to the thin lens approximation;
- arrays are always symmetric, or better it is not possible to realize different stacks with different number of chips.

These are the reasons why the MATLAB software developed during the thesis project could be regarded as an improvement of the Dr. Yu program. Indeed, as it is possible to appreciate from Section 4.2, the tool is versatile and mostly modular, particularly

it may be employed to design whatever optical system including an indefinite number of lenses and arrays with different chips.

Thereafter, some examples have been reported to illustrate the coherence and the accuracy of the tool. Furthermore, the comparison results between the two tools are reported: the difference among the two software programs is always below 1%. Moreover, the error can be further improved by increasing the mesh points of the plots, since sometimes it can be considered just a numerical error. The last proposed example concerns a module composed by chips defined by the same nominal values, but then the actual parameters implemented in the simulation are set according to a Gaussian distribution around the nominal values. In this way, a more realistic configuration has been represented.

In conclusion, the developed software under test is validated.

#### 4.5.1. Single laser diodes stack

The simulations in Fig. 4.21 and Fig. 4.22 concern a single laser diodes stack characterized by the parameters reported in Tab. 4.6. The simulations outputs are compared and illustrated in Tab. 4.7.

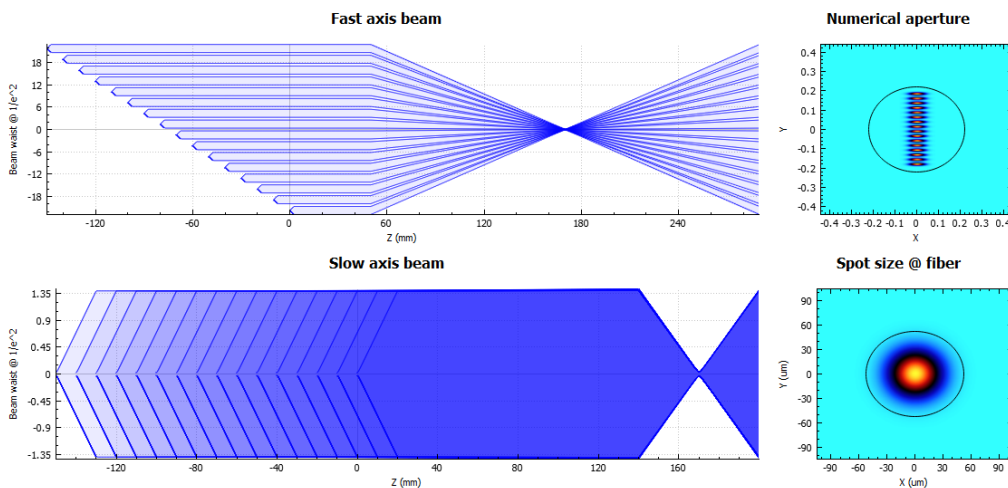


Figure 4.21: First module configuration: Yu outcome.

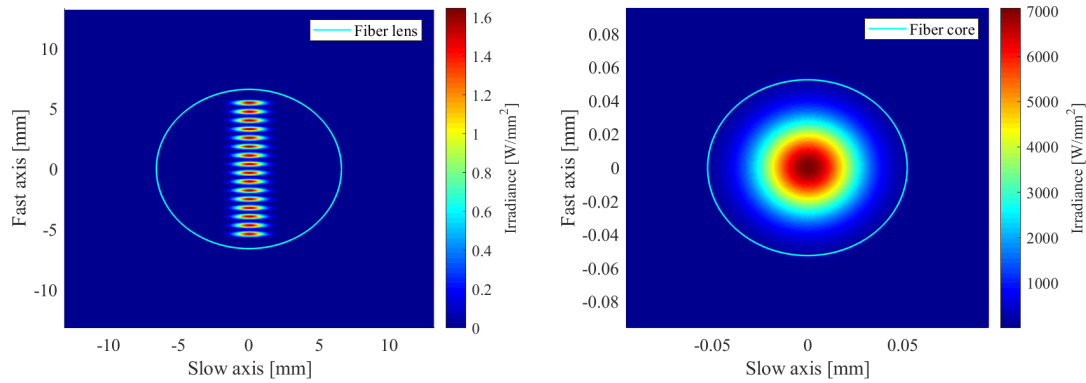


Figure 4.22: First module configuration: field at fiber lens and in fiber core.

Table 4.6: Parameters of first module configuration with wavelength = 450 nm and stack height = 2.9 mm.

Parameters	Fast Axis	Slow axis
Beam waist [ $\mu\text{m}$ ]	0.8	25
Divergence angle [mrad]	436	69.8
Chips offset [mm]	10	-
Collimating lens EFL [mm]	2.5	20
Fiber lens EFL [mm]	120	30
Fiber lens position [mm]	50	140

Table 4.7: First module configuration outputs with fiber core diameter = 105  $\mu\text{m}$  and NA = 0.22.

	MATLAB	LD Module Desgin	Difference [%]
Power losses in fiber [%]	2.2034	2.1862	0.79
Power in NA [%]	100	100	0.000

#### 4.5.2. Super-Gaussian laser diodes stack

The simulations in Fig. 4.23 and Fig. 4.24 concern a super-Gaussian laser diodes stack characterized by the parameters reported in Tab. 4.8. The simulations outputs are compared and illustrated in Tab. 4.9.

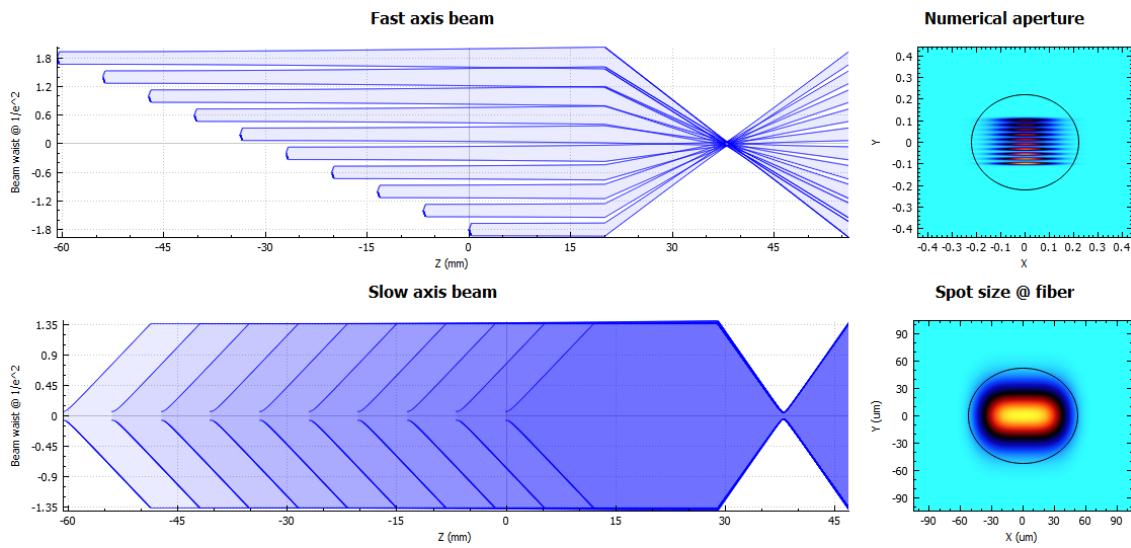


Figure 4.23: Second module configuration: Yu outcome.

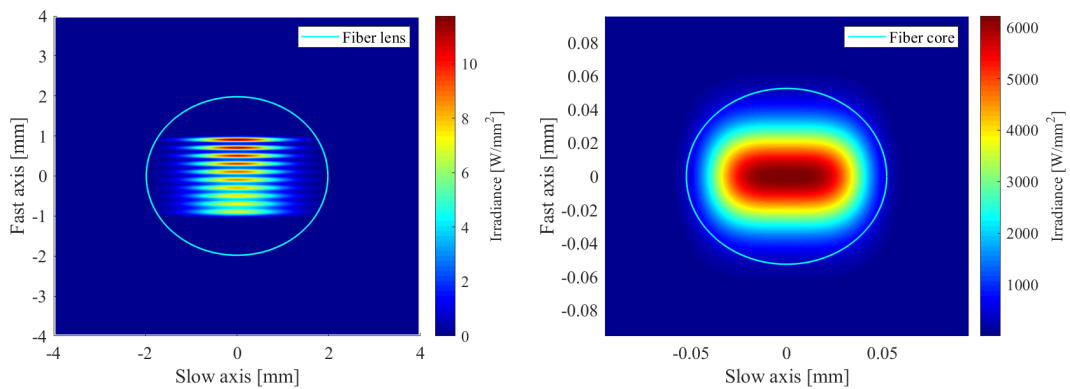


Figure 4.24: Second module configuration: field at fiber lens and in fiber core.

Table 4.8: Parameters of second module configuration with wavelength = 920 nm and stack height = 0.4 mm.

Parameters	Fast Axis	Slow axis
Beam waist [ $\mu\text{m}$ ]	0.7	65
Divergence angle [mrad]	436	113
Chips offset [mm]	6.75	-
Collimating lens EFL [mm]	0.3	12
Fiber lens EFL [mm]	18	9
Fiber lens position [mm]	20	29

Table 4.9: Second module configuration outputs with fiber core diameter = 105  $\mu\text{m}$  and NA = 0.22.

	MATLAB	LD Module Desgin	Difference [%]
Power losses in fiber [%]	4.8123	4.7650	0.99
Power in NA [%]	99.3444	99.3510	0.01

### 4.5.3. Double laser diodes stacks

The simulations in Fig. 4.25 and Fig. 4.26 concern two laser diodes stacks described by the parameters reported in Tab. 4.10. The simulations outputs are compared and illustrated in Tab. 4.11.

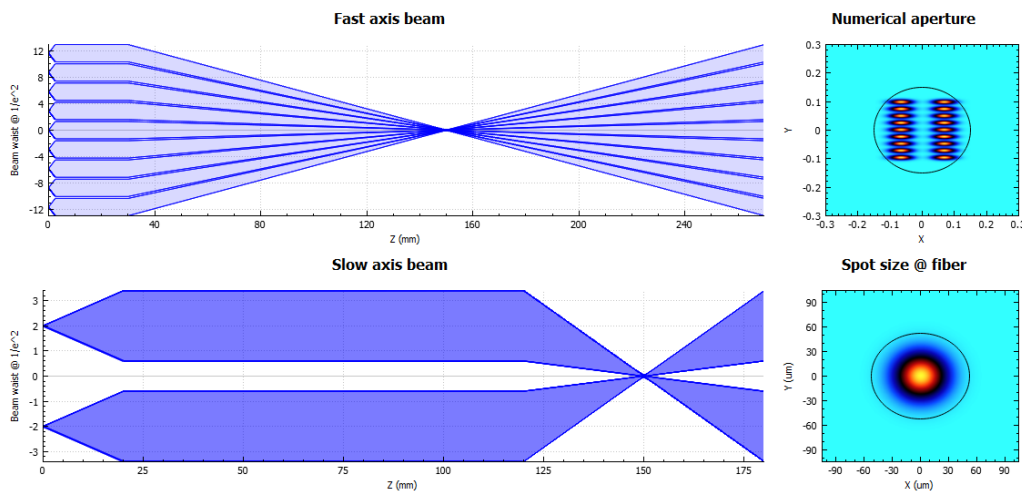


Figure 4.25: Third module configuration: Yu outcome.

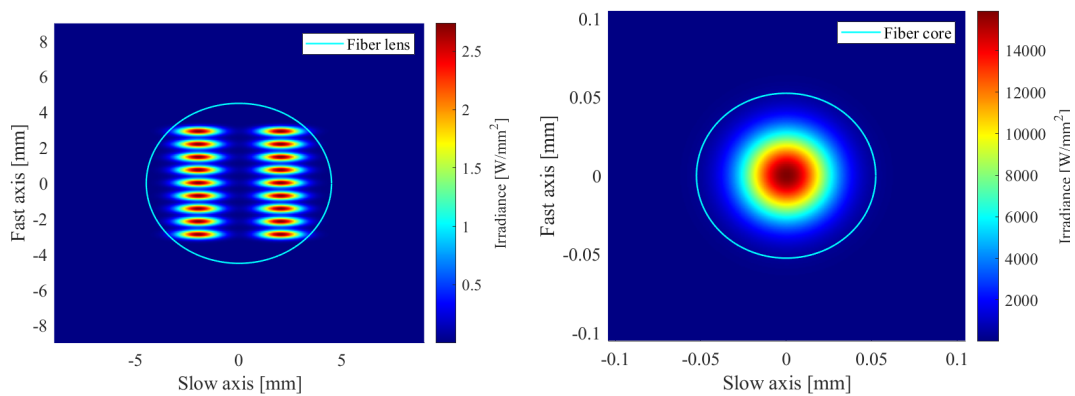


Figure 4.26: Third module configuration: field at fiber lens and in fiber core.

Table 4.10: Parameters of third module configuration with wavelength = 450 nm and stack height = 2.9 mm.

Parameters	Fast Axis	Slow axis
Beam waist [ $\mu\text{m}$ ]	0.8	25
Divergence angle [mrad]	524	69.8
Chips offset [mm]	0	4
Collimating lens EFL [mm]	2.5	20
Fiber lens EFL [mm]	120	30
Fiber lens position [mm]	30	120

Table 4.11: Third module configuration outputs with fiber core diameter = 105  $\mu\text{m}$  and NA = 0.15.

	MATLAB	LD Module Desgin	Difference [%]
Power losses in fiber [%]	2.2031	2.1864	0.78
Power in NA [%]	99.3924	99.4056	0.01

#### 4.5.4. Multiple stacks

The simulations in Fig. 4.27 and Fig. 4.28 concern multiple laser diodes stacks characterized by the parameters reported in Tab. 4.12. The simulations outputs are compared and illustrated in Tab. 4.13.

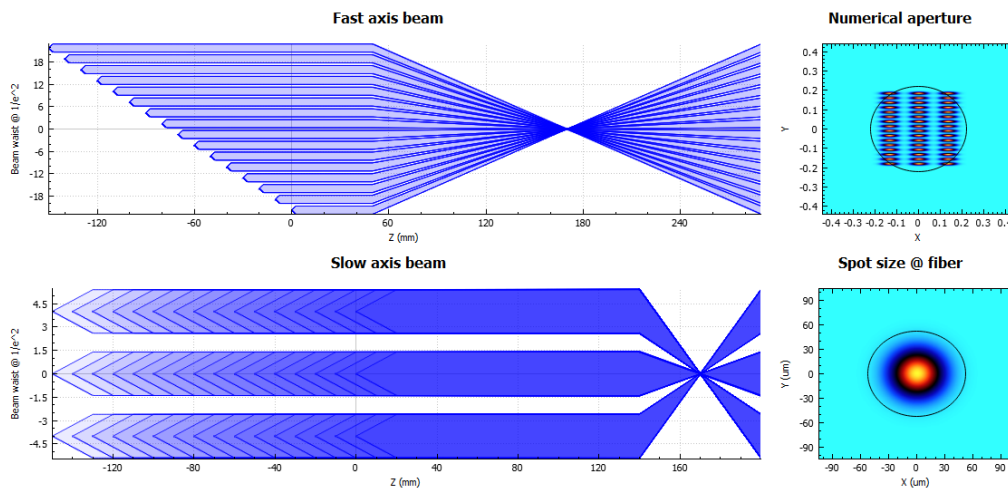


Figure 4.27: Fourth module configuration: Yu outcome.

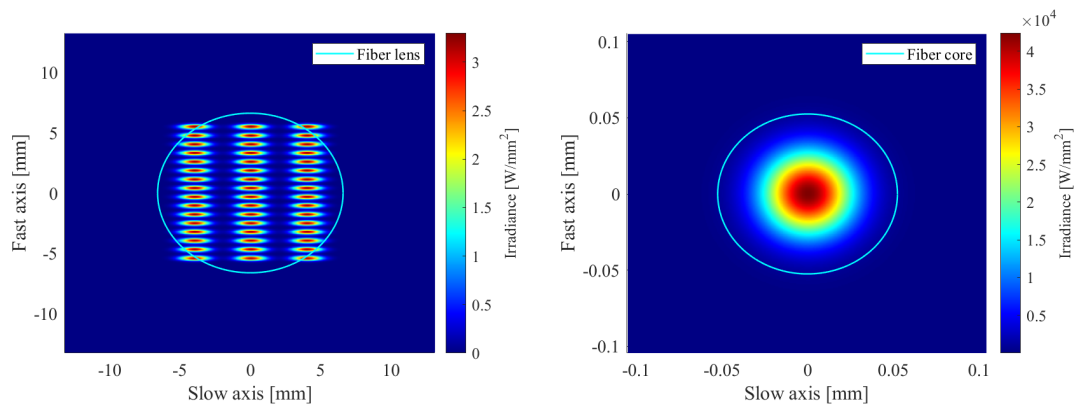


Figure 4.28: Fourth module configuration: field at fiber lens and in fiber core.

Table 4.12: Parameters of fourth module configuration with wavelength = 450 nm and stack height = 2.9 mm.

Parameters	Fast Axis	Slow axis
Beam waist [ $\mu\text{m}$ ]	0.8	25
Divergence angle [mrad]	436	69.8
Chips offset [mm]	10	4
Collimating lens EFL [mm]	2.5	20
Fiber lens EFL [mm]	120	30
Fiber lens position [mm]	50	140

Table 4.13: Fourth module configuration outputs with fiber core diameter = 105  $\mu\text{m}$  and NA = 0.22.

	MATLAB	LD Module Desgin	Difference [%]
Power losses in fiber [%]	2.2034	2.1869	0.74
Power in NA [%]	93.3675	92.6626	0.29

#### 4.5.5. New geometries

The purpose of the following set of simulations is to demonstrate the versatility of the software by realizing new structures to assure the best fiber filling.

As first example, the third simulation (Fig. 4.28) is produced again with the same parameters, in order to improve the power in the fiber NA. Modifying the number of the chips composing each of the three stacks by means of the developed tool (Fig. 4.29), the power in NA is increased of about 6.5% with respect to the previous simulation. Instead, the power losses in the fiber core remain unchanged because spherical aberrations are not taken into account, hence every chip emission converges in the same focal point. For this reason, the chips removal does not provide any power losses improvement. The simulation results are shown in Tab. 4.14.

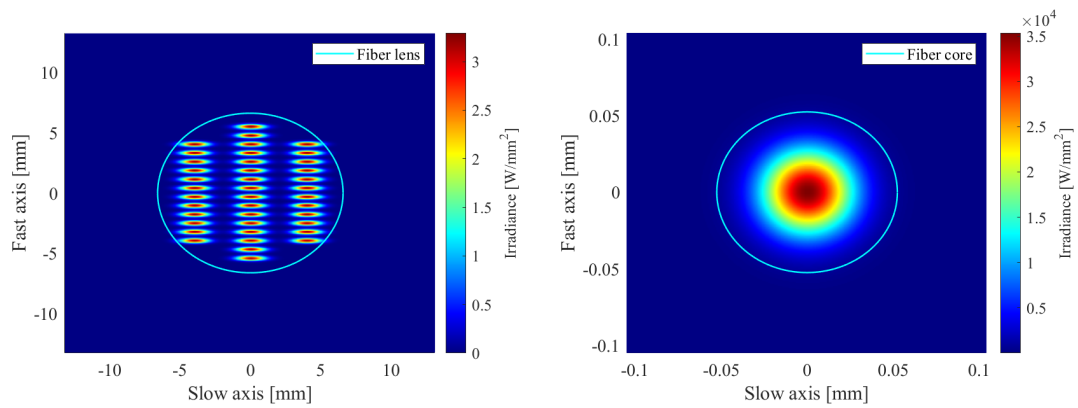


Figure 4.29: Fifth module configuration field at fiber lens and in fiber core.

Table 4.14: Fifth module configuration outputs with fiber core diameter = 105  $\mu\text{m}$  and NA = 0.22.

	MATLAB
Power losses in fiber [%]	2.2034
Power in NA [%]	99.4693

An additional simulation has been carried out to demonstrate an accurate fiber core filling obtained by choosing a circular chips arrangement (Fig. 4.30).

The input and output parameters are respectively reported in Tab. 4.15 and Tab. 4.16.

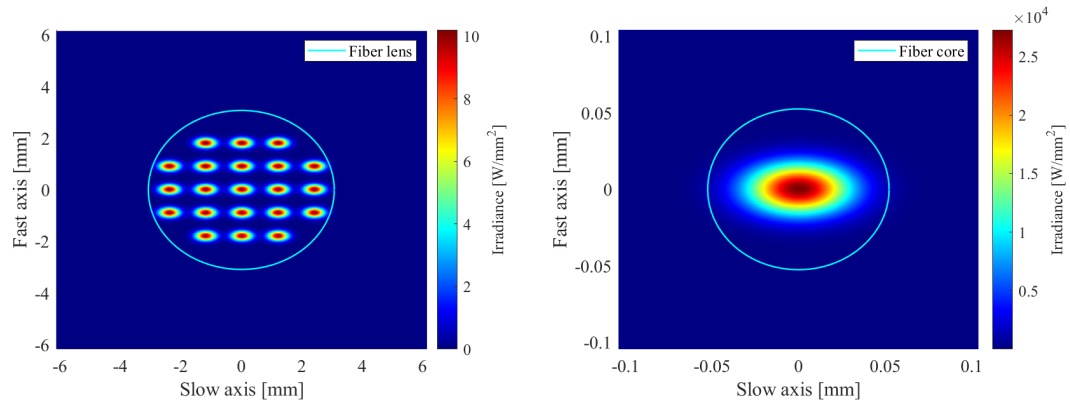


Figure 4.30: Sixth module configuration field at fiber lens and in fiber core.

Table 4.15: Parameters of sixth module configuration with wavelength = 450 nm and stack height = 0.9 mm.

Parameters	Fast Axis	Slow axis
Beam waist [ $\mu\text{m}$ ]	0.8	27
Divergence angle [mrad]	436	52.4
Chips offset [mm]	4	1.2
Collimating lens EFL [mm]	0.6	9
Fiber lens EFL [mm]	14	14
Fiber lens position [mm]	20	20

Table 4.16: Sixth module configuration outputs with fiber core diameter = 105  $\mu\text{m}$  and NA = 0.22.

	MATLAB
Power losses in fiber [%]	1.552
Power in NA [%]	99.734

#### 4.5.6. Double laser diodes stacks - chips statistical analysis

The presented simulation is intended to reproduce a case more realistic than the previous ones: all the chips are not defined by the same parameters in terms of source beam size and divergence angles. The implementation is still far from a fully accurate description of the module, in which all the parameters, such as the chips wavelength of emission, location and emitted power, would be affected by tolerances. In order to provide a comparison with an ideal case, the configuration reported in Tab. 4.10 is proposed again by modifying the values of the beam waists and of the divergence angles. The parameters of the chips are randomly picked within a Gaussian distribution centered around the nominal values; in the case of the beam waist along the two directions the variance value is the 10% of the mean value, the variance of the divergence angles distributions is instead the 5% of the central value.

The simulation provides different output power values (Tab. 4.17) with respect to the ideal configuration and, moreover, it is possible to observe in Fig. 4.31 that the beams incident on the fiber lens are characterized by different irradiance distributions.

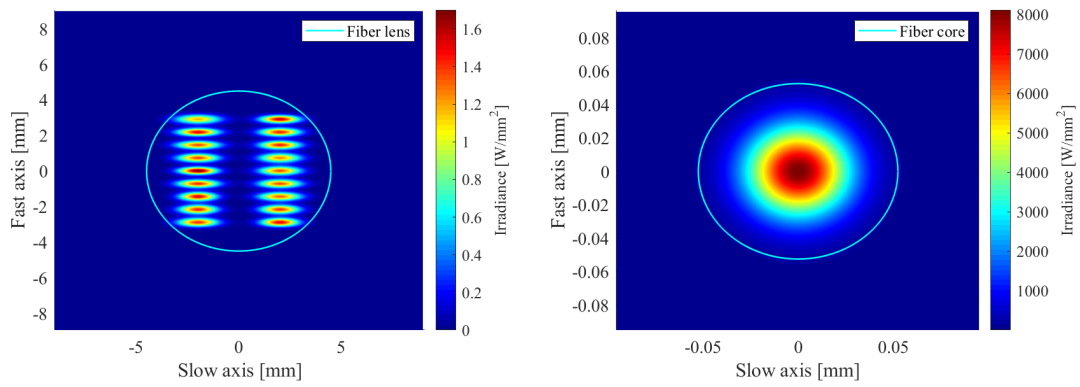


Figure 4.31: Seventh module configuration: field at fiber lens and in fiber core.

Table 4.17: Seventh module configuration outputs with fiber core diameter =  $105\ \mu\text{m}$  and  $\text{NA} = 0.15$ .

	MATLAB
Power losses in fiber [%]	2.3829
Power in NA [%]	99.4086

# Chapter 5

## Beam Shaping Applications

Nowadays, industrial applications involve laser-based systems, especially for materials cutting, because lasers offer well localised power. Furthermore, due to the growth of new advanced fabrication applications, manufacturers are requesting high power systems able to transform the laser intensity profile with much higher precision and control [34]. Optimum processing conditions can be achieved by controlling the main laser parameters, such as polarization, spot size, wavelength, irradiance etc. The manipulation of these parameters allows the so called *beam shaping*, defined as the process of irradiance and beam phase redistribution when the light bumps into the target material [35].

The beam pattern is controlled in terms of phase and amplitude by beam converters, reshaping the radiation spatial profile: for instance, an input Gaussian beam can be transformed into a *top-hat* distribution (super-Gaussian). Beam shaping occurs by means of diffractive optical elements (DOE) modifying an incident laser radiation into a uniform intensity spot: as a consequence, the resulting spot provides well defined shape and sharp edges, creating precise transitions among the treated and untreated areas. Several examples are shown in Fig. 5.1.

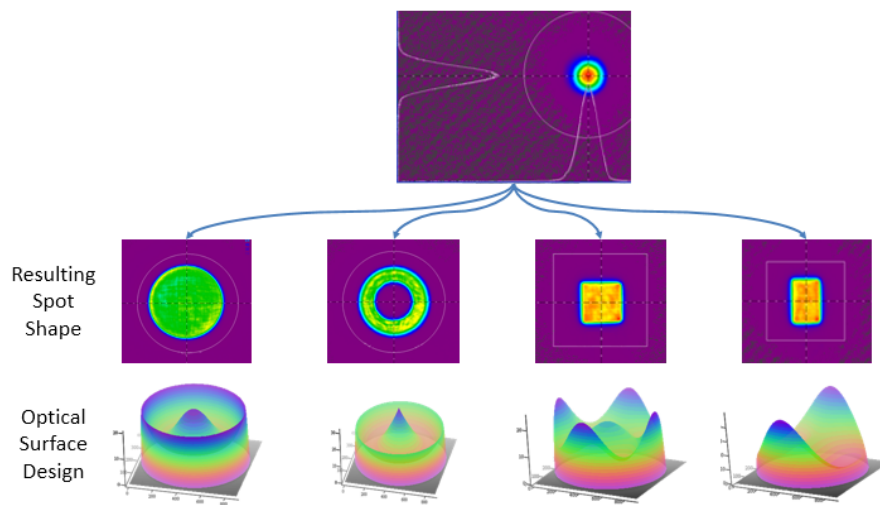


Figure 5.1: Examples of beam shaping [34].

Diffractive optical elements are marked out by several advantages, such as high precision, small size, adjustment for different applications requirements, and are classified into two main categories [36]: beam shapers and beam splitters.

Beam shapers usually work by transforming the far field intensity distribution of the incident radiation. The simplest and oldest beam shaper is an aperture, selecting just a portion of the incident beam and changing its form into circle, square, line etc. The beam shaper class is made up of: diffractive axicons, vortex lenses and top-hat shapers.

Instead, beam splitters are able to divide a single beam (generally collimated) into multiple beams having the same characteristics of the initial one, clearly except the power and the divergence angles. The radiation pattern depends on the diffractive surface, typically leading to a multispots field.

The result of the beam shaping technique is an improvement of laser intensity distribution control, allowing the development of new laser-based applications, like medical implants fabrication, eye surgery and mostly material processing.

The current chapter exhibits different cutting applications involving two round wedge prisms, an axicon and a horizontal laser diodes stack. Moreover, optimization tools have been implemented to find the optimal laser cutting conditions.

## 5.1. Round wedge prism

A round wedge-shaped prism is a transparent optical element whose input and output surface orientations differ for a tilt angle usually around or below  $3^\circ$ . The wedge prism purpose is to deflect an incoming collimated beam, without affecting its main parameters except for the propagation direction. This element is regarded as ideal for obtaining beam steering [37]; moreover, if subjected to a rotation, it can provide a continuous variation of the output beam direction, thus leading to circular outlines. Wedge prisms can also work in pairs to provide beam steering and particular applications as spirals can be achieved by properly setting the rotation speed of the prisms employed.

The beam deviation angle is easily computed by applying the Snell law at the two surfaces defining the prism: if the angles are small, as usually happens, the output deviation angle  $\theta$  can be obtained as a function of the prism refractive index  $n$  and angle between the surfaces  $\alpha$ .

$$\theta = (n - 1)\alpha \quad (5.1)$$

In case of two equal round wedge prisms, the final output angle is approximately twice the deviation angle of each prism, as it is clear when analysing the system by means of ray tracing. One example implementing two prisms defined in Tab. 5.1 is depicted in Fig. 5.2.

Table 5.1: Parameters of round wedge prism.

Diameter	Thickness	Prism angle	Deviation angle
25.40 mm	3.00 mm (min); 4.72 mm (max)	$3.53^\circ$	$2.00^\circ$

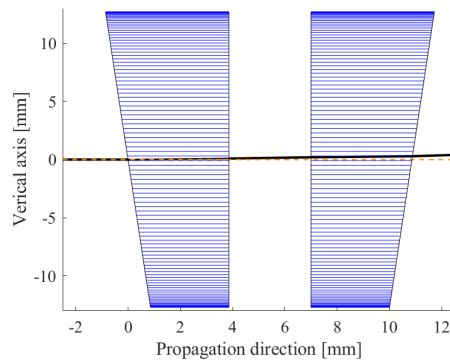


Figure 5.2: Two equal round wedge prisms.

Since the prism does not affect the beam intensity profile, the output beam has the same characteristics of the input collimated beam in terms of irradiance values and distribution: in case of rotating prisms (Fig. 5.3 and Fig. 5.4) the irradiance outline in each time stamp is equal to the input irradiance rotated according to the system velocities and symmetries.

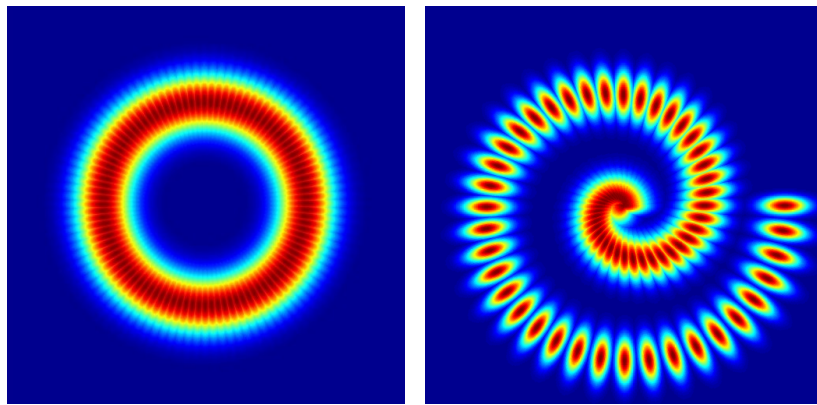


Figure 5.3: Superimposition of beam profiles in different time stamps produced by two round wedge prisms rotating at same (left) and at different speeds (right).

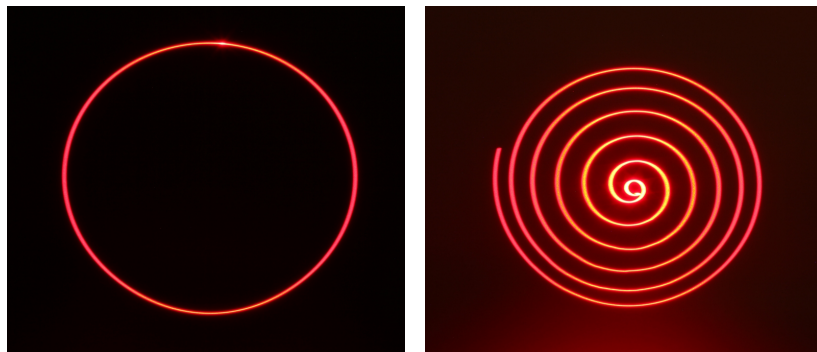


Figure 5.4: Long-exposure photographs provided by Thorlabs of beam profiles produced by two round wedge prisms rotating at same (left) and at different speeds (right).

## 5.2. Axicon

The axicon belongs to prisms category and it is a lens whose peculiarity is the conical surface opposite to the planar surface. Three different types of axicons exist (reflective, refractive and diffractive), but the kind under analysis is just the refractive one (Fig. 5.5).

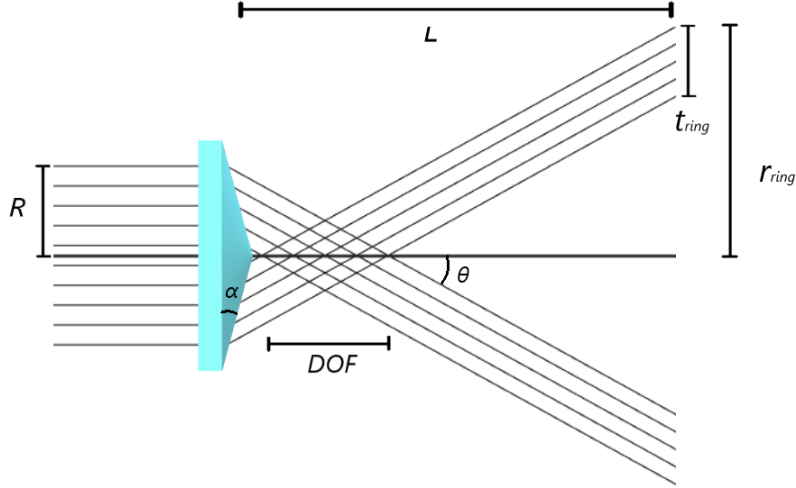


Figure 5.5: Axicon operation scheme.

While ordinary lenses ideally focus the beam just in a single point, the axicon is able to generate a focal line, which is called depth of focus (DOF). The depth of focus depends on the incident beam diameter  $R$ , the axicon refractive index  $n$  and the axicon angle  $\alpha$  according to the following formula [38]:

$$DOF = \frac{R\sqrt{1 - n^2 \sin^2 \alpha}}{\sin \alpha \cos \alpha (n \cos \alpha - \sqrt{1 - n^2 \sin^2 \alpha})} \approx \frac{R}{(n - 1)\alpha} \quad (5.2)$$

Starting from a collimated input radiation, the axicon produces a Bessel beam profile inside the DOF, particularly in this area the beam intensity is almost constant, and a ring-shaped (or annular) intensity profile in far field region. The output beam is non-diverging, or rather the ring radius increments with the distance  $L$  from the axicon, but the ring size remains constant because it mostly depends on the input beam radius [38]:

$$t_{ring} = \frac{R\sqrt{1 - n^2 \sin^2 \alpha}}{\cos \alpha (n \sin^2 \alpha + \cos \alpha \sqrt{1 - n^2 \sin^2 \alpha})} \approx R \quad (5.3)$$

$$r_{ring} = L \left[ \frac{\sin \alpha (n \cos \alpha - \sqrt{1 - n^2 \sin^2 \alpha})}{n \sin^2 \alpha + \cos \alpha \sqrt{1 - n^2 \sin^2 \alpha}} \right] \approx L \tan[(n - 1)\alpha] \quad (5.4)$$

Another main parameter describing the axicon operation is the deflection angle of the beam  $\theta$ , which is computed with respect to the optical axis according to the refractive Snell law:

$$\sin(\alpha + \theta) = n\sin(\alpha) \quad (5.5)$$

A 3D picture of the ray equivalent model of an input radiation propagating through the axicon is depicted in Fig. 5.6. The involved parameters are reported in Tab. 5.2.

The attainment of annular beams allows the employment of axicons in several fields, such as medical, biotechnological or industrial, for the following applications: laser corneal surgery, cutting, welding, optical trapping, frequency doubling and optical pumping.

Table 5.2: Parameters of axicon.

Diameter	Center thickness	Axicon angle	Deviation angle
12.7 mm	3 mm	25°	8°

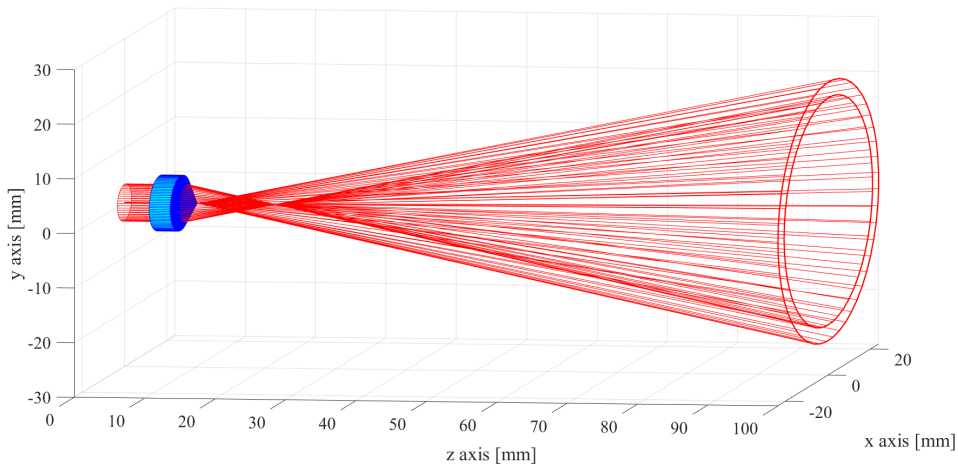


Figure 5.6: Ray equivalent model of beam propagation through an axicon.

**Bessel beams** When a collimated radiation incises on an axicon surface, a wave depicted by a Bessel function of the first kind is generated, or even the so called Bessel beam. The intensity profile results in a series of concentric rings obtained by the interference of the input light with the conical surface. The principal feature of Bessel beams is that they do not experience diffraction because of the minimal spreading in the central lobe of the beam during propagation [39].

The electric field of a Bessel beam can be defined through the zeroth-order Bessel function of the first kind  $J_0$ :

$$E(r, z) = E_0 \cdot \exp(ik_z z) J_0(k_r r) \quad (5.6)$$

where  $r$  is the radial coordinate,  $z$  is the propagation direction and  $k_z$  and  $k_r$  are the longitudinal and radial wavevectors. Clearly, the irradiance is the electric field

squared and, as a result, a series of concentric rings is produced. According to Eq. 5.6, the number of rings should be infinite ideally, but only finite Bessel beams are treated and they are defined as quasi-Bessel beams (Fig. 5.7).

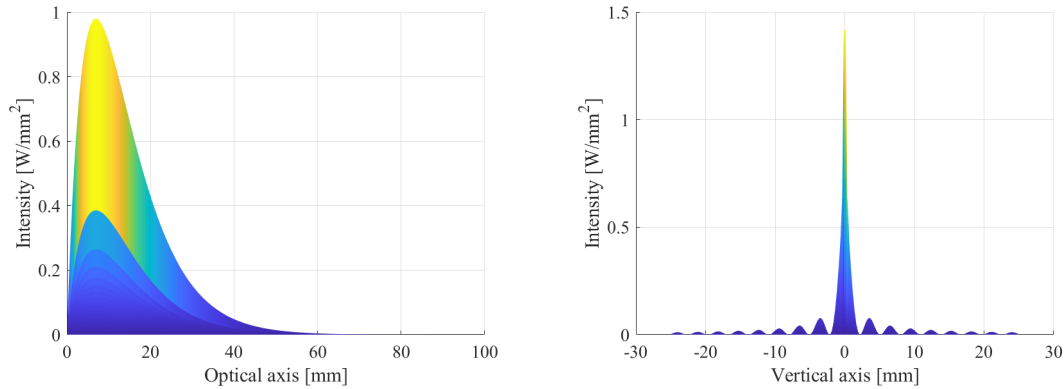


Figure 5.7: Bessel beam intensity.

By comparing Bessel and Gaussian beams, it is possible to state that Bessel beams have larger Rayleigh range, so they point out a longer depth of focus (Fig. 5.8). However, the optical power is distributed on the rings and so the maximum intensity of the central lobe is lower with respect to the Gaussian beam.

When the axicon input radiation is a Gaussian beam, the output beam is defined Gaussian-Bessel, and is depicted by the following intensity distribution [39]:

$$I(r, z) = 2k\pi \tan^2 \alpha (n-1)^2 z I_0 \cdot \exp(-2(n-1)z \tan \alpha / w_0) \times J_0^2(kr(n-1) \tan \alpha) \quad (5.7)$$

where  $I_0$  is the incident beam intensity and  $w_0$  the corresponding beam waist,  $\alpha$  is the axicon angle and  $n$  is the axicon refractive index.

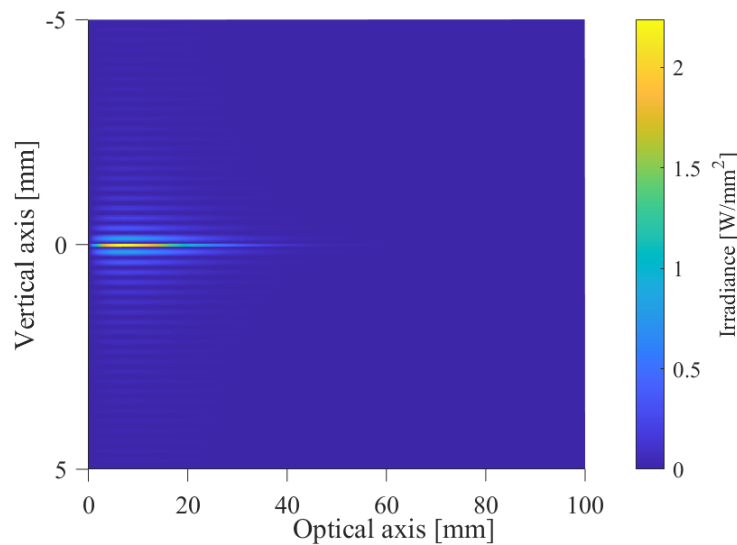


Figure 5.8: Side view of depth of focus where the Bessel beam is generated.

Another Bessel beam realization can be generated using apertures; nevertheless, this technique is quite inefficient since the incident beam should be truncated by the aperture. This is the reason why Bessel beams are usually generated by employing an axicon. Anyways, alignment problems between the beam and the optical element may occur.

**Annular beam intensity** Beyond the region where the rays intersection with the axicon optical axis gives rise to a Bessel intensity profile, the output assumes the characteristic ring shape of an annular beam. The intensity of the latter has been computed numerically, differently from all the cases analysed until the current one, in which analytical formulas based on the Gaussian theory were implemented to obtain the beam irradiance profile.

It is assumed that, since the axicon is treated as an ideal optical element that does not introduce any losses, the total amount of power is conserved during the propagation through it. Therefore, the power carried by the incoming collimated Gaussian beam is exploited in order to compute the output intensity.

The Gaussian intensity profile is associated to a set of rays, that are distributed proportionally to the area below the intensity curve, evaluated by subdividing the space domain in infinitesimal integral intervals: the number of rays then describes the amount of power present on each analysed space interval.

The alternative representation of the axicon input beam by means of power-rays is presented in Fig. 5.9.

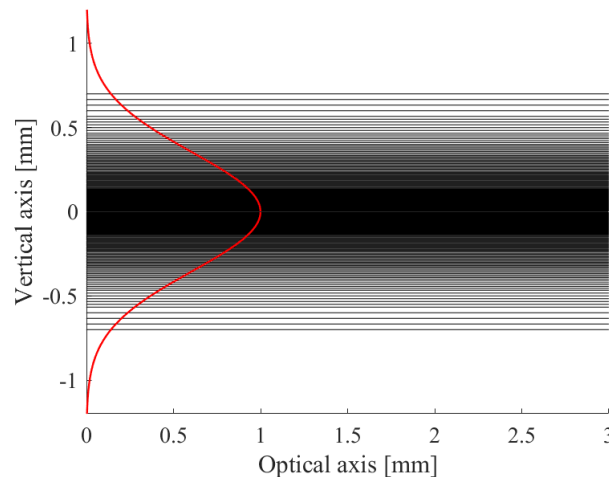


Figure 5.9: Power-rays equivalent model of the axicon input beam intensity.

Since the axicon causes the incoming rays to be deflected, the output rays propagate generating a ring-shaped curve in far field region, whose intensity is determined by the rays density over the ring size. As shown in Fig. 5.10, the annular beam is more intense towards the ring external edge. By reversing the process implemented to generate the input rays, the output rays are exploited to compute the intensity profile by means of power conservation.

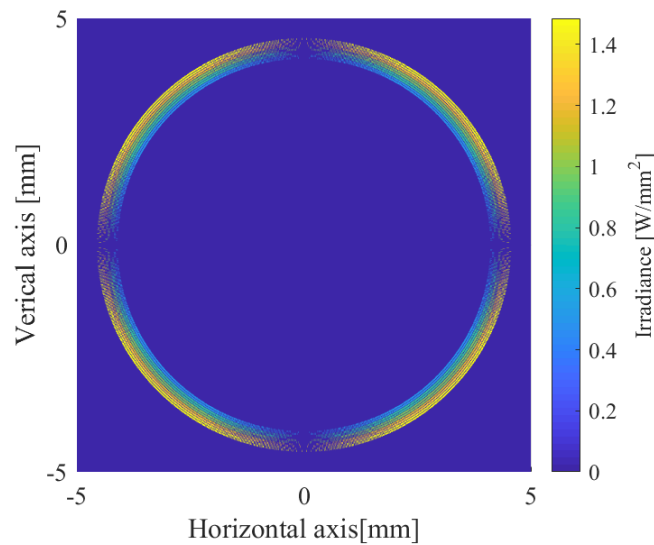


Figure 5.10: Annular beam intensity profile in far field region.

### 5.3. Laser line

The software tool initially designed to simulate a laser diode module has been easily adapted to implement a diodes array intended to cut a piece of the target material. The laser line optical system partially coincides with the module structure, because all the involved chips emissions undergo the collimation process by means of a FAC and a SAC. The laser diode chips must be positioned according to the features of the desired cutting: as in the case presented next, an horizontal cut is provided by an horizontal laser diodes row.

The system, in addition to the two collimating lenses, includes a third cylindrical lens, that operates on the opposite direction with respect to the axis along which the chips are arranged. The diodes are placed side by side along the slow axis in case of the mentioned horizontal cutting case; then, the last lens focuses only the fast axis, and the dimension of the total emission on the slow axis is left unvaried after the SAC collimation. The material to be cut is put in the focal point of the final lens in order to obtain the highest intensity value achievable by the implemented configuration. The cut effectiveness depends indeed on the amount of  $W/mm^2$  delivered by the diodes array in the area intended for the cutting.

A continuous cut is achieved by setting the proper distance between the contribution of each laser source on the material, otherwise the resulting incision is a dashed line. The distance between the spots, in turn, depends on the offset between the chips along the slow axis and on the position of the SAC lenses, that fixes the horizontal final dimension of the spot sizes.

The laser line intensity profile has been simulated by resorting to the parameters of the OSRAM PLPT9 450D\_E A01 blue laser diodes (typical emission wavelength = 447 nm). In particular, 10 chips delivering a power equal to 3.5 W in operating

conditions have been implemented. The whole optical system parameters are reported in Tab. 5.3.

Table 5.3: Laser line system input parameters.

Parameters	Fast Axis	Slow axis
Beam waist [ $\mu\text{m}$ ]	0.75	20
Divergence angle [mrad]	427	61
Chips offset [mm]	-	7.5
Collimating lens EFL [mm]	1.65	80
Focusing lens EFL [mm]	100	-

It has to be remarked that, due to the huge difference of the beam sizes along the SA and the FA caused by the focalisation of the latter, in Fig. 5.11 the representation ranges in the two directions are different, in order to make it possible to appreciate the irradiance profile features.

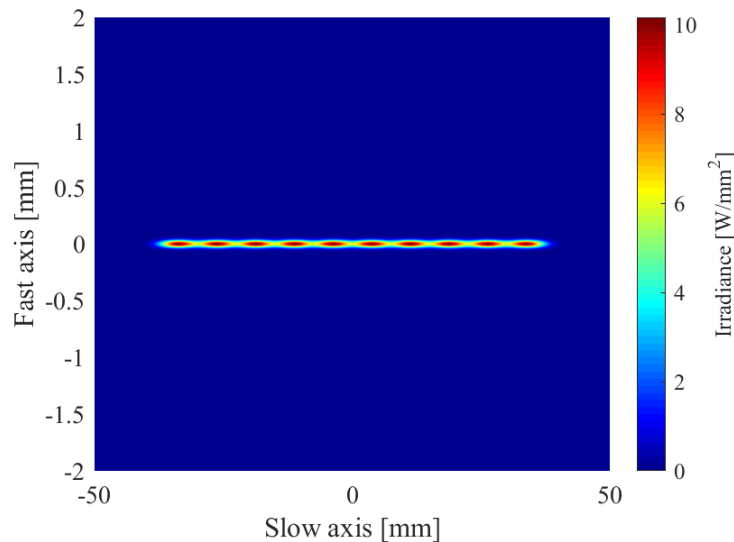


Figure 5.11: Laser line example.

### 5.3.1. Optimization methods

The process of optimization derives from applied mathematics and is adopted to establish the input values of a certain function causing the function result to be the closest possible to a given criterion. One standard optimization application is to maximize or minimize the function under analysis by selecting the proper input values within a definite interval (that can also be unbounded).

The implemented optimization problem aims at minimizing the loss function, or also called cost function, which is based on the definition of a target that should be achieved by feeding the proper input values to the examined function.

For example, in the case of the laser line applied to materials cutting, the irradiance

over the area addressed to the incision must be higher than a threshold in order to be effective; everywhere else it should be null. Then, the function to be minimized is the error between the accepted values of irradiance and the ones depending on the laser line system parameters.

***Fminsearch* algorithm** One of the MATLAB built-in optimization methods is the *fminsearch* algorithm, based on Nelder-Mead simplex method. The latter relies on the  $n$ -simplex concept: the  $n + 1$  test points at which the function to be optimized is computed are arranged to form a simplex, or rather a generalized tetrahedron in  $n$  dimensions having  $n + 1$  vertices. [40]. Therefore, Nelder-Mead optimization method does not make use of derivatives in order to converge. The function is evaluated in each vertex of the simplex, and according to the results, the point that produces the result farther from the optimal one must be replaced by a point depending on the centroid of the remaining points. The function is then computed in the new point and compared with the previous point outcome in order to decide the next step. At each step, the latest simplex vertex is computed by a reflection, a contraction, an expansion or a shrink. The flowchart of the optimization algorithm is shown in Fig. 5.12.

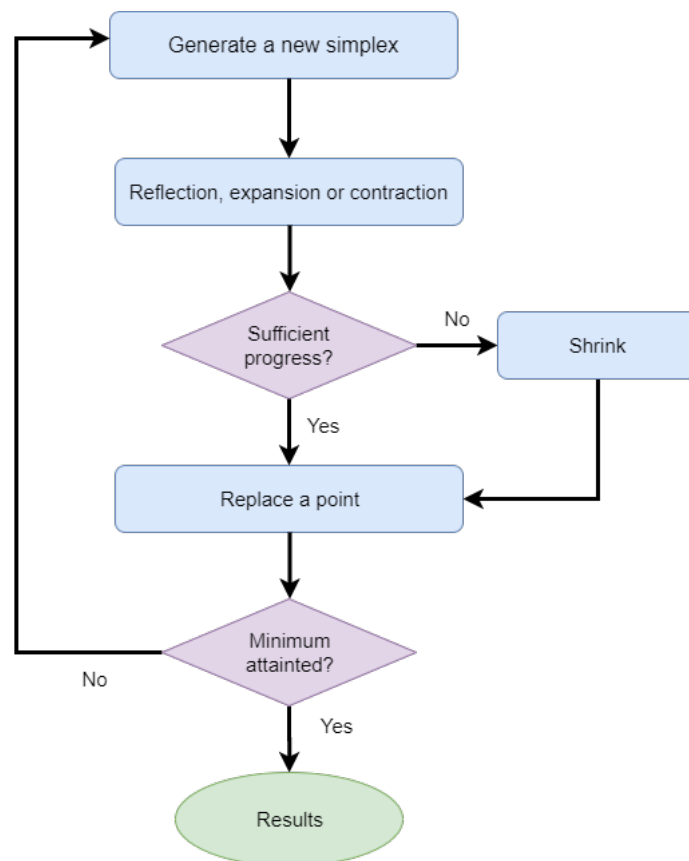


Figure 5.12: Nelder-Mead simplex method flowchart.

**Particle swarm algorithm** MATLAB offers also the possibility to resort to an optimization method for nonlinear problems: the *particle swarm*.

Proposed by Kennedy and Eberhart to simulate social behaviour, the algorithm is inspired from flocks of birds, school of fish or ant colonies searching for the best food source and the sharing of information between members is its key point [41]. The *particle swarm* optimization is based on a group of candidate solutions, or even the particles, moving according to stochastic and deterministic models. At the beginning, particles are distributed randomly to favour the search of the cost function best value: each particle is initialised by a proper velocity and a position, and its movement is influenced by its best position, the group (swarm) best position and its inertia. The cost function is evaluated at every particle location and the algorithm aims at finding the lowest function value and the best location [42].

At each iteration the particles modify their positions according to the new computed velocities and the best known position of the particle and the swarm is updated. Iterations keep on until the algorithm provides a satisfactory solution, or when the stopping condition is achieved (Fig. 5.13).

In the implemented laser line case, to avoid large computational costs, the stopping condition chosen was a maximum number of iterations.

Due to stochastic properties, some consequences follow: the optimized solution is different every time the algorithm is executed, in spite of the same cost function and the same initial values; the computational cost, especially in terms of time, is greater than the *fminsearch* one.

As the previous optimization algorithm, the *particle swarm* is a derivative-free methods.

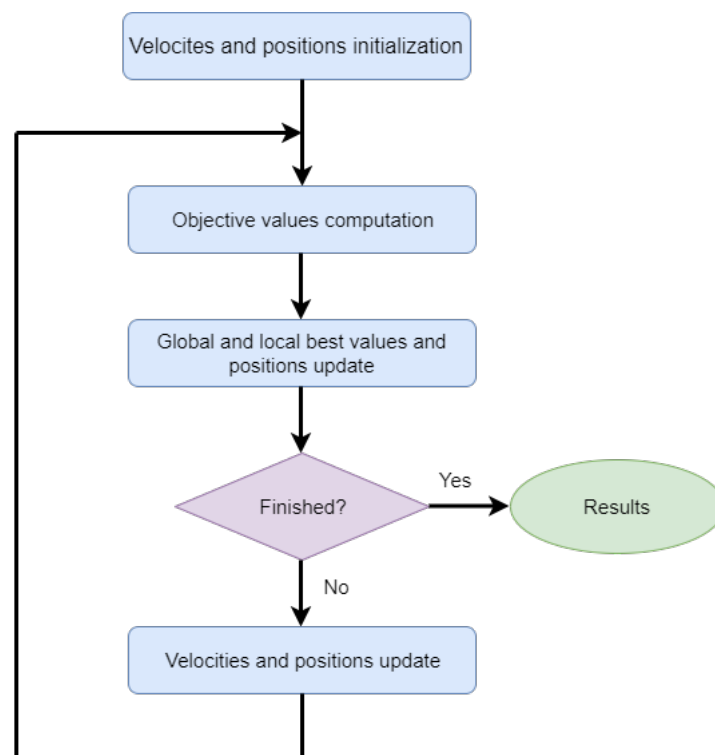


Figure 5.13: Particle swarm flowchart.

In the following table the optimization algorithms results of two laser line applications are reported. Concerning the already discussed structure suitable to produce a laser line (Tab. 5.3), the system for material cutting is made up of an array of 20 or 30 chips (Fig. 5.14) and the purpose is to find the best distance among chips and the best SAC lens location providing a cut about 120 mm long.

In order to find the unknowns of the cost function, a target has to be inserted. In the current case, the target function consists in a rectangular area where the evaluated irradiance should be greater than  $2 \text{ W/mm}^2$  so that material cutting is achieved. The main purpose is to minimize the difference between the target and the simulated field irradiances. By means of the optimization methods, the developed MATLAB tool is able to find the best and lower results for the cost function.

Despite the different mathematics applied, the two optimization algorithms produce the same results, as reported in Tab. 5.4, leading to a difference always below 0.5%.

Table 5.4: Optimization algorithms results comparison.

Case	<i>fminsearch</i> algorithm		<i>particleswarm</i> algorithm	
	Chip distance	SAC position	Chip distance	SAC position
20 chips	5.8502 mm	69.7729 mm	5.8500 mm	69.7850 mm
30 chips	3.9272 mm	47.6537 mm	3.9086 mm	47.7794 mm

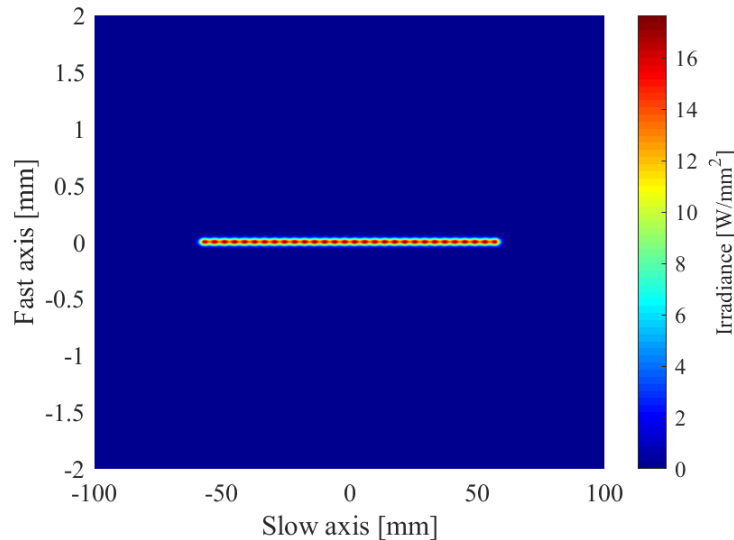


Figure 5.14: Example of laser line optimization output provided by the algorithm *fminsearch* implementing 30 chips.

The optimization program is capable of providing very accurate values for the selected input parameters, but it is always necessary to take into account the concrete feasibility of the system. For example, in the laser line case, the distance at which the chips can be located depends on the adopted equipment tolerance and the value of the SAC focal length must be chosen according to the values available on the product market.

### 5.3.2. Experimental setup

The laser diode emission applied with the cutting purpose has been tested during laboratory experiences; even if the implementation of a laser diode array has not been possible, successful paper cutting has been achieved by exploiting just a single chip.

As it can be noted in Fig. 5.15, the laser diodes employed in the experiment belong to a high-power module, that has been disassembled to make it possible to use the chips singularly. Obviously, some of the module features must be modified to adapt the system to the new application, for example the mirrors that deviate the beams paths towards the fiber are removed so that the beams can travel straight to the cylindrical lens that focalises the fast axis. Moreover, one of the built-in SAC lenses present in the module has been substituted, since the laser diodes cutting capabilities have been analysed in two different configurations: the first employed system is the basic configuration provided by the module, whereas the other one is distinguished by different position of the SAC lens focal length (Fig. 5.16). As a consequence, the experience has been carried out with two different laser diodes, each one aligned with the related SAC.

It has to be remarked that the laser diodes are mounted in the module so that the fast axis is positioned along the horizontal direction and the slow axis along the vertical one. Therefore, the beam profile incident on the paper to be cut is a vertical line.

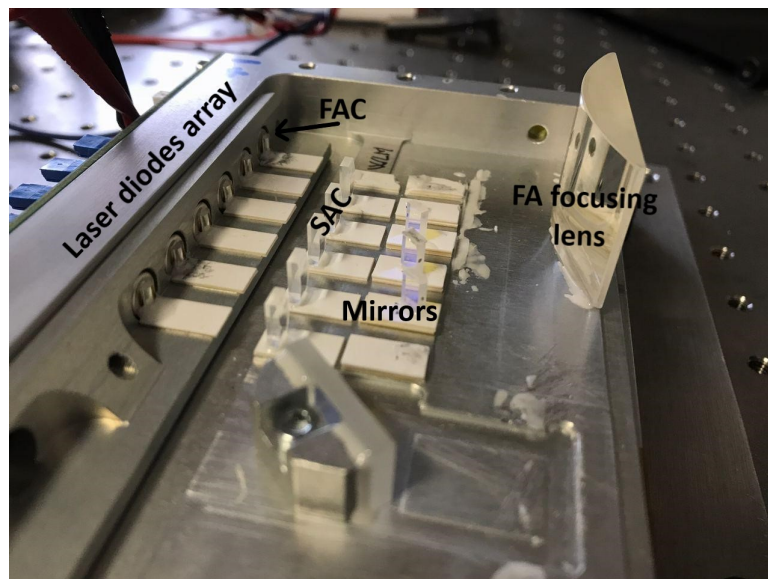


Figure 5.15: Disassembled module suitable to test the cutting properties of a single chip.

The last lens of the optical system, used to focalise the FA towards the target material, is characterized by a focal length of 100 mm; its distance from the source (in this case equal to 65 mm) does not affect the propagation because the incoming beam is collimated by means of the FAC, depicted by a focal length of 1.65 mm. The lenses operating along the fast axis determine the depth of focus, that corresponds

to twice the Rayleigh range size of the focused beam and represents a region where the field intensity variations are minimal. The depth of focus is a fundamental figure of merit to understand where the target material must be located: even if it should naturally be placed in the exact focal length of the last lens, it is a hard task to identify that point just by looking at the beam profile (as it is necessary in absence of a proper equipment). Moreover, being the system mounted manually, errors are unavoidably introduced. Nevertheless, a large depth of focus allows to position the target in a large range around the focus without affecting the cutting performances of the beam.

The lenses employed to manipulate the fast axis produce a Rayleigh range equal to 6.455 mm, resulting in a depth of focus of 12.910 mm.

The SAC lenses implemented during the experience do not affect the depth of focus; indeed, they only cause a change of the slow axis dimension of the beam incident on the paper. Using a SAC characterized by a focal length of 50 mm, the resulting cut turns out to be 8.5 mm long; in the case of the built-in SAC with shorter focal length of 20 mm the incision is just 2.4 mm.

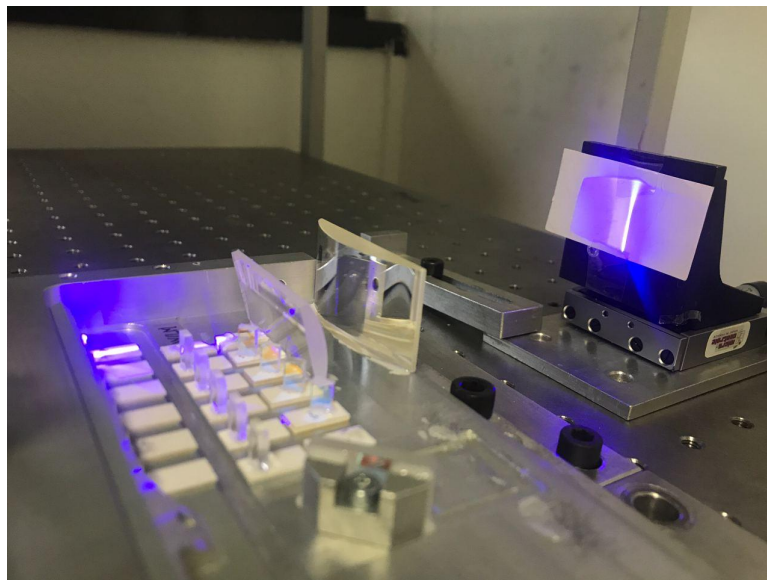


Figure 5.16: Configuration employing the SAC with the longest focal length (50 mm).

Besides the correct positioning of the target, the main parameters impacting the cutting quality are the power delivered by the chip and the material exposure time to the emission.

The latter is conditioned by the material attenuation coefficient, that in turn depends on the material properties and on the incident radiation wavelength. For example, the attenuation coefficient of a light-colored piece of paper is lower than that of a dark-colored one, meaning that the dark material is more transparent to the incoming beam. Fig. 5.17 illustrates two cuts observed by means of a microscope: since they are obtained with different duration of light emission, the outlines are very dissimilar too.

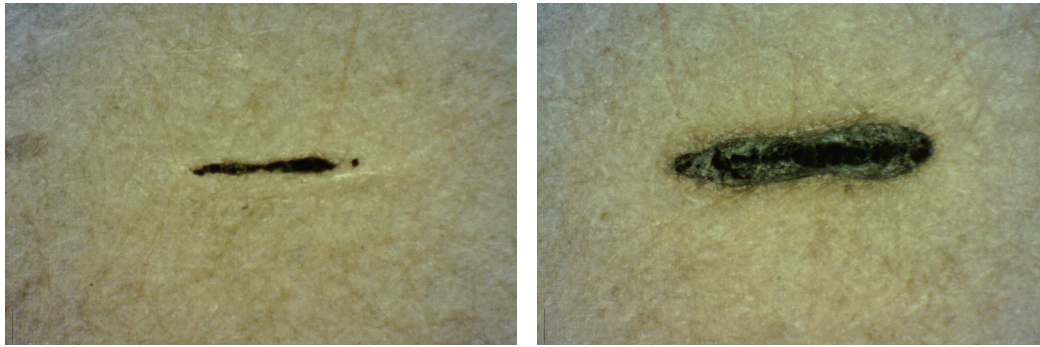


Figure 5.17: Microscope photographs of the paper cutting obtained in the 20 mm SAC focal length configuration in 200 ms (left) and in 500 ms (right).

In order to assure that the laser diode chips emitted the expected amount of power, in the case under study equal to 3.5 W, the power-meter S322C by Thorlabs has been exploited (Fig. 5.18). The detectable power range is very wide (from tens of microwatts up to hundreds of watts) so that different kinds of sources can be analysed with the same device; however, above 50 W a mechanical fan is required for the power meter cooling. The S322C is a thermal power sensor, therefore it takes some time (tens of seconds) to read correctly the incident power. Moreover, it is forbidden to locate the instrument in the focal point of the beam under test, because the temperature rise would lead to a significant overestimation of the power. Lastly, it is recommended to avoid a prolonged exposure to high power radiations, since it could provoke device damages.

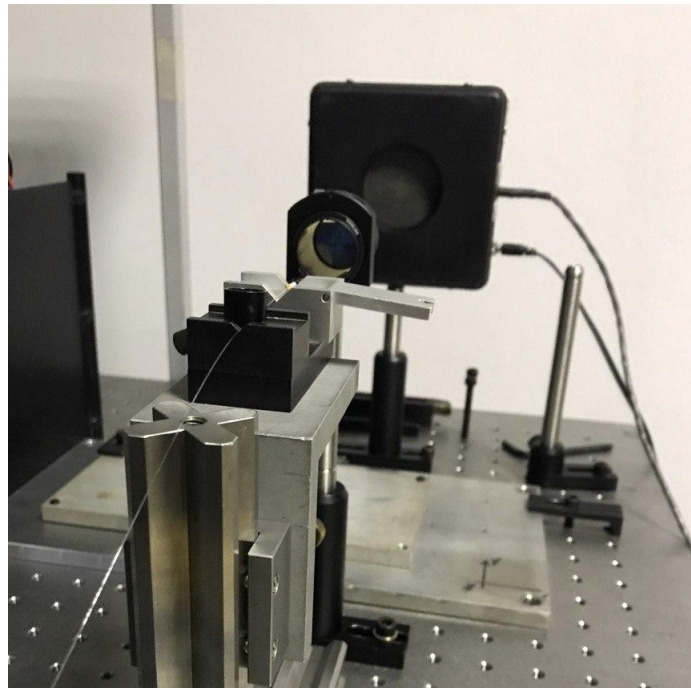


Figure 5.18: S322C power-meter employed to perform the power measurement of an infrared radiation.

The chips output power depends on the driving current, that, in order to achieve lasing condition, must always be higher of the threshold current corresponding to 0.4 A for the PLPT9 450D\_E A01 laser diodes. The operating current of 2.5 A fed to the chips has been provided by the current driver PLPT9 450D\_E A01 manufactured by PicoLAS.

As shown in Tab. 5.5, both the employed laser diodes resulted to emit the power specified by the datasheet.

Table 5.5: Laser diodes measured power.

Laser diode	Power
Chip 1	3.588 W
Chip 2	3.578 W

# Conclusions

In the last few decades the development and the production of high-power laser modules have been deeply relevant especially in the industrial, medical and military sectors. By virtue of their high power density and high efficiency, laser diodes are the mostly employed sources for the laser module realisation. Proper beam combining techniques are exploited to give birth to those properties that embody the laser module figures of merit: great beam quality and high output power (typically from tens of watts up to few kilowatts).

The developed tool is addressed to be integrated in the initial part of the industrial production flow. The design and modelling step is essential before to proceed with the prototype realisation, since the production of few devices, intended for trial tests, is very expensive if compared to the launched mass production. The tool then can be exploited to choose the proper optical components suitable for the given application. In the case of a high-power module design, the tool is useful to understand which are the lenses and fiber characteristics to be implemented in order to achieve the established power delivering in the module fiber, given the available source chips. More generally, the software can represent an important support to assert the feasibility of projects involving the combination of several laser diodes emission before moving forward to the prototyping.

Despite the satisfactory results of the developed software, in order to achieve a more realistic model, the following improvements will be fulfilled.

First of all, currently only paraxial optics has been exploited, so just small divergences have been treated; beams depicted by higher divergence angles could be introduced and, as a consequence, the paraxial approximation will be overcome by applying first order corrections.

The main limitation of the tool is the lack of spherical aberrations: when an aberration free system is employed, the beams incident at different heights of a converging lens are focused in the same focal point, leading to a perfect superposition of the radiations. In this way, an indefinite number of beams could be focused in the module fiber core obtaining always the same power loss. Nevertheless, such situation is just an ideality, thus aberrations should be taken into account.

Another possible improvement is the introduction of mirrors in the module structure. Mirrors purpose is to deviate the radiation direction, but they also provoke beam tails truncation; hence, the truncated beam is no longer properly represented by a Gaussian distribution and it should be fitted by a more suitable function. Moreover, the truncation may lead to a power intensity reduction, as well as imperfections of

reflecting coating of the mirrors could do.

Another non-ideality that the optical elements, as lenses and mirrors, introduce in the system, are the orientation tilts, bringing about the ineffectiveness of *Ray Tracing Technique*: the five rays are deviated in different planes and, as a result, the spot size curve cannot be computed.

One last enhancement could be the treatment of coherent beam combining, which exploits the interference among several beams. Consequently, not only the module, but also the phase of the beam must be taken into account, so that phase stability can be studied to assure proper combining. Finally, the developed tool should implement all the other beam combining techniques in order to maximize the power and the beam quality for a given application.

# Bibliography

- [1] Haiyin Sun. *A Practical Guide to Handling Laser Diode Beams*. SpringerBriefs in Physics, Pittsburgh (USA), 2015.
- [2] Thomas V. Higgins. Article on *The three phases of lasers: solid-state, gas, and liquid*. 1995.
- [3] Giovanni Ghione. *Semiconductor Devices for High-Speed Optoelectronics*. Cambridge University Press, 2009.
- [4] Stimulated Emission-Wikipedia.  
[https://en.wikipedia.org/wiki/Stimulated\\_emission](https://en.wikipedia.org/wiki/Stimulated_emission)
- [5] Hao Yu. Doctoral Thesis on *Laser Diode Beam Spatial Combining*. Politecnico di Torino, 2017.
- [6] R. Paschotta. Article on '*CO<sub>2</sub> lasers*' in the Encyclopedia of Laser Physics and Technology. October 2008.
- [7] B. Gefvert, J. Wallace, G. Overton, A. Noguee. Article on *Annual Laser Market Review Forecast 2019* in Laser Focus World. 2019.
- [8] David Belforte. Article *2018 was another record year, contending with turmoil* in Industrial Laser Solutions. 2019.
- [9] S. Subramonian. *Comprehensive Materials Processing, Vol. 9*. Elsevier, 2014.
- [10] D.A.V. Kliner, L. Sheehan. Article on *High-Power Fiber Lasers* in Tech Briefs. 2017.
- [11] T. Y. Fan. *Laser Beam Combining for High-Power, High-Radiance Sources*. IEEE journal, 2005.
- [12] K. Tojo, S. Masuno, R. Higashino, M. Tsukamoto. Article on *Japan develops blue laser for advanced materials processing* in Industrial Laser Solution. 2018.
- [13] B. Srinivasan, C. L. Linslal, A. Dixit, M. S. Sooraj. *Challenges in Coherent Beam Combining of High Power Narrow Linewidth Fiber Lasers*. Reserch Gate, 2018.
- [14] R. Paschotta. Article on *polarization beam combining* in the Encyclopedia of Laser Physics and Technology. 2008

- [15] H. Yu, Y. Liu, A. Braglia, G. Rossi, G. Perrone. Article on *Investigation of collimating and focusing lenses impact on laser diode stack beam parameter product* in Applied Optics. 2015.
- [16] Keigo Iizuka. *Elements of Photonics, Vol.I.* Wiley-Interscience, 2002.
- [17] Joseph Thomas Verdeyen. *Laser Electronics, Chapter 3: Gaussian Beams.* Prentice Hall, 1989.
- [18] Anna Petrova-Mayor. Article on *Development of an eye-safe solid-state tunable laser transmitter around 1.45  $\mu\text{m}$  based on Cr<sup>4+</sup>.* Research Gate, 2008.
- [19] Maria Dienerowitz. *Physical Optics: Gaussian beams.* Univeritat Klinikum Jena, 2017.
- [20] Colin E Webb. *Handbook of Laser Technology and Applications, Volume I.* IOP Publishing Ltd, 2004.
- [21] RP Photonics Encyclopedia.  
[https://www.rp-photonics.com/broad\\_area\\_laser\\_diodes.html](https://www.rp-photonics.com/broad_area_laser_diodes.html)
- [22] Lucas Hofer. Article on *M<sup>2</sup> and High-order modes.* DataRay Blog, 2016.
- [23] R. Paschotta. Article on '*Hermite-Gaussian modes*' in the Encyclopedia of Laser Physics and Technology. October 2008.
- [24] K. Gillen-Christandl, G.D. Gillen, M.J. Piotrowicz, M. Saffman. *Comparison of Gaussian and super Gaussian laser beams for addressing atomic qubits.* Springer-Verlag Berlin Heidelberg, 2016.
- [25] Rudolf Kingslake, R. Barry Johnson, *Lens Design Fundamentals (Second Edition).* 2010
- [26] Pedrotti, Leno S. *Fundamentals of Photonics, Chapter 3: Basic Geometrical Optics.* Chandra Roychoudhuri, 2008.
- [27] Hyper Physics.  
<http://hyperphysics.phy-astr.gsu.edu/hbase/geoopt/lenseq.html>
- [28] Sophie Morel. *Methods for measuring a lens focal length.* 2011.
- [29] R. Paschotta. Article on *Beam quality* in the Encyclopedia of Laser Physics and Technology. 2008.
- [30] Minerva Programs.  
<http://minerva.union.edu/newmanj/Physics100/LaserTypes/GasLasers.htm>
- [31] R. Paschotta. Article on *Laser Pointers* in the Encyclopedia of Laser Physics and Technology. 2008.

- [32] B. Köhler, T. Brand, M. Haag, J. Biesenbach. Article on *Wavelength stabilized high-power diode laser modules* in The International Society for Optical Engineering. 2009.
- [33] Roland Diehl. *High-Power Diode Lasers: Fundamentals, Technology, Applications*. Springer, 2000.
- [34] Power Photonics.  
<http://www.powerphotonic.com/tools-and-support/additional-resources/enhancing-beam-performance>
- [35] P. Delaporte, I. Zergioti. *Handbook of Flexible Organic Electronics*. Woodhead Publishing, 2014.
- [36] Sintec Optronics. Article on *DOEs for Beam Shaping*. 2020.
- [37] Wedge Prisms.  
<http://www.standaphotonics.com/prisms/wedge-prisms.php>
- [38] An In-Depth Look at Axicons.  
<https://www.edmundoptics.com/knowledge-center/application-notes/lasers/an-in-depth-look-at-axicons/>
- [39] M. Duocastella and C. B. Arnold. *Bessel and annular beams for materials processing*. Laser and Photonics Reviews, 2012.
- [40] Nelder-Mead method - Wikipedia.  
<https://en.wikipedia.org/wiki/Nelder>
- [41] C. Martínez, D. Cao. *Ihorizon-Enabled Energy Management for Electrified Vehicles*. Butterworth-Heinemann, 2019.
- [42] Particle Swarm Optimization Algorithm.  
<https://uk.mathworks.com/help/gads/particle-swarm-optimization-algorithm.html>